

# Astrophysically Relevant Large Carbonaceous Molecules and their Interaction with Atomic Hydrogen

PhD Thesis

Pernille Ahlmann Jensen  
p.ahlmann@phys.au.dk

Supervisor: Liv Hornekær

July 2017

---

Department of Physics and Astronomy  
Aarhus University

This thesis has been submitted to the Graduate School of Science and Technology at Aarhus University in order to fulfil the requirements for obtaining a PhD degree. The work presented has been performed under supervision of Associate Professor Liv Hornekær in the Surface Dynamics Laboratory group at The Department of Physics and Astronomy, Aarhus University, and Professor Els Peeters at The Department of Physics and Astronomy, University of Western Ontario.

# Acknowledgements

While actually writing a PhD thesis may be something you have to do yourself, getting to the point where that is possible takes more than just one person, and throughout the last three years of working towards handing in this thesis, I have been lucky enough to share the experience with many incredible people.

First and foremost I would like to thank my supervisor, Liv Hornekær, for the opportunity to complete my PhD studies in her lab, and for her excellent support and guidance throughout my time in the group. I would like to extend that thank you to everyone I have had the pleasure of working with in the surface dynamics group. To Anders Skov and Frederik Simonsen for their company and help during long days working on the Big Chamber, and to John Thrower for introducing me to the system and experimental astrophysics in general. Thank you to Martha Scheffler for introducing me to STM and the coal chamber during the last few weeks of the project. Also a general thank you other group members past and present; Andrew Cassidy, Line Kyhl, Susanne Halkjær, Antonija Cabo, Jakob Jørgensen, Richard Balog, Jon Iversen, and Federico Andreatta. Their friendship, technical support and patience with my (at times) stupid questions over the last few years has been invaluable. And thank you to John Thrower, Andrew Cassidy, and Frederik Simonsen for their help in proof reading this thesis, their kind and constructive criticism only helped improve it.

A special thank you also to Els Peeters, who kindly agreed to host my research stay at the University of Western Ontario, and to Matt Shannon and Dave Stock, for their support and guidance working on my project, and for teaching me how to program. And thank you to the rest of the Department of Physics and Astronomy at UWO, who all had a hand in making the months I spent in Canada a time I will look back on with nothing but happiness.

Finally, I would like to thank my family and friends. I know I'm not always the easiest person to be around, especially when things are busy and I cancel plans to go to the lab on weekends, and the constant support I have been lucky to have has meant the world to me.

Pernille Ahlmann Jensen, July 2017

# Contents

<b>Contents</b>	<b>i</b>
<b>List of Publications</b>	<b>v</b>
<b>Abbreviations</b>	<b>vii</b>
<b>1 Introduction</b>	<b>1</b>
1.1 The Interstellar Medium . . . . .	2
1.1.1 The Life Cycle of Stars and the Galaxy . . . . .	2
1.1.2 Regions of the ISM . . . . .	4
1.2 Molecular Hydrogen . . . . .	7
1.2.1 Formation of H <sub>2</sub> in the ISM . . . . .	7
1.3 Polycyclic Aromatic Hydrocarbons . . . . .	10
1.3.1 Photoexcitation of PAHs . . . . .	12
1.3.2 PAHs in the ISM . . . . .	17
1.3.3 PAHs and Their Interaction with Hydrogen . . . . .	19
1.4 Fullerenes . . . . .	36
1.4.1 Fullerenes in the ISM . . . . .	38
<b>2 Experimental Setups and Techniques</b>	<b>43</b>
2.1 The Big Chamber . . . . .	43
2.2 The Coal Chamber . . . . .	45
2.3 Temperature Programmed Desorption - TPD . . . . .	46
2.3.1 Adsorption and Desorption . . . . .	47
2.3.2 Thermally Induced Desorption . . . . .	49
2.4 Scanning Tunnelling Microscopy - STM . . . . .	51
2.5 Minor Techniques . . . . .	54
2.5.1 Low Energy Electron Diffraction - LEED . . . . .	54
2.5.2 Auger Electron Spectroscopy - AES . . . . .	55

2.5.3	Density Functional Theory - DFT . . . . .	56
<b>3</b>	<b>The Hydrogen Doser Flux</b>	<b>59</b>
3.1	Measuring the Hydrogen Flux . . . . .	59
3.1.1	The Si(100) Surface . . . . .	60
3.1.2	H/Si(100) TPDs and Flux Measurement . . . . .	60
<b>4</b>	<b>Experimental Results - PAHs</b>	<b>65</b>
4.1	Deuteration of coronene . . . . .	65
4.1.1	Low Temperature Deuteration . . . . .	69
4.2	Hydrogenation of coronene . . . . .	69
4.2.1	Stable Configurations . . . . .	75
4.3	Addition Cross Sections . . . . .	77
4.4	Binding Energies to HOPG . . . . .	77
4.5	Summary . . . . .	81
<b>5</b>	<b>Experimental Results - Fullerenes</b>	<b>83</b>
5.1	C <sub>60</sub> on HOPG and Au(111) . . . . .	84
5.1.1	HOPG . . . . .	85
5.1.2	Au(111) . . . . .	85
5.2	Deuteration of C <sub>60</sub> on Au(111) . . . . .	88
<b>6</b>	<b>Astrophysical Observations</b>	<b>93</b>
6.1	Introduction . . . . .	93
6.2	Sample . . . . .	94
6.3	Analysis Methods . . . . .	95
6.3.1	Classification . . . . .	97
6.4	Results . . . . .	99
6.4.1	PAH Class and Band Profiles . . . . .	99
6.4.2	Band Profiles of the Aliphatic Features . . . . .	102
6.4.3	Correlation Studies . . . . .	107
6.4.4	Summary . . . . .	111
6.5	Discussion . . . . .	112
6.5.1	Chemical and Structural Evolution of the Emitting Population . . . . .	112
6.5.2	Aliphatic Band Profiles and Correlations . . . . .	113
6.5.3	Superhydrogenated PAHs and Their Role in H <sub>2</sub> For- mation . . . . .	114

<b>7</b>	<b>Summary and Outlook</b>	<b>115</b>
7.1	Polycyclic Aromatic Hydrocarbon Experiments . . . . .	115
7.1.1	Outlook . . . . .	116
7.2	Fullerene Experiments . . . . .	118
7.2.1	Outlook . . . . .	119
7.3	Astrophysical Observations . . . . .	119
7.3.1	Outlook . . . . .	120
<b>8</b>	<b>Danish Summary - Dansk Resumé</b>	<b>121</b>
8.1	Sukkersøde Stjernetåger . . . . .	121
8.2	Internetdating for Atomer . . . . .	122
	<b>Bibliography</b>	<b>125</b>



# List of Publications

- **P. A. Jensen**, M. J. Shannon, D. J. Stock, and E. Peeters. Aliphatic Features in Mid-Infrared Polycyclic Aromatic Hydrocarbon Spectra. To be submitted to *Astronomy & Astrophysics*, 2017.



# Abbreviations

AES - Auger Electron Spectroscopy  
AGB - Asymptotic Giant Branch  
AIR - Aromatic infrared bands  
B3LYP - Becke, three-parameter, Lee-Yang-Parr  
BE - Binding Energy  
DFT - Density functional theory  
DHA - 9,10-dihydroanthracene  
DOS - Density of states  
FUV - Far Ultraviolet  
FWHM - Full Width Half Maximum  
GGA - General gradient approximation  
GMC - Giant molecular cloud  
HABS - Hydrogen atom beam source  
HBC - Hexa-peri-hexabenzocoronene  
HK - Habenschaden-Küppers  
HOMO - Highest occupied molecular orbital  
HOPG - Highly ordered pyrolytic graphite  
IMFP - Inelastic Mean Free Path  
IR - Infrared  
ISRF - Interstellar Radiation Field  
ISM - Interstellar medium  
LEED - Low energy electron diffraction  
LDA - Local density approximation  
LDOS - Local density of states  
LN<sub>2</sub> - Liquid nitrogen  
LUMO - Lowest unoccupied molecular orbital  
ML - Monolayer  
PAGB - Post Asymptotic Giant Branch  
PAH - Polycyclic aromatic hydrocarbon

PBE - Perdew, Burke, Ernzerhof  
PDR - Photondominated/Photodissociation region  
PID - Proportional-integral-derivative  
PN - Planetary Nebula  
QMS - Quadropole mass spectrometer  
RN - Reflection Nebula  
RT - Room temperature  
SDL - Surface Dynamics Laboratory  
SNR - Supernova Remnant  
STM - Scanning tunneling microscope/microscopy  
TOF - Time of Flight  
TPD - Temperature programmed desorption  
UHV - Ultrahigh vacuum  
UIR - Unidentified infrared bands  
UV - Ultraviolet  
VUV - Vacuum Ultraviolet  
WPCC - Weighter Pearson Correlation Coefficient  
YSO - Young Stellar Object

# Chapter 1

## Introduction

*"Begin at the beginning," the King said gravely,  
"and go on till you come to the end: then stop."*

— Lewis Carroll, *Alice in Wonderland*

Astrochemistry is the study of the chemistry of the universe and how molecules can form and interact with each other, atoms, and radiation, under the harsh conditions present in many part of the galaxy. It is a highly interdisciplinary field, requiring results and methods from experimental work, astronomical observations, and theoretical modelling and calculations in order to paint a complete picture of the chemistry taking place in the universe. In this thesis I have mainly made use of the first two, though results from theoretical models and calculations will be incorporated and discussed when relevant.

The thesis is concerned with studying large carbon based molecules of astrophysical relevance, and their interaction with hydrogen atoms. These reactions are vastly important in the interstellar medium (ISM). Hydrogen is the most abundant element in space, and up to 20% of interstellar carbon is believed to be locked up in large carbon containing molecules, like polycyclic aromatic hydrocarbons (PAHs) and fullerenes.

In this chapter I will first give a brief introduction to the regions of the ISM to which the results of this project is of most relevance. I will then go on to discussing molecular hydrogen in the ISM, and how it can be formed in different regions. Finally I will give an introduction to PAHs and fullerenes, their structure and spectral characteristics, and observations of their pres-

ence in the ISM. This serves as a literature overview, and includes results from previous experiments, as well as outlines the main motivations for this thesis.

In the chapters following this introduction I describe the experimental setups used in the laboratory part of the project (chapter 2) and the flux measurements (chapter 3). The results from the experiments with PAHs and fullerenes are described in chapters 4 and 5. In chapter 6 I describe the methods and results from astrophysical observations of mid-infrared (IR) PAH spectra containing aliphatic features. Finally in chapter 7 I present a summary and outlook and in chapter 8 a Danish summary of the thesis.

## 1.1 The Interstellar Medium

Although stars and planets make up most of what we see when we look at the sky, they only account for about  $3 \times 10^{-3}\%$  of the galaxy by volume. However, the space between the stars is not as empty as, at a first glance, it appears. Dust and gas pervades this space, known as the ISM. It is not uniformly distributed, but instead formed of many different environments, from regions full of hot ionised gas, to large warm, to wispy clouds of atomic hydrogen, and finally includes cold dense cores in molecular clouds, where star formation takes place.

Despite making up the majority of the galaxy by volume, the ISM is not very massive, with densities ranging from 100 to  $10^{12}$  atoms  $\text{m}^{-3}$ . For comparison, the density in earth's atmosphere is  $\approx 10^{35}$  atoms  $\text{m}^{-3}$ . Temperatures in the ISM range from 5 to  $10^4$  K, and some regions are dominated by a high flux of high energy photons. In short, the ISM is a very harsh, inhospitable environment, but in spite of this, a large variety of complex molecules and larger objects inhabit it.

### 1.1.1 The Life Cycle of Stars and the Galaxy

The material in interstellar space is a product of stellar evolution, and finds its origin in the cores and circumstellar environments of old, evolved stars. Therefore, to properly understand the evolution of the ISM, it is necessary to understand the lives of stars. This section is based mainly on [1, 2].

A star begins its life in the centre of a cold (about 20 K) core of a dense cloud of gas. Natural flow inside the cloud allows for the formation of overly dense regions, which, if they reach sufficiently high densities (the Boner-Ebert

mass) undergo gravitational collapse. The gravitational pressure inwards is opposed by a thermal pressure outwards, caused by radiating gas, leading to a temporary dynamic equilibrium. However, as the gas continues to radiate, it cools, decreasing the outward thermal pressure, resulting in further collapse. This in turn causes the temperature of the gas to rise, and with it, the thermal pressure. This quasi-static cycle is known as the Kelvin-Helmholtz mechanism, and repeats until the gas is sufficiently dense to allow for a new type of pressure to act against the gravitational collapse: that of energy released from nuclear fusion [1].

During collapse, some of the gas and dust surrounding the protostar is swept outward by the interior radiation. The remainder will accrete onto the forming star, forming a circumstellar accretion disk, from which planets can form. Once nuclear fusion of hydrogen into helium starts in the core of the protostar it moves onto the main sequence, where its position depends almost entirely on its mass and metallicity. It will reside on the main sequence for millions to billions of years, while burning hydrogen in its centre.

Once the central hydrogen is depleted the core will contract while the outer layers expand, and the star leaves the main sequence for the asymptotic giant branch (AGB). At this stage in stellar evolution the core consists of stable helium. The temperature in the core is still not sufficient to allow fusion of helium, but in the innermost shell surrounding the core, hydrogen will be burnt. This shell burning progresses until the core becomes hot enough for helium to ignite. Both the length of the fusion processes and which elements can be burnt depend almost entirely on the initial zero-age main sequence mass of the star. The heaviest stars may burn increasingly high atomic mass elements, eventually ending up with a core of iron. Stars the size of our sun, will never be able to burn elements with a higher atomic mass than helium [2].

As a star burns increasingly heavy elements in its core, and lighter elements in the shells, it develops an onion like structure, with different elements dominating the consecutive layers. The different elements are cycled to the surface of the star through convective motions, and pulsations in the stellar atmosphere expel some of the material into the surrounding environment. The speeds of these outflows are dependent on stellar mass. High mass stars have high velocity outflows, up to  $2000 \text{ km s}^{-1}$ , and low and intermediate mass stars have much lower velocity outflows ( $10\text{-}30 \text{ km s}^{-1}$ ) [2].

At the end of its life a very high mass star explodes in a type II supernova (SN). The core of the star becomes too massive for the internal pressure to withstand the force of gravity, and the core undergoes rapid collapse, while the outer layers are violently ejected at speeds of up to  $30000 \text{ km s}^{-1}$ . Heavy elements are formed in this ejecta through rapid nucleosynthesis processes. The material enters interstellar space, cools, and complex molecules begin to form. Dust grains form close to the star, and grow in size as the SNR expands and cools [3, 4]. The chemistry in the supernova remnant (SNR) depends on the elements available in and the chemical balance of the ejecta. The chemical reactions tend to go towards CO - which is a very stable molecule - and what other molecules and grains are formed depends on whether there is a relative overabundance of carbon or oxygen in the star. [5].

### 1.1.2 Regions of the ISM

The ISM can be roughly divided into two distinct regions based on density - the diffuse medium and dense clouds. In the diffuse medium average densities are typically  $\approx 5 \times 10^7 \text{ atoms m}^{-3}$ , and temperatures are around 80 K. They have an average spatial extent of approximately 10 pc, and average masses of the order of 500 solar masses [6]. The diffuse medium is largely transparent, meaning that high energy UV photons important in determining the physical and chemical environments of such regions. The large interstellar radiation field (ISRF), and especially the high flux of far ultraviolet (FUV) photons, hinders the build-up of large, complex molecules, as UV photons are energetic enough to dissociate many of the molecular bonds. As a result the diffuse medium is dominated by atomic gas, and small molecules comprised of 2-5 atoms, many of which are radicals or ions [7]. The hydrogen in these regions is therefore predominantly atomic, though some  $\text{H}_2$  is observed. It can be detected directly through emission in its Lyman and Werner bands in the UV.

Dense clouds, also known as giant molecular clouds (GMCs), contain larger, more complex molecules. The average density in GMCs is  $1.5 \times 10^8 \text{ atoms m}^{-3}$ , and the average temperature is around 10 K. They have a spatial extent of roughly 40 pc and masses of the order of  $4 \times 10^5 M_{\odot}$ . All these parameters vary widely, however, and GMCs are not uniform, but contain cold dense cores with densities of the order of  $10^{12} \text{ atoms m}^{-3}$  and temperatures as low as 6 K [8]. These are the birthplaces of new stars.

The ISRF is attenuated by the material at the outer edges of the cloud,

Simple hydrides, oxides, sulfides, halogens				
H <sub>2</sub> (IR, UV)	CO	NH <sub>3</sub>	CS	HCl
O <sub>2</sub>	H <sub>2</sub> O <sub>2</sub>	PO	CO <sub>2</sub> (IR)	NaCl <sup>a</sup>
H <sub>2</sub> O	SO <sub>2</sub>	OCS	H <sub>2</sub> S	KCl <sup>a</sup>
PN	SiO	SiH <sub>4</sub> <sup>a</sup> (IR)	SiS	AlCl <sup>a</sup>
N <sub>2</sub> O	CH <sub>4</sub> (IR)	HSCN	HF	AlF <sup>a</sup>
HONC	HNCO	AlOH		
Nitriles and acetylene derivatives				
C <sub>2</sub> (IR)	HCN	CH <sub>3</sub> CN	HNC	C <sub>2</sub> H <sub>4</sub> <sup>a</sup> (IR)
C <sub>3</sub> (IR,UV)	HC <sub>3</sub> N	CH <sub>3</sub> C <sub>3</sub> N	HNCO	C <sub>2</sub> H <sub>2</sub> (IR)
C <sub>5</sub> <sup>a</sup> (IR)	HC <sub>5</sub> N	CH <sub>3</sub> C <sub>5</sub> N	HNCS	C <sub>6</sub> H <sub>2</sub> (IR)
C <sub>3</sub> O	HC <sub>7</sub> N	CH <sub>3</sub> C <sub>2</sub> H	HNCCC	C <sub>3</sub> H <sub>6</sub>
C <sub>3</sub> S	HC <sub>9</sub> N	CH <sub>3</sub> C <sub>4</sub> H	CH <sub>3</sub> NC	C <sub>3</sub> H <sub>7</sub> CN
C <sub>4</sub> Si <sup>a</sup>	HC <sub>11</sub> N	CH <sub>3</sub> C <sub>6</sub> H	HCCNC	
H <sub>2</sub> C <sub>4</sub>	HC <sub>2</sub> CHO	CH <sub>2</sub> CHCN	CH <sub>2</sub> CCHCN	
Aldehydes, alcohols, ethers, ketones, amides				
H <sub>2</sub> CO	CH <sub>3</sub> OH	HCOOH	HCOCN	CH <sub>3</sub> CH <sub>2</sub> CN
CH <sub>3</sub> CHO	CH <sub>3</sub> CH <sub>2</sub> OH	HCOOCH <sub>3</sub>	CH <sub>3</sub> NH <sub>2</sub>	NH <sub>2</sub> CH <sub>2</sub> CN
CH <sub>3</sub> CH <sub>2</sub> CHO	CH <sub>2</sub> CCHOH	CH <sub>3</sub> COOH	CH <sub>3</sub> CONH <sub>2</sub>	NH <sub>2</sub> CN
NH <sub>2</sub> CHO	(CH <sub>2</sub> OH) <sub>2</sub>	(CH <sub>3</sub> ) <sub>2</sub> O	H <sub>2</sub> CCO	CH <sub>2</sub> CHCN
CH <sub>2</sub> OHCHO	(CH <sub>3</sub> ) <sub>2</sub> CO	H <sub>2</sub> CS		
C <sub>2</sub> H <sub>5</sub> OCHO		CH <sub>3</sub> SH		
Cyclic molecules				
C <sub>3</sub> H <sub>2</sub>	SiC <sub>2</sub>	<i>c</i> -C <sub>3</sub> H	CH <sub>2</sub> OCH <sub>2</sub>	C <sub>6</sub> H <sub>6</sub> (IR) ?
<i>c</i> -SiC <sub>3</sub>	H <sub>2</sub> C <sub>3</sub> O	C <sub>2</sub> H <sub>4</sub> O		
Molecular cations				
CH <sup>+</sup>	CO <sup>+</sup>	HCNH <sup>+</sup>	OH <sup>+</sup>	HN <sub>2</sub> <sup>+</sup>
CH <sub>3</sub> <sup>+</sup>	HCO <sup>+</sup>	HC <sub>3</sub> NH <sup>+</sup>	H <sub>2</sub> O <sup>+</sup>	H <sub>3</sub> <sup>+</sup> (IR)
HS <sup>+</sup>	HOC <sup>+</sup>	H <sub>2</sub> COH <sup>+</sup>	H <sub>3</sub> O <sup>+</sup>	SO <sup>+</sup>
HCS <sup>+</sup>	HOCO <sup>+</sup>	CF <sup>+</sup>	HCl <sup>+</sup>	H <sub>2</sub> Cl <sup>+</sup>
Molecular anions				
C <sub>4</sub> H <sup>-</sup>	C <sub>6</sub> H <sup>-</sup>	C <sub>8</sub> H <sup>-</sup>		
CN <sup>-</sup>	C <sub>3</sub> N <sup>-</sup>	C <sub>5</sub> N <sup>-</sup>		
Radicals				
OH	C <sub>2</sub> H	CN	C <sub>2</sub> O	C <sub>2</sub> S
CH	C <sub>3</sub> H	C <sub>3</sub> N	NO	NS
CH <sub>2</sub>	C <sub>4</sub> H	HCCN <sup>a</sup>	SO	SiC <sup>a</sup>
NH (UV)	C <sub>5</sub> H	CH <sub>2</sub> CN	HCO	SiN <sup>a</sup>
NH <sub>2</sub>	C <sub>6</sub> H	CH <sub>2</sub> N	C <sub>5</sub> N <sup>a</sup>	CP <sup>a</sup>
SH	C <sub>7</sub> H	NaCN	KCN	MgCN
C <sub>3</sub> H <sub>2</sub>	C <sub>8</sub> H	MgNC	FeCN	
C <sub>4</sub> H <sub>2</sub>	HNO	H <sub>2</sub> CN	HNC <sub>3</sub>	HO <sub>2</sub>
C <sub>6</sub> H <sub>2</sub>	AlNC	SiNC	C <sub>4</sub> Si	SiCN
HCP	CCP	AlO		
Fullerenes				
C <sub>60</sub> (IR)	C <sub>70</sub> <sup>a</sup> (IR)	C <sub>60</sub> <sup>+</sup> (VIS) ?		

<sup>a</sup>These species have been detected only in the circumstellar envelope of carbon-rich stars.

**Figure 1.1:** Table showing the molecules identified in the ISM in 2013. Figure from [7]. The number of molecules identified in the ISM is now almost 200 [9].

leading to large variety in the molecular inventory of the clouds. To date, almost 200 different molecular species have been detected [9]. Some of these molecules are listed in the table in Fig. 1.1. The lack of high energy UV photons inside the clouds also leads to the the  $\text{H}_2/\text{H}$  ratio being close to unity. However, also as a result of to the lack of exciting UV photons,  $\text{H}_2$  is not directly detectable in GMCs. Instead, the  $J = 1-0$  transition in CO is used to trace the molecular gas. This method assumes a particular ratio between CO and  $\text{H}_2$ . It is however possible that this is not a generally good assumption, at least outside our own galaxy, as there is evidence to suggest that the  $\text{CO}/\text{H}_2$  ratio depends on metallicity [10].

Some parts of the GMCs are subject to stronger radiation fields, and exhibit higher temperatures. The chemistry in these regions is dominated by photodissociation, and for the same reason they are known as photodissociation regions (PDRs, also sometimes referred to as photon dominated regions). They are essentially border regions, either between the dense clouds and the diffuse medium or between newly formed stars and the rest of the GMC.

Interesting chemistry also takes place in the circumstellar environments of evolved and dying stars, *e.g.* planetary nebulae (PNe) and supernova remnants (SNRs). When a low to moderate mass star nears the end of its life, it sheds most of its outer layers in slow, but massive winds. When most of the envelope has been ejected the core, now a hot white dwarf, becomes exposed, and eventually ionises the surrounding gas. This causes the gas to light up as a PN [2].

When a high mass star dies it explodes in a supernova. While the core of the star collapses, the stellar envelope is ejected in a massive explosion that shocks the surrounding interstellar medium. SNRs are prominent sources of radioemission from relativistic electrons spiralling around strong magnetic fields, and of x-ray emission due to the very hot gas, at temperatures of the order of  $10^6$  K. No two SNRs are alike, but in general they are often characterised by long, delicate filaments of gas [5, 2].

In these circumstellar environments of dying stars, a lot of interesting chemistry can take place. PAHs and fullerenes have been detected in PNe, and are believed to form in these regions from smaller carbon bearing species in a bottom-up scenario. [11, 12, 13, 14, 15]. SNRs are sites of active dust and large molecule formation [3, 4], and PAH molecules are expected to form in the expanding ejecta in bottom-up reactions similar to those of soot chemistry [15].

It is not just atomic and molecular gas that is found in the ISM. In some regions dust grains are present. The grain size distribution ranges from very large molecules to  $\mu\text{m}$ -sized grains. The grains tend to be either carbon or silicate based, depending on whether they are formed in a carbon or oxygen rich environment, and may also contain trace amounts of metals, like Mg or Fe [16]. In very cold regions the dust grains will be covered in icy mantles, consisting mainly of  $\text{H}_2\text{O}$  ice, which may also contain molecules like CO,  $\text{CO}_2$ ,  $\text{CH}_3\text{OH}$ ,  $\text{NH}_3$ , and similar simple species [17]. Interstellar dust grains are important catalysts for the formation of many molecules found in the ISM, and play a very important role in the formation of  $\text{H}_2$ , as gas phase formation of  $\text{H}_2$  is not efficient in the ISM.

## 1.2 Molecular Hydrogen

The hydrogen molecule is the most abundant molecule in space, and it plays a key role in determining the range of chemical complexity in the molecular universe, as well as in determining the timescales of star and planet formation [5, 7], as it plays an important role in cooling the molecular clouds through line emission. Furthermore, without molecular hydrogen present, many of the almost 200 molecular species observed in the galaxy could not be formed. Reaction networks for the gas phase formation of some carbon and oxygen bearing molecules are shown in Fig. 1.2. Molecular hydrogen is involved in many of these reactions, either as a reactant or a catalyst, and without it, the rich gas phase chemistry observed in the ISM would not be possible. The solid blue lines in the figure indicate the point at which the presence of  $\text{H}_2$  becomes necessary for the molecules to form.

### 1.2.1 Formation of $\text{H}_2$ in the ISM

$\text{H}_2$  is easily photodissociated in the ISM [18], an efficient formation route is required to maintain its high abundance. Jura (1975) [19] proposed a required formation rate at 70 K of  $10^{-17} \leq R \leq 3 \times 10^{-17} \text{ cm}^3\text{s}^{-1}$ , based on observations of the  $\text{H}_2$  abundance and the radiation field. Only a grain surface formation route is efficient enough in these regions. However, Habart et al. [18] found a formation rate of  $R_f \approx 10^{-16} \text{ cm}^3\text{s}^{-1}$  is needed in PDRs in order to maintain the observed abundance of  $\text{H}_2$ . This rate is significantly

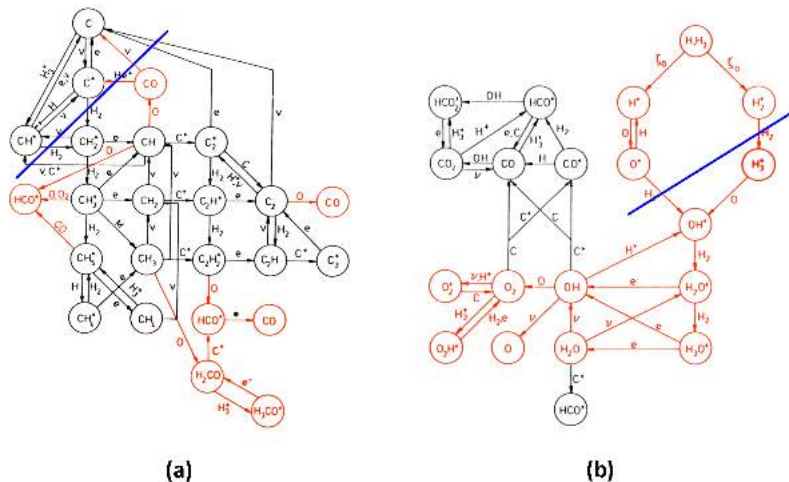


**Figure 1.2:** Reaction networks showing the gas phase formation route of a sample of (a) carbon and (b) oxygen based molecules. The blue lines indicate the cut-off point, beyond which  $\text{H}_2$  is needed in order for the rest of the molecules to form. Figure adapted from [5].

higher than that found by Jura [19].

However, no efficient gas phase route to  $\text{H}_2$  formation exists in the ISM.  $\text{H}_2$  cannot be formed in simple two-body collisions between neutral atoms, since it is a homonuclear molecule with no dipole allowed transitions with which to dispose of the excess energy. When the pressure is at terrestrial levels  $\text{H}_2$  can be formed in three body collisions, where the excess energy of the reaction can be carried away by the third atom, allowing the first two to form a bond. In the ISM however, the density is not high enough for this type of reaction to occur efficiently, and other formation mechanisms have to be invoked.

In many regions of the ISM the required formation rate can be explained by invoking reactions on dust grain surfaces. Surface reactions are very efficient in two different temperature domains, and will each be described here in turn.

Firstly, grain surface reactions are important and efficient in regions where the gas temperature is less than 20 K, such as the inner regions of GMCs. In this temperature domain, dust grains are covered by icy mantles, consisting mostly of water ice. Atomic and molecular species can get trapped in this ice, or physisorb onto the surface of it. In the latter case, most species

will be bound to the surface weakly, and are free to diffuse around on the surface. When two atoms meet on the surface they can react to form a molecule (known as the Langmuir-Hinshelwood process). The molecule can subsequently leave the surface upon further processing of the dust grain (*e.g.* heating by stellar photons, sputtering by gas phase species), or simply upon formation of the molecular bond, as  $\text{H}_2$  is more weakly bound to the surface than H. This has been studied experimentally a number of times for silicates [20, 21, 22, 23], carbonaceous materials [24, 25, 26], and for water ice [27, 28, 29]. When the temperature reaches more than roughly 20 K, however, this process becomes inefficient, as the H atoms will not remain on the surface long enough for the Langmuir-Hinshelwood process to be effective. The temperature domain in which this process remains efficient can be extended somewhat by increasing the roughness of the surface [30], but not enough to explain the  $\text{H}_2$  formation rate in the galaxy at large.

The second domain in which  $\text{H}_2$  formation on dust grains is very efficient is at gas temperatures higher than roughly 500 K, such as SNRs or shocks. In these regions atoms may chemisorb onto either carbon or silicate based dust grains. In chemisorption a chemical bond is formed between the adsorbate and the substrate, and the atom will not be free to diffuse around on the surface, but rather stay in the place where it first hit. If a second atom is incident on that same adsorption site, it may abstract the first atom, creating a molecule (via the Eley-Rideal process)[31, 32]. This only works at high temperatures because the atom needs to overcome an adsorption barriers to chemisorb to a carbonaceous surface (*e.g.* the barrier for graphite: 200 meV) [33].

However, in regions where the gas temperature is between 20 and 500 K, dust grain reactions, while they do take place, are not sufficiently efficient to account for the required  $\text{H}_2$  formation rate. In PDRs, which is one such type of region, a correlation has been observed between the  $\text{H}_2$  formation rate and emission from PAHs, so it has been suggested that such molecules might play a role in the formation of molecular hydrogen in the ISM [18, 34]. This section is mainly based on [35, 5, 36].

## 1.3 Polycyclic Aromatic Hydrocarbons

Polycyclic aromatic hydrocarbons (PAHs) comprise a family of stable, aromatic, molecules consisting of fused benzenoid rings. On the Earth PAHs are most commonly known as the highly carcinogenic products of incomplete combustion reactions. They are found in soot and car exhaust as well as smoked and barbecued food. PAHs are also observed ubiquitously throughout the interstellar medium as the carriers of the aromatic infrared bands (AIBs) at 3.3, 6.2, 7.7, 8.6, 11.2, and 12.7  $\mu\text{m}$  [37, 38, 39]. They are believed to account for between 5 and 20% of the carbon available in the galaxy [40], and are therefore likely play a very important role in many different processes in interstellar environments.

The main constituent of PAH molecules is carbon. Carbon has atomic number 6 and exists in three isotopes. The most common,  $^{12}\text{C}$  accounts for 98.9% of all carbon, while  $^{13}\text{C}$  accounts for 1.1% and the radioactive  $^{14}\text{C}$  exists only in trace amounts. A carbon atom has six electrons, two in the 1s orbital, two in the 2s orbital, and two in the 2p orbitals. Atomic orbitals are described by one-electron wave functions, and the different types of orbitals are characterised by the orbital angular momentum quantum number,  $l$  [36, chap. 3]. Angular momentum  $l = 0$ , characterises the s-orbital, while p-orbitals are characterised by  $l = 1$ . d- and f-orbitals have angular momenta  $l = 2$  and  $l = 3$  respectively. The s-orbitals are spherical and centered on the nucleus of the atoms, while the p-orbitals have two lobes with a node on the nucleus, *i.e.* a dumbbell shape. There is one s-orbital for each energy level,  $n$ , in an atom, and three p-orbitals for any given  $n > 1$ , one along each axis.

When atoms bind together to form molecules the atomic orbitals combine to form molecular orbitals and accumulate electron density in the internuclear region [36, chap. 8]. Carbon has four valence electrons which participate in chemical bonds, the two 2s electrons and the two 2p electrons. When forming bonds the s- and p-orbitals in the carbon atoms hybridise. Carbon shows three different types of hybridisation, which are illustrated in Fig. 1.3. The most common is  $sp^3$  hybridisation, where the 2s and three 2p orbitals combine to form four equivalent hybridised orbitals. This results in a tetrahedral shape with an angle between the orbitals of  $\theta = 109.5^\circ$ . This type of hybridisation is found, for example, in diamond. Another possibility for carbon is  $sp^2$  hybridisation, in which two p-orbitals hybridise with an s-orbital to form three equivalent hybridised orbitals, leaving one unhy-

bridised p-orbital. This creates a planar-trigonal structure, with an angle between the hybridised orbitals of  $\theta = 120^\circ$ . The unhybridised p-orbital is oriented perpendicular to the bond axes. This type of bonding is found in graphite and in PAHs. The last option for carbon is sp hybridisation, where one p-orbital and one s-orbital combine. This results in two hybridised orbitals and two unhybridised p-orbitals. The structure is linear and the two unhybridised orbitals lie perpendicular to the bond axis and to each other. Acetylene is an example of a molecule in which the carbon is sp hybridised. Bonds formed along the bond axis by hybridised orbitals are called  $\sigma$ -bonds, while bonds formed above and below the bond axis are called  $\pi$ -bonds. These are usually delocalised over a large part of the molecule, while  $\sigma$ -bonds remain localised in the region between the atoms forming the bond.

Aromatic hydrocarbons are mostly planar molecules (with few exceptions, e.g. fullerenes) in which the carbon is  $sp^2$  hybridised. They are, by definition, cyclic (made up of 5 and 6 membered rings), and follow Hückel's rule, which states that they must contain  $4n + 2$  delocalised  $\pi$ -electrons, where  $n$  is the number of carbon atoms in the molecule, and can be either zero or any positive integer. The  $\pi$ -electrons are delocalised above and below the carbon skeleton of the molecule, and the more extended the delocalisation, the more stable the molecule [5]. The simplest aromatic hydrocarbon is benzene, ( $C_6H_6$ ), a cyclic molecule with one 6-membered ring. PAHs are defined as aromatic hydrocarbons containing three or more fused benzenoid rings, although the 2-ringed naphthalene ( $C_{10}H_8$ ) molecule is often included in the family, as it has similar physical and chemical characteristics.

A few different PAHs are shown in Fig. 1.4. PAHs can be divided into two families; the pericondensed PAHs (lhs Fig. 1.4) and the catacondensed PAHs (rhs Fig. 1.4). Pericondensed PAHs contain carbon atoms which are members of three separate aromatic rings. A subclass of this category are the centrally condensed PAHs, which are the most stable types of aromatic molecules, since the  $\pi$ -electrons are completely delocalised over the whole molecule. In catacondensed PAHs any carbon atom may not be a member of more than two separate rings.

In the experiments presented in this thesis the molecule coronene ( $C_{24}H_{12}$ ) has been used as an analogue for interstellar PAHs. Coronene has an average mass of 300.33 amu, and if it only contains  $^{12}C$ , has a mass of 300.09 amu. This means it is small enough to easily evaporate, and pump out of the vac-

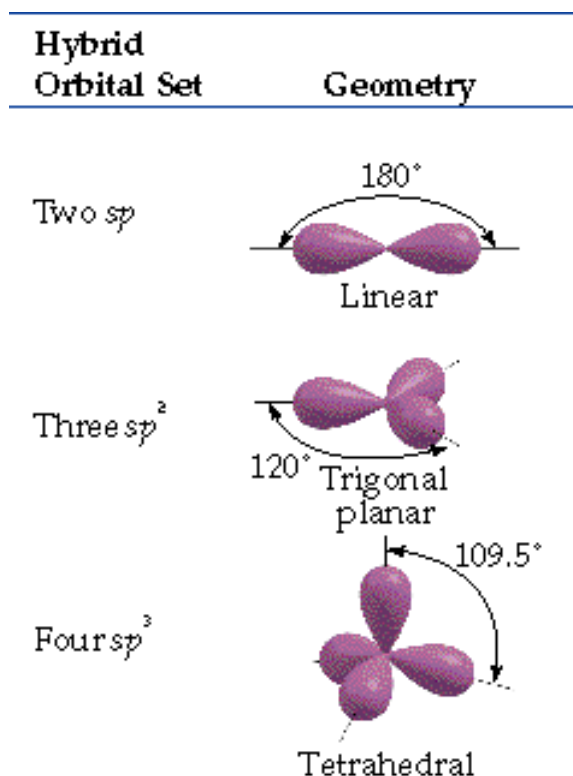


**Figure 1.3:** An illustration of the different types of hybridisation possible in a carbon atom, and the resulting bond configurations. Adapted from [41].

uum chamber. It is also small enough to measure with the mass spectrometer we have available (see chap. 2 for experimental details). At the same time it is large enough to contain all possible hydrogenation sites (if no distinction is made between zigzag and armchair edges, see section 1.3.3). Furthermore, theoretical calculations on very large molecules are computationally costly, and so smaller molecules are preferred for *e.g.* density functional theory (DFT) calculations.

### 1.3.1 Photoexcitation of PAHs

In order to understand the observations of PAHs in the ISM, we must first understand how they interact with FUV photons, and how this relates to the vibrational temperature of the molecules emitting in the infrared (IR). The

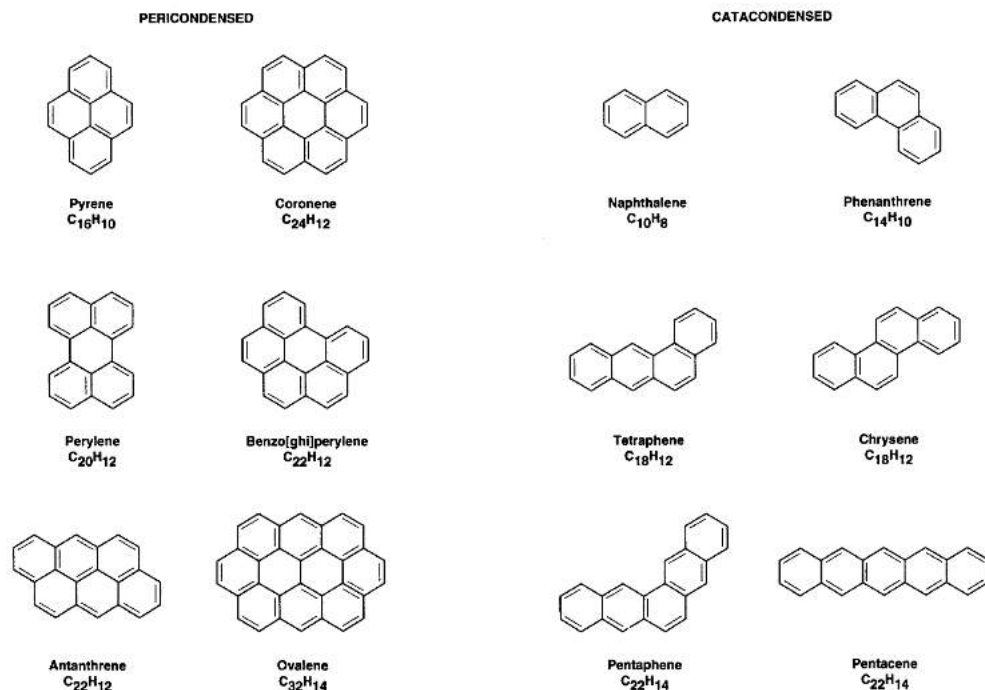


Figure 1.4: Structure of different PAH molecules.

temperature of the molecules varies over time. Immediately upon absorption of a FUV photon the temperature of the molecule will jump to several 100 K, and once it de-excites it will cool back down to the equilibrium gas temperature of a few 10s K.

## Photophysics

A PAH molecule can absorb FUV photons of certain energies, corresponding to specific electronic transitions in the molecule, from the electronic ground state to the first or second, or higher excited states, i.e.  $s_0 \rightarrow s_1, s_2$ , etc. Once a molecule is excited, various de-excitation processes exist.

1. Ionisation (If the energy of the photon is sufficient to overcome the ionisation potential)
2. Photodissociation
3. Collisional de-excitation

#### 4. Infrared fluorescence

Collisional de-excitation, while an important de-excitation process in high pressure terrestrial environments, does not play a large role in interstellar environments, as the density is not high enough to have a sufficient number of collision partners. Ionisation and photodissociation can and do occur, but the most important de-excitation process for PAHs in the ISM is IR fluorescence.

Once a PAH molecule is excited, IR fluorescence can proceed in two ways; either through internal conversion or intersystem crossing. In internal conversion the electronic excitation is converted to a highly vibrationally excited state of a lower lying electronic state. In intersystem crossing the molecule is transferred to a highly vibrationally excited state of an electronic state of different multiplicity, *i.e.* from a singlet to a triplet state. Both internal conversion and intersystem crossing are non-radiative.

The process of internal conversion or intersystem crossing is followed by a cascade down the vibrational manifold to the vibrational ground state, resulting in emission of multiple IR photons. If the molecule is in a singlet state this fluorescence is usually the final stage of relaxation. If intersystem crossing has occurred the molecule is still electronically excited, and the final state will be emission of a visible photon, relaxing the molecule to the ground state (phosphorescence). An energy diagram illustrating these processes is shown in Fig. 1.5.

The electronic structure of PAH molecules is size and structure dependent. For a neutral PAH the  $\pi$ -bonding levels are completely filled, while the  $\pi^*$ -antibonding levels are empty. The total width of the bands is constant, but the number of energy levels increases with PAH size, thus decreasing the energy separation between the levels. This means that the energy separation between the bonding and antibonding levels also decreases with PAH size. PAHs essentially behave as semiconductors, due to the dispersive nature of the antibonding levels and the delocalisation of the  $\pi$ -electrons over the entire molecule. Their optical properties in the UV are dominated by electronic transitions, while their optical properties in the IR are dominated by vibrational transitions. The FUV absorption properties are similar between PAHs, however, the onset of the first transition is size dependent though, shifting to longer wavelengths for larger PAHs.

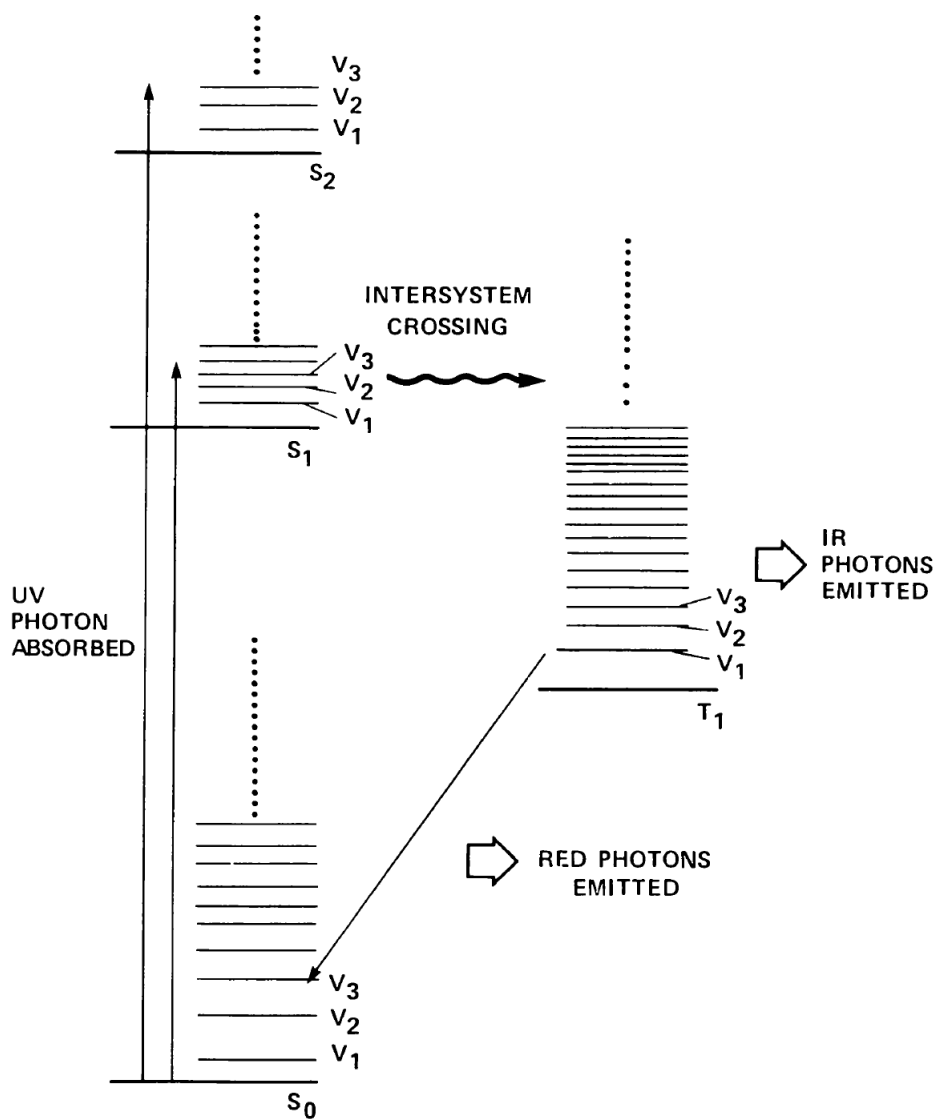


**Figure 1.5:** Energy level diagram, showing potential excitation and relaxation processes of a PAH molecule. Taken from [38].

The average absorption cross section scales roughly with the number of  $\pi$ -electrons in the system, with  $\sigma_{FUV} = 7 \times 10^{-18} N_C \text{ cm}^2$ . A high density of states of highly vibrationally excited species means that the different vibrational states of the molecule are efficiently coupled, ensuring a rapid redistribution of energy among all the accessible vibrational modes. The rate constant depends on the coupling between the vibrational modes and the density of states at the internal energy of the molecule.

A PAH molecule with roughly 50 carbon atoms in a diffuse cloud will absorb a UV photon approximately once a year, while the same molecule in a PDR will absorb a photon every 10 minutes or so. The timescale for relaxation in comparison, is very fast. The timescale for internal conversion is  $10^{-12}$  s, and  $10^{-9}$  s for intersystem crossing. The time scale for vibrational redistribution is  $10^{-12}$  s. The large differences in timescale results in the temperature of the species fluctuating widely, as the heating of the molecules is infrequent, and the cooling very rapid. Large PAH molecules and very small grains (VSGs) will be heated to some 2200 K upon UV absorption, and will rapidly cool down to the equilibrium gas temperature.

The energies at which PAH molecules emit in the IR correspond to vibrations of the molecular bonds. Roughly speaking, these vibrational modes can be divided into stretching modes, bending modes, and combination modes. It is possible to identify the bond involved in the vibration from the wavelength of the IR feature, but since the emission is only connected to that particular bond rather than the molecule as a whole, it is not possible to identify a specific molecule from the vibrational emission alone.

It is, however, possible to identify a family of molecules, and the nature of the bonds involved in the transition. One example is the CH stretch transition. For an aromatic CH bond (*i.e.* where a H atom is bound to a  $sp^2$  hybridised C atom), the CH stretch transition occurs at  $\simeq 3.3\mu\text{m}$ , whereas for an aliphatic CH bond (*i.e.* when a H atom is bound to an  $sp^3$  hybridised C atom) the CH stretch transition occurs at around  $3.4 \mu\text{m}$  [42, 43].

## PAH Charge

Interstellar PAHs are found to exist in different charge states. The charge distribution results in a balance between photoionisation and electron recombination (or attachment). A typical interstellar PAH with 50 carbon

atoms has ionisation potentials (for the first three ionisation states) of 6.2, 9.7, and 13.3 eV respectively. The next ionisation state has an ionisation potential above the Lyman alpha energy (13.6 eV), and thus cannot be reached in diffuse clouds. The same 50 carbon atom interstellar PAH molecule has an electron affinity for the first excess electron of 2.6 eV, and -0.9 eV for the second. Thus the a small interstellar PAH has a limited number of charge states, from  $\text{PAH}^-$  to  $\text{PAH}^{3+}$ , available to it.

The charge state of a PAH in a given environment is determined by the ionisation and recombination balance, which in turn is determined by the intensity of the radiation field, the gas temperature, and the electron density, and also influenced by the PAH size.

### 1.3.2 PAHs in the ISM

Prominent emission bands at 3.3, 6.2, 7.7, 8.6, 11.2, 12.7  $\mu\text{m}$  amongst others, are observed ubiquitously throughout the ISM, as well as the circumstellar environments of many evolved and young stellar objects [12, 44] and planetary atmospheres in our own solar system [45, 46]. They have been assigned to the fluorescence of PAH molecules, as discussed above [37, 38, 39, 47, 35].

Through combining theoretically calculated and experimentally measured spectra with observations it is possible to characterise the emitting PAH population, and by extension their physical and chemical environments (see for example [48, 49, 50, 51, 52, 53, 54, 55, 56, 57]). Two different interstellar PAH spectra are shown in Fig. 1.6, illustrating the similarities and differences between PAH bands in different objects [47]. The same bands are observed in many different objects, but some variations do occur in band profiles and peak positions. These variations are to be found both between different objects and spatially, within extended objects. This has led to a four-component classification scheme to differentiate between the variable PAH profiles [47, 58, 59]. PAH spectra are separated into four different classes based on the shape and peak position of the 7.7  $\mu\text{m}$  band.

1. **Class A:** The 7.7  $\mu\text{m}$  band peaks to the blue of 7.7  $\mu\text{m}$ , and the 8.6  $\mu\text{m}$  band is a clearly separate peak.
2. **Class B:** The 7.7  $\mu\text{m}$  band is significantly redshifted compared to class A spectra, and the 8.6  $\mu\text{m}$  band is still a separate feature.

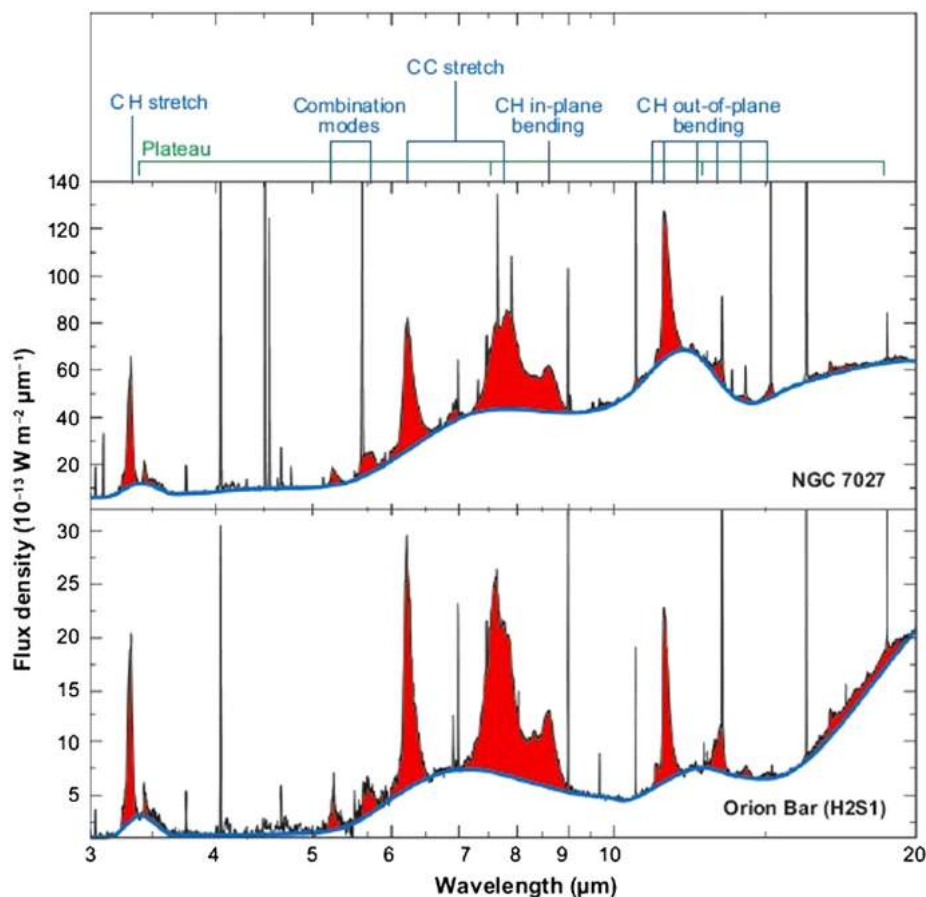


**Figure 1.6:** Mid-IR Spectra of NGC7023 and the Orion Bar PDR, showing the PAH emission features. The modes giving rise to specific features are labelled above. [47]

3. **Class C:** The  $7.7 \mu\text{m}$  band is very broad and the  $8.6 \mu\text{m}$  band is no longer a separately identifiable feature. The whole complex peaks around  $8.2 \mu\text{m}$ .
4. **Class D:** The  $7.7 \mu\text{m}$  band is broad, and the  $8.6 \mu\text{m}$  band is only partly resolved if at all. The complex peaks between  $7.9$  and  $8 \mu\text{m}$ .

The different PAH classes have been shown to be somewhat dependent on object type. Class A spectra are mainly found in interstellar objects such as PDRs and HII regions (where the hydrogen gas is ionised), and a small number of planetary nebulae (PNe). Class B spectra are found in a

wide range of evolved and young stellar objects (YSOs), while class C and D are mostly comprised of post-AGB (pAGB) stars and variable stars. The spectral variations in the PAH bands reflect a physical (*e.g.* structural) or chemical change in the PAH population between the different objects, but the exact origin of the variability has not yet been determined.

One possibility is that the variability between the PAH classes, and by extension ISM objects, is caused by a change in the size distribution of the PAHs between environments [50, 51, 60]. Another possibility is that it is due to a varying importance of aliphatic and aromatic material [61, 12, 62, 63, 64, 65, 66]. Aliphatic material in this case refers to PAHs where aromatic  $sp^2$  hybridised carbon bonds have been converted to  $sp^3$  hybridised bonds by the addition of a hydrogen atom. This bond removes a  $\pi$ -electron from the system.

For example it is thought that the broadened  $7.7 \mu\text{m}$  band in class C spectra could signify an increased abundance of aliphatic material. Processing by UV photons preferentially destroys aliphatic bands, leading to a dominance of aromatic material as the environment evolves from star to ISM. An increase in aliphatic material on going from the ISM to YSOs can be explained by a dynamic equilibrium of hydrogenation reactions and abstraction [62]. This is of special importance in regard to the formation of  $\text{H}_2$ .

The presence of aliphatic material in the PAH population can be studied directly from the PAH observations, through comparison with experimentally and theoretically acquired spectra. Bands at  $3.4$ ,  $6.9$ , and  $7.25 \mu\text{m}$  are aliphatic in nature. It is, however, unclear exactly which type of aliphatic material (*e.g.* hydrocarbon chain molecules, methyl side groups on aromatic molecules, or superhydrogenated PAHs) is responsible for the occurrence of these bands [67, 68, 42, 69, 43].

I have studied this further in an astronomical context as part of this thesis, and the results are described in detail in chapter 6.

### 1.3.3 PAHs and Their Interaction with Hydrogen

As mentioned above, PAHs are ubiquitous in the ISM, and we study their interaction with hydrogen, in order to determine whether they play a role in the formation of  $\text{H}_2$ , and in that case, how large a role that is. Furthermore, it is useful to study the interaction between PAHs and hydrogen from a terrestrial perspective, as a way to limit their negative health effects or as a way to store hydrogen for energy purposes [70, 71, 72].

In this section some experimental and theoretical studies of hydrogen addition to PAHs are discussed, particularly in relation to  $H_2$  formation under interstellar conditions. Hydrogen can be added to PAHs in up to five different sites. On the edge of the molecules there are outer and inner edge sites. The outer edge site is a secondary carbon atom, with one hydrogen already bound. The inner edge site is a tertiary carbon atom placed on the edge of the carbon skeleton. PAHs can have either zig-zag or armchair edges, resulting in a total of four different edge binding sites. The fifth possible addition site is a centre site, a tertiary carbon atom in the middle of the PAH molecule [73, 74].

Adding a hydrogen atom changes the hybridisation of the binding carbon atom from  $sp^2$  to  $sp^3$ , causing an alteration in the local  $\pi$ -electron structure, which in turn changes the geometry and strain of the nearby carbon atoms. This generally lowers the barrier for subsequent hydrogen addition to adjacent carbon atoms.

### Neutral PAH Molecules

For neutral molecules hydrogen addition to coronene has been studied through density functional theory (DFT) calculations [74]. Coronene has only zig-zag edges, resulting in three possible additions sites, outer and inner edge and centre site. In [74] the addition route for the first eight hydrogen atoms was studied. The energetically most favourable first addition was found to be to an outer edge site. This addition has a barrier of 60 meV and a binding energy (BE) of 1.45 eV. The addition barrier to an inner edge or centre site for the same initial H atom was found to be almost three times as large. The second hydrogen atom has the highest BE if it binds to an outer edge site neighbouring the first addition site. This causes the C-C bond to tilt, stabilising the C-H bonds and resulting in a binding energy of 3.25 eV. This addition of the second hydrogen atom to the adjacent outer edge site is barrierless.

The third H atom binds to an inner edge site that is adjacent to a hydrogenated outer edge site, with a barrier of 30 meV and a BE of 1.55 eV. The fourth and fifth atoms will bind to adjacent outer edge sites without a barrier, and binding energies of between 2.8 and 3.0 eV. The sixth atom is the first to add to a centre site. It binds to the centre site next to the third hydrogen atom, on the opposite side of the molecule (bottom), without a barrier and with  $BE \simeq 3$  eV. Hydrogen atom number seven will add to the

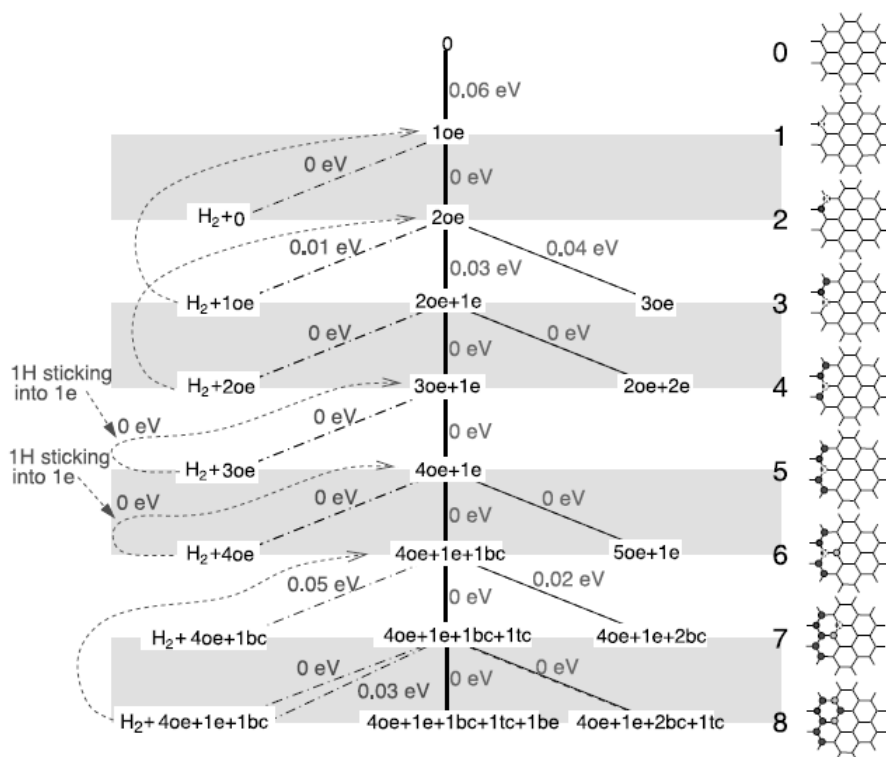


**Figure 1.7:** Reaction pathways of the addition of hydrogen atoms to coronene, and the abstraction of H<sub>2</sub>, calculated using density functional theory. The right hand side of the figure shows the total number of extra hydrogen atoms involved in each step. The centre line represents the most energetically favourable addition reaction, and the dashed lines to the left represent abstraction reactions. Lines to the right represent less energetically favourable addition reactions. The abbreviations *oe*, *e*, *tc*, and *bc* are used to describe the resulting structure, denoting outer edge, inner edge, top centre, and bottom centre sites respectively. To the far right in the figure the structure of the carbon backbone is shown. From [74].

neighbouring centre site, on the top side of the molecule, again without a barrier and this time with a BE of 1.5 eV. Atom number eight can add to an inner edge site with no barrier and a BE of 3.2 eV.

After addition of the first atom, the authors also examined Eley-Rideal abstraction, and found that this was possible with no barriers and provide a catalytic route to the formation of  $H_2$ . In conclusion, the largest barrier involved in the addition of hydrogen to coronene is the 60 meV barrier associated with the addition of the first atom, meaning that if the first atom is added, superhydrogenation of the molecule will follow and competing  $H_2$  abstraction reactions are favourable. The addition and abstraction pathways for the first eight atoms are shown in Fig. 1.7.

Similar DFT calculations have been performed for the addition of the first two hydrogen atoms to the PAH molecule pyrene [75]. They also found the barrier for the first addition to be 60 meV, and the second addition to be barrierless. Abstraction was found to have a barrier of 50 meV. For anthracene the barrier for addition of the first hydrogen atom was also found to be 60 meV, while for the infinitely long polyacene it was found to be only 34 meV. This smaller barrier can be explained by the partly radical nature of the edge carbon atoms in the polyacene. All calculations show that the favoured position for the first adatom is always an outer edge site [74, 75, 76, 77, 78].

Hydrogenation reactions for pyrene have also been theoretically studied taking quantum tunnelling at low temperatures into account [79]. It was found that at 40 K the addition rate was non-negligible, and there was a pronounced isotope effect, consistent with a tunnelling effect. This process is likely very significant for the colder environments of the ISM.

PAH hydrogenation reactions have also been studied experimentally. Previous experiments carried out using the Big Chamber in the Surface Dynamics Laboratory at Aarhus University (see chapter 2 for details) have studied the hydrogenation of coronene monolayers on graphite [80, 81, 82, 83]. In [80] a coronene monolayer (ML) was exposed to different fluences of deuterium (D) at a gas temperature of 2300 K. The masses of the desorbing species were measured in temperature programmed desorption (TPD) measurements (see chapter 2). The mass distribution for different atom fluences can be seen in figure 1.8. Masses higher than 348 amu were detected,

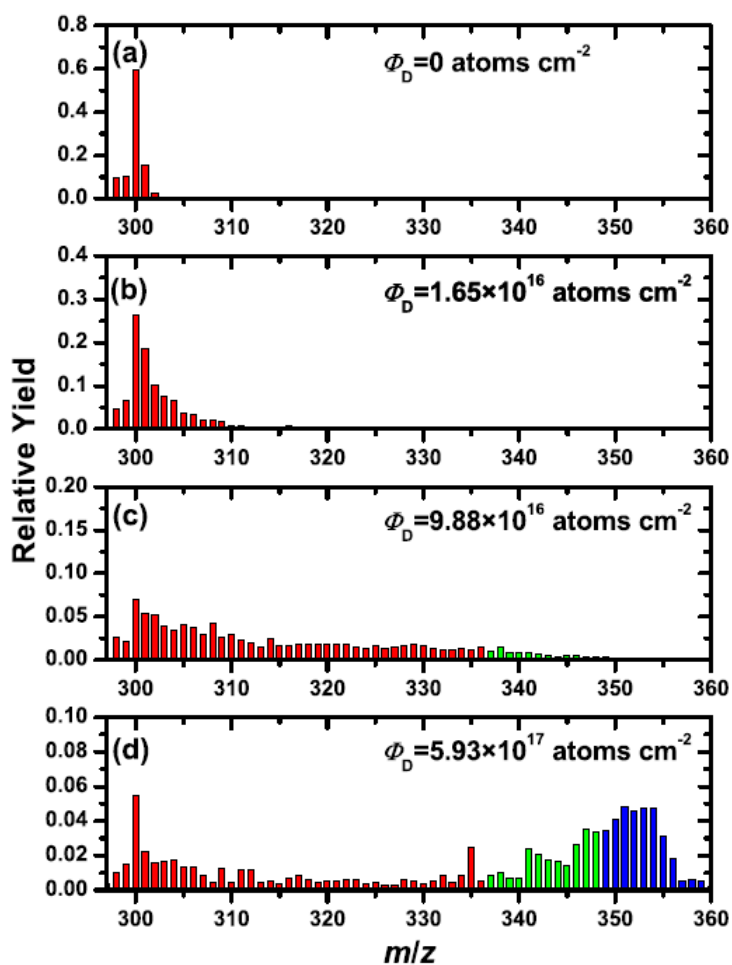


**Figure 1.8:** The mass distribution of superdeuterated coronene, for various fluences of D atoms at 2300 K. From [80].

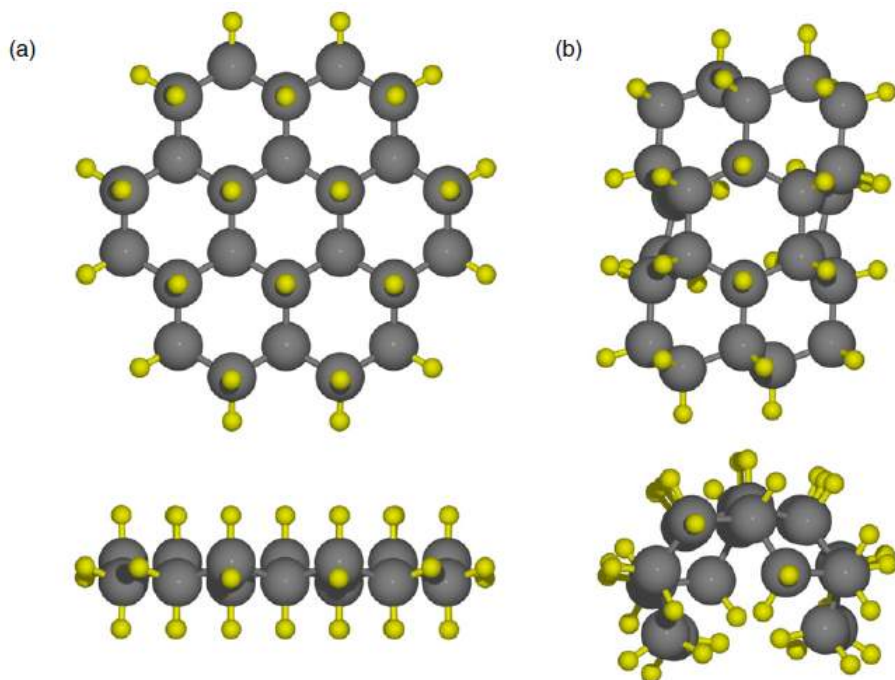


**Figure 1.9:** The relaxed, stable structures of trans- (a) and cis-perhydrocoronene (b). From [80].

which are only possible if D atoms are added to all available carbon atoms, and the original H atoms on the edge of the molecule are exchanged for D. Thus these experiments show indirectly that  $\text{H}_2$  formation from superhydrogenated PAHs is possible. DFT calculations of the stability of various superhydrogenated structures were also included in this investigation. They showed that the fully superhydrogenated coronene, perhydrocoronene, is stable, both in its trans- (molecule hydrogenated evenly on both sides) and cis-forms (molecule only hydrogenated on one side). In the case of cis-perhydrocoronene the molecule buckles up to relax, and the most stable route to formation is if the centre ring is hydrogenated last [80]. The structures of these molecules are shown in Fig. 1.9.

Kinetic simulations were performed in order to determine the addition and abstraction cross-sections of the system [82]. These are relevant if one wants to quantify the role PAHs play in molecular hydrogen formation in the ISM. In the simple kinetic simulations of [82], the molecular mass distri-

bution was evaluated through a series of timesteps, and for each step one of three reactions was permitted: a deuterium atom could add to the molecule, a hydrogen atom could be abstracted from the molecule, or a deuterium atom could be abstracted from the molecule. The algorithm used is not site specific, and thus does not distinguish between outer, and inner edge sites, and centre sites.

The rate of addition of atoms to the molecule is determined by the (known) flux of deuterium atoms at the sample,  $\phi_D$ , and the (unknown) addition cross-section to a molecule with  $n$  additional H or D atoms,  $\sigma_{add}(n)$ . It is assumed that the addition cross-section depends only on the number of additional atoms already attached, and not on the specific addition sites. The cross-section for the first addition can be obtained directly from experiments, and was determined to be  $0.55 \pm 0.03 \text{ \AA}^2$  [82]. For  $n > 0$ ,  $\sigma_{add}(n)$  is treated as a variable parameter.

The rate of abstraction scales linearly with  $\phi_D$ ,  $n$ , and the abstraction cross-section,  $\sigma_{abs}(n)$ . Abstraction was not allowed for  $n = 0$ , and the cross-section is taken to be isotope independent (*i.e.* it is the same for the abstraction of H and D atoms). The corresponding mass distribution is evaluated at each time step, and the theoretical fit is overlaid on the experimental fit. Several sets of cross-sections are attempted. The best fit to the data is found with a constant abstraction cross-section of  $\sigma_{abs}(n) = 0.01 \text{ \AA}^2$ , and an addition cross-section which was allowed to vary from 0.55 to  $2.00 \text{ \AA}^2$ . The resulting mass distribution is shown in Fig. 1.10.

At 2300 K the deuterium atoms have enough energy to overcome the barrier associated with hydrogenation (or deuteration) of graphite. Experiments have been carried out to see if coronene could become superhydrogenated through interaction with hydrogenated graphite [81]. First the HOPG surface was exposed to D atoms until a saturation coverage of 0.4 ML [32] was reached, after which the deuterated sample was exposed to coronene. It was found that the signal from  $D_2$  desorption was almost completely suppressed after a coronene coverage of less than half a ML, indicating that H atoms are released from the graphite surface as a result of coronene adsorption. The resulting mass distribution of coronene species is shown in Fig. 1.11.

The decay of the  $D_2$  signal as a function of coronene dose time can be seen in Fig. 1.12. It is clear from the figure that it does not take a full monolayer of coronene to completely suppress the  $D_2$  signal. Considering the number of D atoms available for reaction, and the number of coronene molecules on the surface, it can be calculated [32, 84, 85, 86, 87] that the average coronene

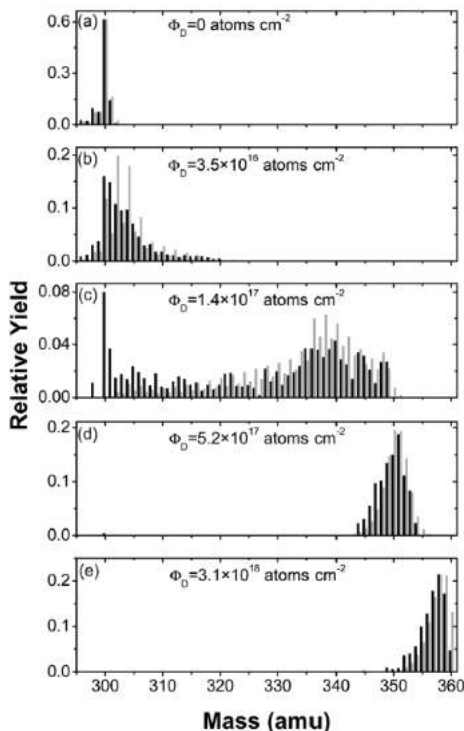


**Figure 1.10:** Kinetic simulations (grey) and experimental measurements (black) of the mass distributions of coronene exposed to D atoms at 2300 K, for different D atom fluences. Taken from [82].

molecule on the surface should pick up  $17 \pm 9$  extra deuterium atoms, corresponding to it reaching a mass of  $332 \pm 18$  amu. From the mass distributions shown in Fig. 1.11, this is clearly not the case. In fact, up to 90% of the deuterium is lost, most likely in abstraction reactions. Thus the experiment shows that PAHs can catalyse  $\text{H}_2$  formation from carbonaceous grains below the desorption temperature of superhydrogenated PAHs on graphite. From this experiment it is not possible to say at which temperature the reaction occurs, but coronene is expected to be mobile on graphite surfaces down to 100 K [84, 86], and smaller PAHs at even lower temperatures, suggesting this reaction could take place at very low temperatures.

The interaction between the hydrogenated coronene and the graphite substrate was studied by Skov et al. [83]. It was observed that pristine coronene and its hydrogenated counterparts desorb from the HOPG surface

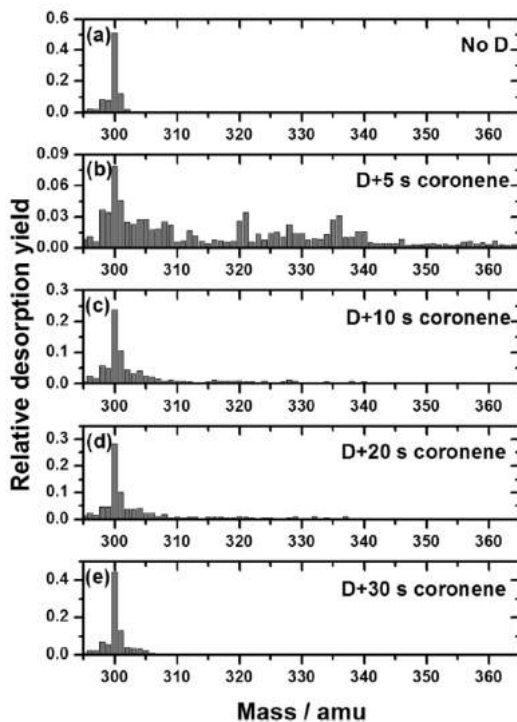


Figure 1.11: Mass distribution of coronene species after exposing deuterated graphite to coronene for various lengths of time [81].

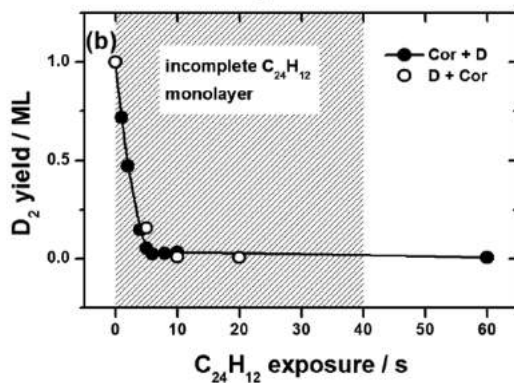
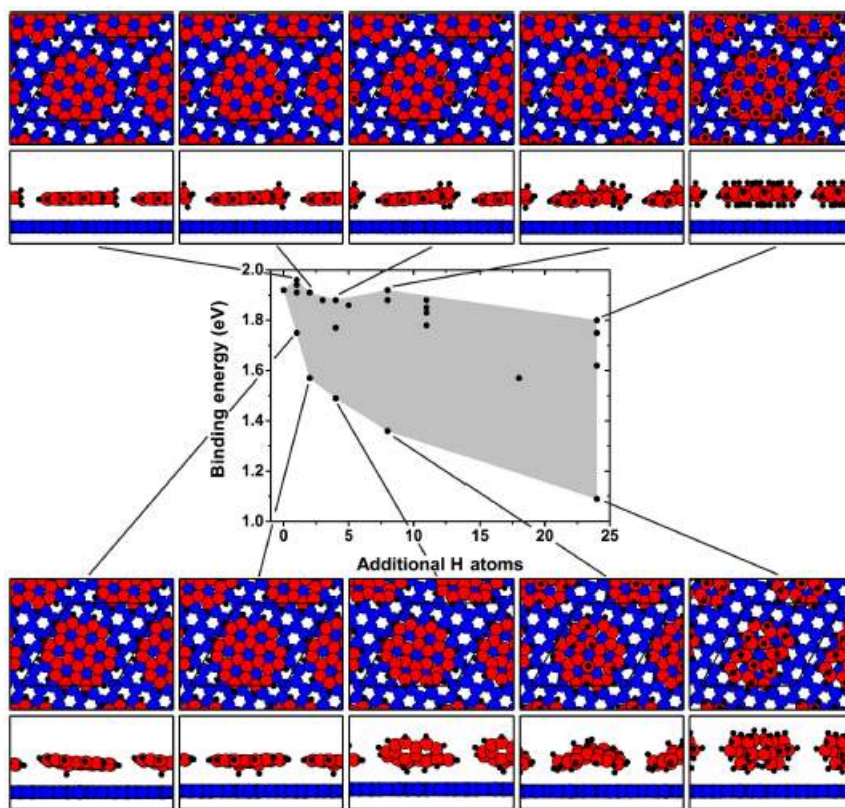


Figure 1.12: The decay of the  $D_2$  signal as a function of coronene dose [81]. The closed circles are for coronene dosed before D, and the open circles are coronene dosed after the graphite surface has been saturated with deuterium.



**Figure 1.13:** DFT calculations of the desorption energy for different configurations of superhydrogenated coronene, showing the interval in which the desorption energy is expected to lie for any configuration [83].

at different temperatures. Desorption of a pristine coronene monolayer from HOPG peaks at  $T_p = 465$  K, while masses 302 amu and 304 amu (corresponding to coronene with one and two added D atoms respectively) desorb at 448 and 432 K respectively. Aside from a decrease in desorption temperature, a decrease in signal was also observed. The decreased signal can be explained, in part, by the broadened molecular distribution, but a loss of molecules during the deuteration process must also be taken into account, as losses upwards of 75% have previously been observed [82].

The desorption of the superdeuterated coronene molecules follow first order kinetics, and thus the desorption energy can be found using the Red-head equation (discussed in Chapter 4). For low deuteration states a rapid

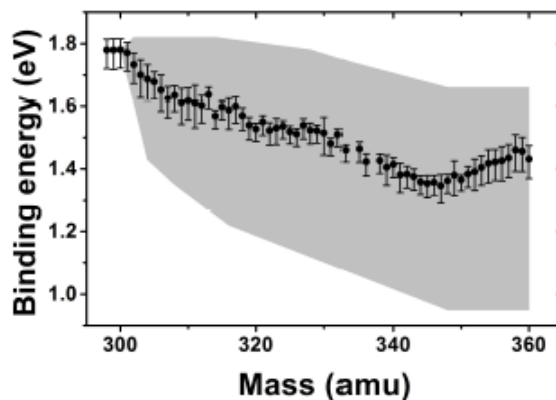


**Figure 1.14:** The experimentally measured binding energies of superdeuterated coronene molecules, overplotted on the interval in which the binding energies are expected from DFT calculations to be found (after applying a correction factor) [83].

decrease in  $E_{des}$  from 1.78 eV to 1.55 eV was seen. This levels out somewhat, but continues to decrease until a mass of 347 amu, where the desorption energy reaches a minimum at 1.34 eV. From here it increases again, to 1.43 eV at 360 amu (fully superdeuterated coronene). DFT calculations were performed for several different configurations of superhydrogenated coronene, resulting in a range of different desorption energies. These are shown in Fig. 1.13. The experimentally measured desorption energies are plotted with the theoretically expected interval after applying a correction factor in Fig. 1.14. The general decrease in desorption energy is expected due to the removal of  $\pi$ -electrons from the molecules, resulting in a change in the hybridisation, and because the molecule buckles to relax, reducing the area in close proximity to the graphite surface [80].

The hydrogenation and deuteration of coronene has also been studied using IR spectroscopy [88]. Here multilayers of coronene (of thickness 150–180 nm) were deposited on a CsI substrate. The coronene films were then exposed to a beam of deuterium atoms with a kinetic temperature of 300 K, and the changes in the IR spectrum were measured. These are shown in Fig. 1.15, where in (a) the evolution of the aromatic C-H out-of-plane (oop), C-H in-plane (ip), and C=C stretch transitions can be seen. These are all observed to decrease with increasing D fluence with a reaction cross-section of roughly  $1.1 \text{ \AA}^2$ . This is exactly what is expected when changing the hy-

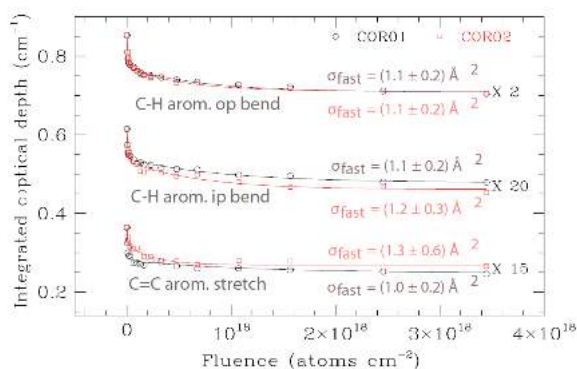
bridisation of the coronene molecules from  $sp^2$  to  $sp^3$ , and thus changing their nature from aromatic to aliphatic. In Fig. 1.15(b) the evolution of the aliphatic C-H and C-D stretch vibrations are shown. Here the aliphatic C-H stretch is first observed to increase rapidly, and then start to decrease. The aliphatic C-D stretch is observed to gradually increase with D fluence. This is due to abstraction of H from the molecule by D. After superdeuteration the coronene films were exposed to a hydrogen atom beam. This caused a decrease in the intensity of the aliphatic C-D stretch transition and a corresponding increase in the intensity of the aliphatic C-H stretch transition. This is shown in Fig. 1.15(c). The abstraction cross-section was estimated to be  $\sigma_{abs} = 0.06 \pm 0.02 \text{ \AA}^2$ . This value is much higher than that found in the kinetic simulations of [82]. One explanation for the discrepancy may be the difference in atomic gas temperature and excitation state. Where Skov et al. [82] use a thermal cracker resulting in atoms in the electronic ground state at a temperature of 2300 K, Mennella et al. [88] use a microwave plasma discharge source, resulting in excited atoms at room temperature.

The same bands studied in this experiment can be found in astronomical PAH spectra (see Fig. 1.6), and the variation in band strengths and positions between objects can potentially be used in combination with these experimental measurements to determine the degree of aromaticity in the emitting populations in the ISM.

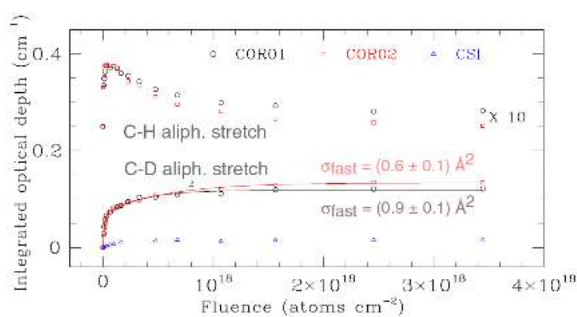
### Spectral Characteristics

Bernstein et al. [42] studied the 3.13 - 3.70  $\mu\text{m}$  spectral characteristic of superhydrogenated PAHs isolated in a solid Ar matrix in relation to astronomical PAH spectra. They found that as PAHs go from being completely aromatic and become more aliphatic in nature, the aromatic CH stretch band at  $\sim 3.3 \mu\text{m}$  gets weaker, while an aliphatic CH stretch band at  $\sim 3.4 \mu\text{m}$  starts to appear. Superhydrogenated PAHs are often not completely aromatic or aliphatic, and both types of features are therefore seen in their spectra, their strengths depending on the level of superhydrogenation of the molecule. The wavelength of the aliphatic CH stretch band was also found to depend on level of superhydrogenation, as well as the position of the excess atoms. A higher level of hydrogenation results in a longer wavelength of the aliphatic feature.

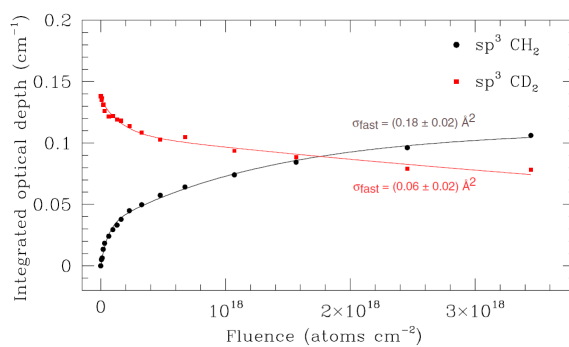
The authors compare the matrix isolation spectra of a sample of super-



(a)



(b)



(c)

**Figure 1.15:** (a) The evolution of the aromatic C-H out-of-plane bend, C-H in-plane bend, and C=C stretch bands, (b) and the aliphatic C-H and C-D stretch bands. (c) The evolution of the aliphatic C-H and C-D stretch bands during subsequent hydrogenation. Adapted from [88].

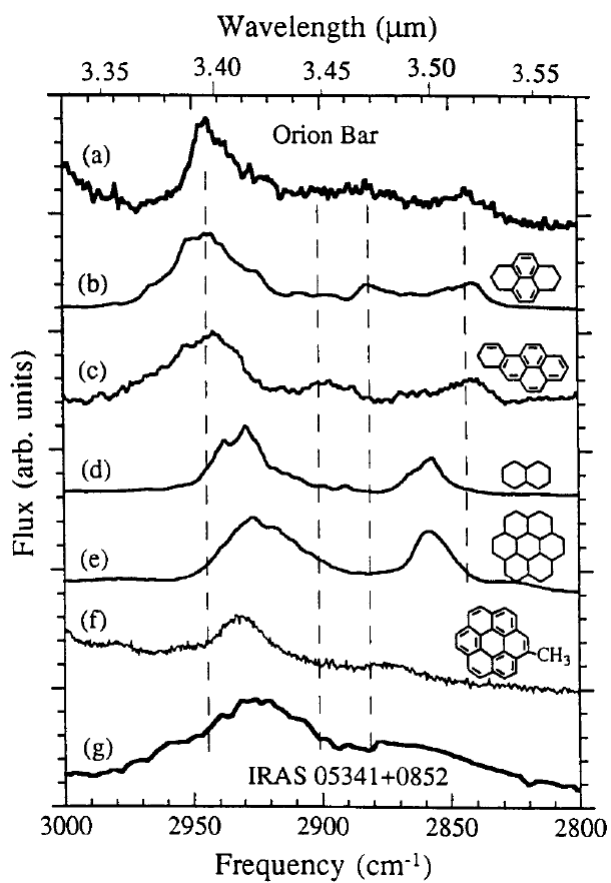


**Figure 1.16:** The spectra in the aliphatic CH stretch region of Orion Bar and IRAS 05341+0852, and a sample of superhydrogenated PAHs. From [42].

hydrogenated PAHs to two astronomical spectra of the Orion Bar PDR and IRAS 05341+0852 respectively. The result is shown in Fig. 1.16. Orion bar shows only a weak feature attributable to aliphatic material around  $3.4 \mu\text{m}$ , whereas IRAS 05341+0852 shows a stronger, broader aliphatic feature at a longer wavelength. The spectra of superhydrogenated PAHs are plotted between the astronomical spectra in an evolutionary sequence going from little to full superhydrogenation. It is clear that as the level of superhydrogenation of the PAH molecules increase, so does the wavelength of the aliphatic CH stretch feature, leading the authors to conclude that there is a larger presence of aliphatic material in IRAS 05341+0852 than in Orion Bar.

Sandford et al. [43] also investigated the IR spectra of a large sample of superhydrogenated PAHs (mainly naphthalene, anthracene, pyrene, and coronene derivatives) isolated in a solid Ar matrix. They mention three regions in the IR in which differences between aromatic and aliphatic features are observable,  $3\text{-}4 \mu\text{m}$ ,  $11\text{-}16 \mu\text{m}$ , and  $6.7\text{-}6.99 \mu\text{m}$ . First there is the CC stretch region also mentioned above. For regular, fully aromatic PAHs, the CH stretch feature has a wavelength between  $3.13$  and  $3.33 \mu\text{m}$ , but as the molecule becomes more aliphatic methylene groups appear giving rise to features between  $3.33$  and  $3.70 \mu\text{m}$ . As the molecules become more aliphatic the original features are weakened and the aliphatic features grow stronger. CH out-of-plane (oop) bending transitions occur in the region  $11\text{-}16 \mu\text{m}$ . These transitions provide important information about the structure of the PAH molecules, both aromatic and aliphatic, since the frequency of the oop bending modes are influenced by the neighbouring CH units on an aromatic ring. Adding excess hydrogen atoms to a PAH causes the aromaticity of the ring to be disrupted, and new features to arise, while some of the features associated with aromatic molecules disappear. The frequencies of the new bands depend on the location of the excess atoms as well as the number of atoms added to the molecule. The region between  $5$  and  $10 \mu\text{m}$  contains a range of bands attributed to CH in plane (ip) bending transitions and multiple CC transitions, however, in traditional PAHs the region between  $6.76$  and  $6.99 \mu\text{m}$  is mostly empty. When excess hydrogen atoms are added a strong band associated with methylene scissoring transitions appear at approximately  $6.9 \mu\text{m}$ , the position of which doesn't vary greatly with degree of superhydrogenation. As it is a strong band appearing in an otherwise empty part of the PAH spectrum, the authors suggest that it might be a good tracer for superhydrogenated PAHs in space, although it is worth not-

ing that it is virtually indistinguishable from the the feature appearing in linear aliphatic hydrocarbon chain molecules, resulting in a chance of cross contamination in astronomical spectra.

## PAH Ions

The interaction with hydrogen atoms has also been studied for PAH cations, both theoretically and experimentally. Bauschlicher [89] suggested that small PAH cations are quickly hydrogenated, and used DFT calculations of addition and abstraction of hydrogen and deuterium on naphthalene cations showed a low to no barrier for addition of the first two atoms. The reaction is highly exothermic, which could render small PAHs unstable, as the release of energy might be enough to dissociate the molecule. Abstraction of  $H_2$  by an incoming H atom is found to have a very small barrier of 11 meV, while abstraction of HD has a somewhat larger barrier of 29 meV. This could potentially lead to a deuterium enrichment of PAHs.

Similar results were found for anthracene and pyrene by Hirama et al. [90]. The calculations for naphthalene were revisited by Ricca et al [91], and the results were close to those of Bauschlicher [89]. A barrier of 30 meV was found for the addition of a second atom only. Higher degrees of hydrogenation were also studied, and it was found that once a second atom was added, further hydrogen additions to all secondary carbon atoms could proceed with no barriers.

The reaction rates for hydrogenation of naphthalene cations were studied for the first two additions by Le Page et al. [92]. They found rate constants of  $1.9 \times 10^{-10} \text{ cm}^3 \text{ s}^{-1}$  and  $4.0 \times 10^{-12} \text{ cm}^3 \text{ s}^{-1}$  for the first and second additions respectively. Snow et al. [93] studied the same reaction rates for the pyrene cation, with similar results, finding rate constants of  $1.4 \times 10^{-10} \text{ cm}^3 \text{ s}^{-1}$  for the first addition and  $3.0 \times 10^{-12} \text{ cm}^3 \text{ s}^{-1}$  for the second.

The hydrogenation of pentacene cations was studied by Klærke et al. [94], using both experiments and DFT calculations. They found that the molecule can be driven to complete hydrogenation of the secondary carbon atoms, but that the tertiary carbon atoms remain unhydrogenated. Furthermore, a difference was found in the yield of molecules with an odd number of added H-atoms, and an even number of added atoms. Specifically, the yield was significantly higher for molecules with an odd number of added atoms, suggesting that these molecules are more stable than those with an even

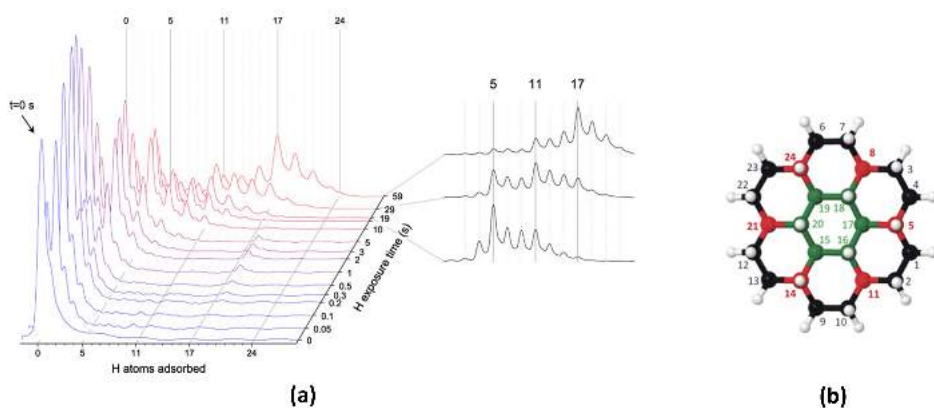


**Figure 1.17:** The mass distribution of coronene cations, having been exposed to different fluences of hydrogen atoms (a), with three highest fluences highlighted, and an illustration of the lowest energy hydrogenation route of the coronene cation (b). Figure modified from [95]

number of excess atoms. This fits with the additional atoms making the system closed shell. The opposite situation is true for neutral PAHs, where the even numbered additions are expected to be more stable.

The hydrogenation of coronene cations has also been studied both theoretically and experimentally, by Boschman et al. [96]. They found, in agreement with [94], that molecules with an odd number of added atoms were more stable than those with an even number of added atoms. They also determined the barriers for addition of the 2nd and 4th atoms to be 72 meV and 40 meV respectively, while the 1st and 3rd additions were found to have no barriers. These studies were followed up by Cazaux et al. [95], who included DFT calculations, estimating the barriers involved in the reactions. They confirmed the higher stability of odd numbered additions experimentally, and found that the 5th, 11th, and 17th additions showed an extra high degree of stability. The mass distributions of the hydrogenated coronene cations for different fluences are shown in Fig. 1.17(a). The lowest energy addition route was calculated using DFT, and is shown in Fig. 1.17(b). After addition of the first couple of atoms the route differs significantly from that of neutral coronene [74]. The largest barriers to addition were found to be those for the 6th, 12th, and 18th additions, and have values of 110, 170, and 320 meV respectively.

The desorption of molecular hydrogen from superhydrogenated PAH cations has also been investigated. Vala et al. and Szczepanski et al. [97, 98] studied IR-multiphoton dissociation of 1,2-dihydronaphthalene, acenaphthalene, and 9,10-dihydrophenanthrene cations. In all cases loss of two hydrogen atoms was observed, and DFT calculations found a lower barrier for  $H_2$  loss, compared loss of two hydrogen atoms. Exposure of PAH cations to UV radiation from 7-40 eV was investigated by Zhen et al [99, 100]. They found that the UV radiation caused large PAHs to become doubly ionised, while small PAHs lost two hydrogen atoms, though whether the loss occurred as a molecule or two separate atoms was not determined.

Dissociation of hydrogenated PAH cations has also been studied through collisions with high energy He cations [101, 102, 103] by Chen et al. Perhaps the most interesting result was found in [102], where it is shown that  $H_2$  loss becomes important once the internal temperature of the PAH molecule becomes higher than approximately 2200 K, regardless of PAH size and excitation mechanism.

Many PAHs have a range of negative health effects. They are toxic, carcinogenic, and teratogenic [104], and are therefore unwanted pollutants in *e.g.* car exhaust, power plants, factories, etc. It is possible that removing the aromaticity from the molecules will help reduce the negative health effects associated with the molecules, and hydrogenation has also been studied in this context [70, 71, 72].

## 1.4 Fullerenes

Buckminster Fullerene,  $C_{60}$ , was discovered by accident, during experiments aimed at understanding the carbon chemistry taking place in the warm dense surroundings of evolved stars by Kroto et al. [105]. In the experiment carbon species were vaporised from a solid graphite disk into a high density helium flow using a focused pulsed laser. The resulting carbon clusters were then expanded in a supersonic molecular beam and the products detected using time-of-flight (TOF) mass spectrometry. The authors found that for clusters larger than 40 carbon atoms only clusters with an even number of atoms were detected, and the clusters containing exactly 60 carbon atoms dominated the mass spectra. Under certain expansion conditions the  $C_{60}$  peak

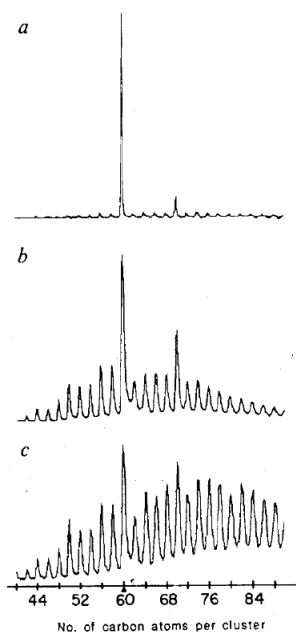


**Figure 1.18:** The TOF mass spectra of carbon clusters prepared from laser vaporisation of graphite, followed by cooling in supersonic molecular beam. As the density of helium present during vaporisation changes, so does the relative strengths of the peaks. The higher the density of helium, the stronger the  $C_{60}$  peak. From [105].

could be up to 40 times as large as neighbouring peaks. This is shown in Fig. 1.18.

The  $C_{60}$  molecule must therefore be very stable, and hence, when considering plausible structures only one stands out - that of a spheroidal truncated icosahedron [105]. If the molecule was flat, consisting of fused rings it would have unsatisfied valences at the edges, and if it had a tetrahedral diamond structure its entire surface would be covered in unsatisfied valences. The only structure that satisfies all  $sp^2$  valences is the truncated icosahedron (or 'football' shape). The structure is aromatic, with the inner and outer surfaces covered in clouds of  $\pi$ -electrons, and the diameter of the molecule is approximately 7 Å. Even at this early stage Kroto et al. speculated that, due to its remarkable stability, the molecule would be abundant in interstellar space and in the circumstellar environments of evolved stars.

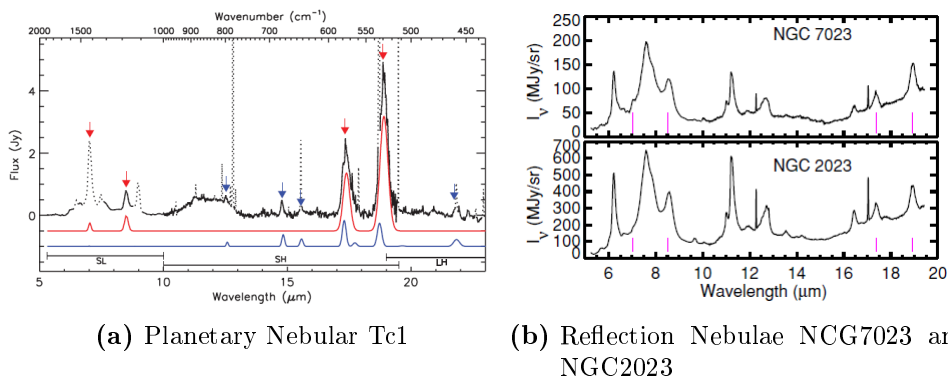


**Figure 1.19:** In (a) the continuum subtracted 5-23  $\mu\text{m}$  spectrum of the planetary nebula Tc1. The red arrows indicate features arising from  $\text{C}_{60}$ , and the blue arrows the four strongest features from  $\text{C}_{70}$ . The red and blue curves correspond to model spectra of  $\text{C}_{60}$  and  $\text{C}_{70}$  at temperatures of 330 and 180 K respectively. Adapted from [14]. In (b) the 6-20  $\mu\text{m}$  spectra of the reflection nebulae NGC7023 (upper panel) and NGC2023 (lower panel), with vertical lines indicating the positions of  $\text{C}_{60}$  features. From [107].

### 1.4.1 Fullerenes in the ISM

Fullerenes were not, however, definitively identified in the ISM until 2010. The  $\text{C}_{60}$  cation was proposed as a plausible carrier for two diffuse interstellar bands (DIBs) in the near IR in 1994 by Foing and Ehrenfreund [106], due to their proximity in wavelength to absorption features of  $\text{C}_{60}^+$  in a solid Ne matrix. However, in order to confirm this hypothesis laboratory measurements of gas phase  $\text{C}_{60}^+$  were needed, and these were not available at the time.

The neutral fullerenes  $\text{C}_{60}$  and  $\text{C}_{70}$  were identified in the peculiar planetary nebula Tc1 in 2010 by Cami et al. [14]. The PN is peculiar as it shows no trace of even simple H-carrying species, and has no PAH features. Instead the spectrum is dominated by four IR features at 7.0, 8.5, 17.4, and 18.9  $\mu\text{m}$ , attributed to neutral  $\text{C}_{60}$ , and also shows weaker features attributed to  $\text{C}_{70}$ . The continuum-subtracted mid-IR spectrum of Tc1 is shown in Fig. 1.19(a), with red and blue arrows indicating the features attributed to  $\text{C}_{60}$  and  $\text{C}_{70}$  respectively.

Aside from the peculiar Tc1,  $\text{C}_{60}$  has also been identified in the planetary nebulae NGC7023 and NGC 2023 [107]. The spectra of these two PNe are

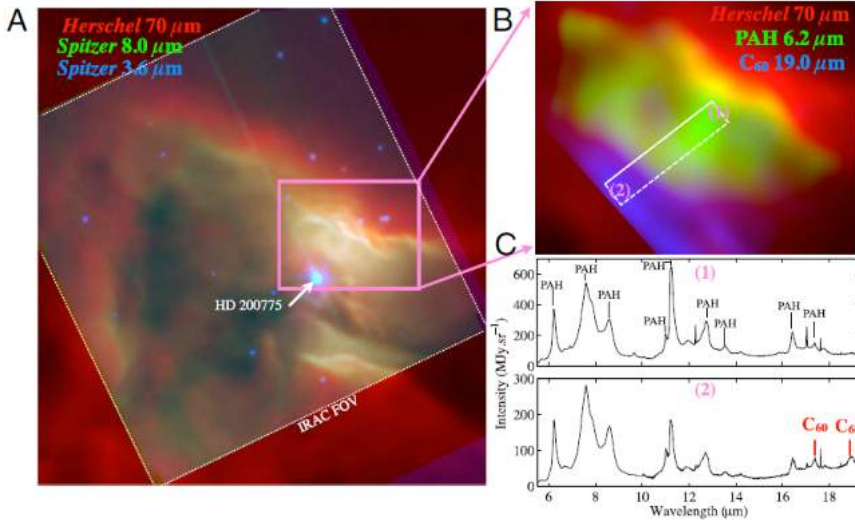


**Figure 1.20:** The reflection nebula NGC7023. Spectra are shown of two regions in the nebula taken at different distances from the star, and show the evolution from PAH emission far from the star to fullerene emission closer to the star. From [111]

shown in Fig. 1.19(b), with the  $C_{60}$  features indicated by short vertical lines.

It has been suggested that fullerenes in space form in the hot, dense envelopes of evolved stars, in processes similar to soot formation, and are eventually ejected into interstellar space. However the problem with this process is its limited efficiency [108, 109, 110].

Another possible formation route has been suggested in which fullerenes are formed in the ISM [111, 112]. PAHs and fullerenes are known to coexist in the ISM, but a distinct difference in their spatial distribution has been observed in the reflection nebula NCG7023 [107, 111]. Deep in the cloud the emission is dominated by clusters of PAHs which, further out, where the UV field is stronger, are evaporated into free-flying neutral PAHs and then ionised. In regions closer to the nascent star the spectrum is dominated by emission from  $C_{60}$ . In fact, the abundance of  $C_{60}$  increases towards the star, from accounting for  $1.4 \times 10^{-4}\%$  of the available carbon to  $1.7 \times 10^{-2}\%$ , while at the same time the abundance of PAHs decrease from carrying 7.0% of the available carbon to 1.8%. The spatial evolution of the spectra are illustrated in Fig. 1.20.

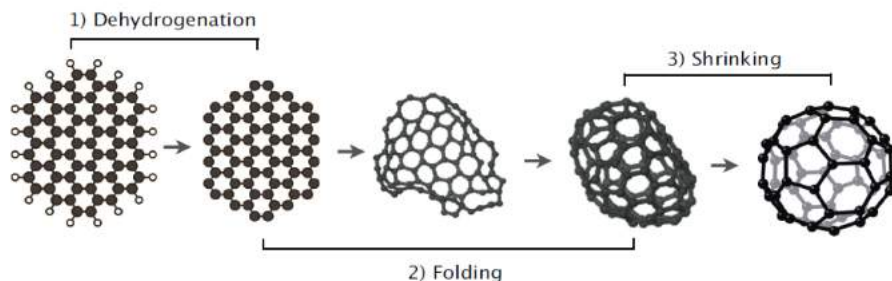


**Figure 1.21:** Alternative formation route of fullerenes in the ISM, involving the chemical processing of PAHs. PAHs are dehydrogenated, and then loose carbon atoms, creating pentagons and making the molecules close up. Once the cage is closed it shrinks through loss of  $C_2$ , eventually leading to formation of stable fullerenes. From [112].

This chemical evolution provides evidence that  $C_{60}$  is formed and PAHs are destroyed in the ISM, and the correlation with the UV field is a strong suggestion that UV photons control the process. The authors, therefore, propose a top-down formation process as shown in Fig. 1.21. When the UV field increases PAHs become dehydrogenated creating small graphene flakes, which in turn start to lose carbon atoms. This carbon-loss causes pentagons to form in the graphene flakes, causing it to curl up. The cage then closes up and shrinks through  $C_2$ -loss until stable fullerenes, probably mainly  $C_{60}$  and  $C_{70}$ , are reached.

The evolution over time of the abundance of large PAHs and a number of carbon-cage structures (including  $C_{60}$ ) is shown for different distances from the central star in Fig. 1.22 [112, 113]. The abundance of  $C_{60}$  is seen to decrease after some millions of years, however the route to their the molecule's dissociation in the ISM is unknown. One possibility is that hydrogenation of the molecule weakens the carbon skeleton sufficiently for FUV photons to dissociate it. Experiments to test this hypothesis, and their results will be discussed in chapter 4.

## Fullerenes and the Diffuse Interstellar Bands

As mentioned above, the  $C_{60}$  cation was suggested to be the carrier of two DIBs at  $9632 \text{ \AA}$  and  $9577 \text{ \AA}$  as early as 1994 [106], owing to their proximity to absorption bands of  $C_{60}^+$  in a solid Ne matrix. However, in order to ultimately confirm this assignment, gas phase spectra were required. The

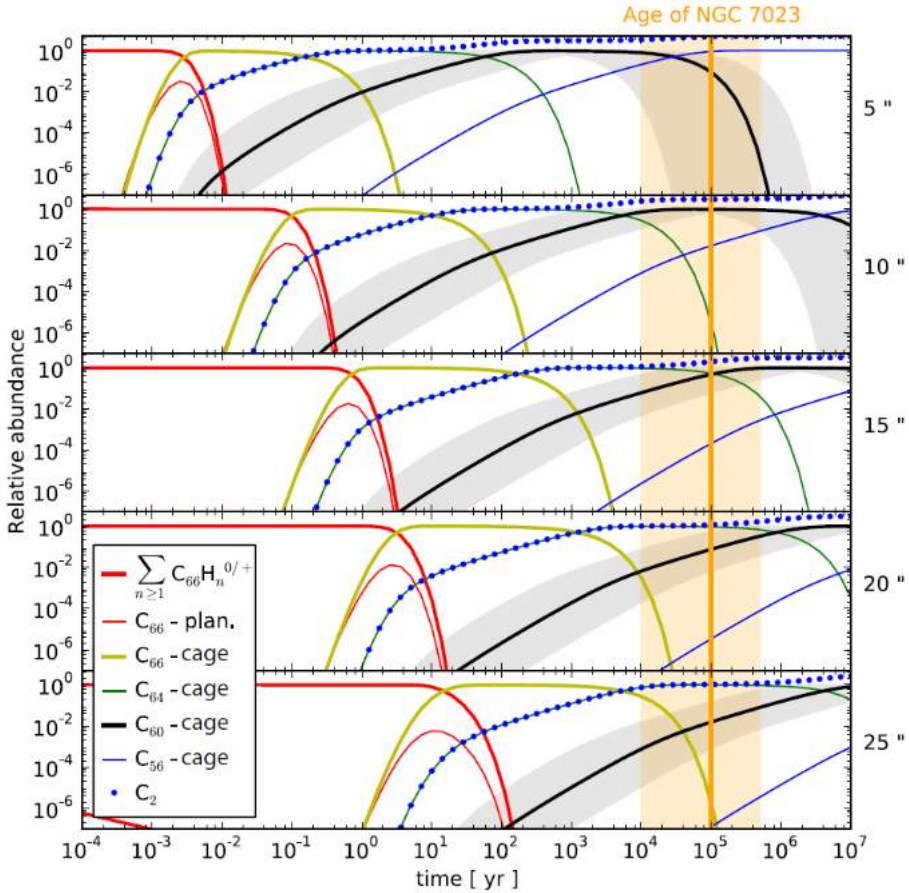


**Figure 1.22:** Calculated time-evolution in the abundance of large PAHs and a sample of carbon cages, assuming fullerenes form from PAH precursors, at various distances from the star in NCG7023. The approximate age of NCG7023 is noted by the orange region. From [112].

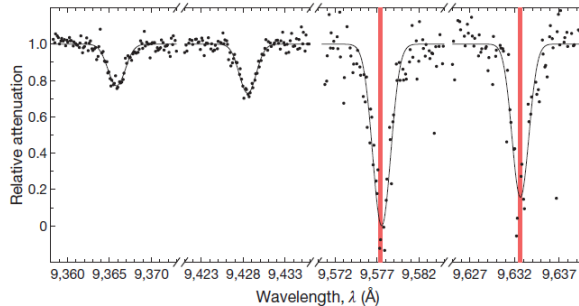


**Figure 1.23:** The experimentally measured absorption spectrum of  $C_{60}^+$ , with the position of the DIBs at 9632 and 9577 Å superimposed, confirming the  $C_{60}$  cation as the carrier of those two DIBs. From [114].

gas phase spectrum of  $C_{60}^+$  was measured by Campbell et al. in 2015 [114], and they found absorption features at  $9632.7 \pm 0.1$  Å and  $9577 \pm 0.01$  Å with full width half maxima (FWHM) of  $2.2 \pm 0.2$  and  $2.5 \pm 0.2$  Å, respectively, with the band at 9577 Å being the strongest. They also observed two weaker bands at  $9428.5 \pm 0.1$  and  $9365.9 \pm 0.1$  Å both with FWHM of  $2.4 \pm 0.1$  Å. These weaker bands do not correspond to any known DIBs, but with strengths of 0.3 and 0.2 times that of the 9577 Å band respectively, it is possible that they are too weak to be detected in the diffuse ISM. The absorption bands of  $C_{60}^+$  are shown in Fig. 1.23, along with the DIBs coinciding with the two stronger bands. The identification of  $C_{60}^+$  as the carrier of the two DIBs has since been called into question [115].

# Chapter 2

## Experimental Setups and Techniques

*Finally from so little sleeping and so much reading, his brain dried up and he went completely out of his mind.*

— Miguel de Cervantes Saavedra, *Don Quixote*

There are two main parts to the experiments involved in this project. The temperature programmed desorption (TPD) experiments with superhydrogenated and -deuterated PAHs were carried out on the Big Chamber in the Surface Dynamics Laboratory (SDL) at Aarhus University, while the scanning tunnelling microscopy (STM) and the experiments with hydrogenated fullerenes were carried out at the Coal Chamber, also at SDL. All TPD and flux measurement experiments were carried in close collaboration with former PhD student Anders Witte Skov and current PhD student Frederik Doktor Skødt Simonsen, while the fullerene STM experiments on the coal chamber were performed in collaboration with postdoc Dr Martha Scheffler.

### 2.1 The Big Chamber

The Big Chamber is an ultra-high vacuum (UHV) setup, originally from IBM, that was moved first to Syddansk Universitet in Odense and then to Aarhus, in 2007. It has a base pressure of between  $10^{-10}$  and  $10^{-9}$  mbar, maintained by a turbomolecular pump and an additional titanium sublima-

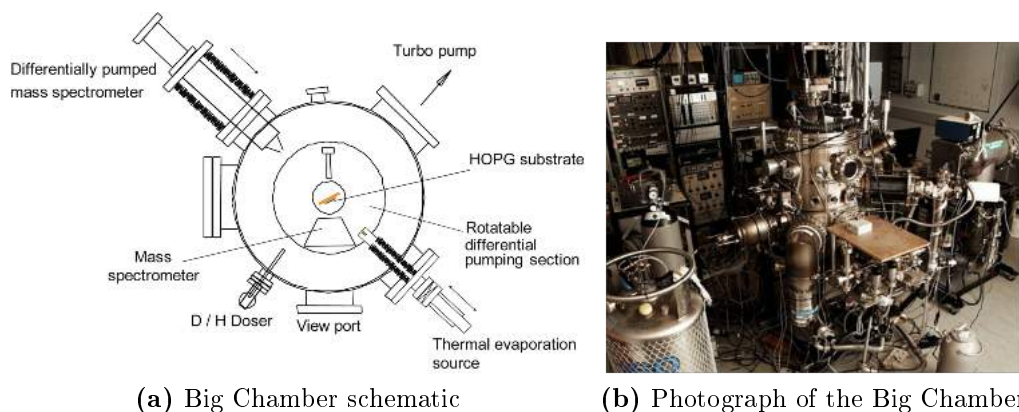


**Figure 2.1:** Schematic (a) and photograph (b) of the Big Chamber in the Surface Dynamics Laboratory.

tion pump (TSP). A series of differential pumping stages pump the regions which are not sufficiently pumped by the main chamber, *e.g.* the mass spectrometer enclosures. The chamber is equipped with a manipulator, which is rotatable through  $360^\circ$  and can be moved in three dimensions, and on which is mounted a tantalum (Ta) sample holder. The manipulator is normally water cooled to approximately  $18^\circ\text{C}$ , but it is also possible to cool it using liquid nitrogen ( $\text{LN}_2$ ) to reach even lower temperatures. The sample can be heated through electron bombardment of the back of the sample, by passing a current through a tungsten (W) filament and biasing the sample holder with 500-1000 V relative to said filament. This allows for the sample to be heated as high as 1300 K, as measured by a C-type thermocouple squeezed between the backside of the sample and the sample holder. The temperature of the sample can be controlled accurately by a model 340 LakeShore PID temperature controller. A schematic as well as a photograph of the chamber can be seen in Fig. 2.1.

Molecules can be deposited on the sample using a home-built Knudsen cell evaporation source, and the film can be subsequently hydrogenated. This is achieved by passing  $\text{H}_2$  or  $\text{D}_2$  (Air Liquide,  $> 99\%$ ) through a hydrogen atom beam source (HABS), a hot capillary source similar to that described by Tschersich et al. [116, 117, 118], dissociating the molecules and resulting in an atomic beam with a kinetic temperature of 2300 K. A custom made quartz cooling nozzle can be attached to the doser, as shown in Fig. 2.2, and this cools the atoms to a kinetic temperature of approximately 1000 K

through collisions with the walls.

The kinetic energy of the atoms is estimated assuming inelastic collisions of the atoms with  $\text{SiO}_2$ , the molecular unit of quartz, and found from

$$\frac{E_{scat}}{E_i} = \frac{(M - m)^2}{(M + m)^2},$$

where  $E_{scat}$  is the kinetic energy of the atom after a collision and  $E_i$  is the kinetic energy of the same atom prior to the collision.  $M$  is the molecular mass of  $\text{SiO}_2$  and  $m$  the mass of the atom. For deuterium this gives a ratio of kinetic energies of 0.88, *i.e.*, an incoming deuterium atom loses 12% of its kinetic energy per collision. The fractional loss in kinetic energy can be directly related to a loss in temperature through  $E_{kin} = k_B T$ . Assuming a minimum of 4 collisions the atoms will be cooled to a temperature of  $\simeq 1000$  K.

Two quadrupole mass spectrometers (QMS) are attached to the chamber to monitor desorption products upon heating of the sample, both differentially pumped. The Pfeiffer Vacuum Prisma QMS operates within a mass range of 1 - 200 amu, and is mainly used for rest gas measurements, leak testing, and hydrogen and deuterium desorption experiments. The Extrel CMS LLC QMS has a cross-beam ion source and is rotatable and operates in a range of 1- 500 amu. This is the QMS used in the PAH desorption experiments. Furthermore the chamber is equipped with a sputter ion gun, Auger electron spectroscopy (AES), and low energy electron diffraction (LEED).

## 2.2 The Coal Chamber

The Coal Chamber, where the fullerene STM experiments have been performed is also located in SDL. It is primarily used for STM, though it is equipped with a variety of instruments. The STM in the Coal Chamber is an Aarhus STM [119]. It is normally run at room temperature, although it is possible to cool it using liquid nitrogen. Aside from the STM the chamber is also equipped with a sputter gun, LEED, a QMS with a range up to  $\frac{m}{z} = 500$ , a hydrogen cracker similar to the one on the Big Chamber, and a vacuum UV (VUV) source. The UV source is a Krypton Line Source with a MgF2 window from Resonance Ltd (model: KrLM-LQD12), and emits at 123.6 and 116.5 nm, *i.e.* just on either side of the Ly- $\alpha$  line at 121.6 nm.



**Figure 2.2:** Short cooling nozzle mounted on the hydrogen doser.

The chamber also has a manipulator, rotatable through  $360^\circ$ , and equipped with a tungsten filament for sample heating.

In the STM experiments performed on the Coal Chamber two samples were used, a cleaved HOPG crystal and a foil of Au(111) on Mica. Measurements were done using STM, although the sputter gun was used to clean the gold foil.

## 2.3 Temperature Programmed Desorption - TPD

The main experimental technique used in this project TPD, and it has been used in the PAH experiments and the atomic flux calibration, but also. The process of TPD is shown in Fig. 2.3. A layer of molecules, in our case coronene, is deposited on a HOPG surface. The layer of molecules is subsequently exposed to a beam of hydrogen or deuterium atoms for a set amount of time. The sample is then heated in a controlled manner at a rate of  $1 \text{ Ks}^{-1}$  in front of the mass spectrometer, and the desorption products are

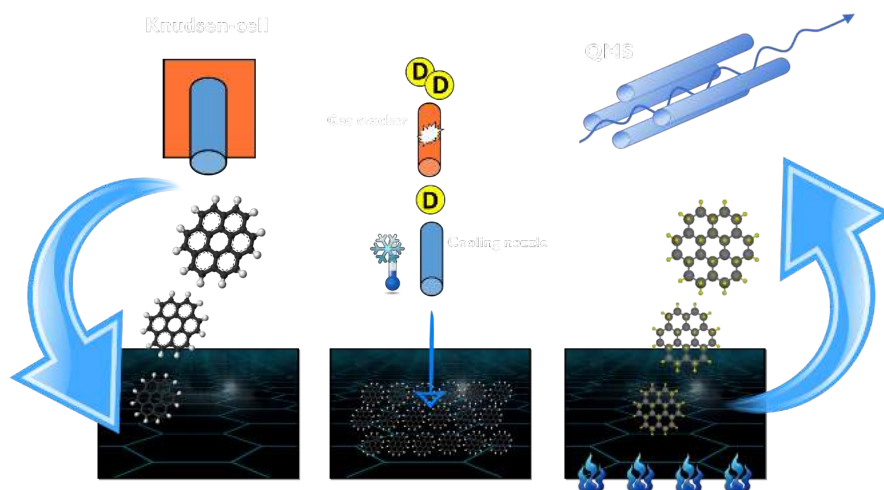


**Figure 2.3:** Illustration of the experimental method used in the TPD experiments. Credit: Frederik D. S. Simonsen.

detected. Beyond product mass distribution, TPD can provide very valuable information about the interaction between an adsorbate and a substrate. It is possible to study the strength of the bonds between the adsorbate and the substrate, the growth of adsorbate films on the substrate, and quantify the range of adsorption sites available in terms of energy using this technique.

### 2.3.1 Adsorption and Desorption

In order to understand TPD in general, it is necessary to first discuss the processes of adsorption and desorption. Adsorption is the process by which molecules or atoms stick to a surface, while desorption is the opposite, the process by which adsorbed species leave the surface. The following section is based mainly on [120].

Adsorption can be divided into two different categories, physisorption and chemisorption, depending on which type of bond is formed between the adsorbate and the substrate. The two types of adsorption are described in Fig. 2.4. Physisorption describes adsorption processes whereby the adsorbate is bound to the substrate by van der Waals interactions, where an induced dipole moment in the adsorbate interacts with the substrate. This type of

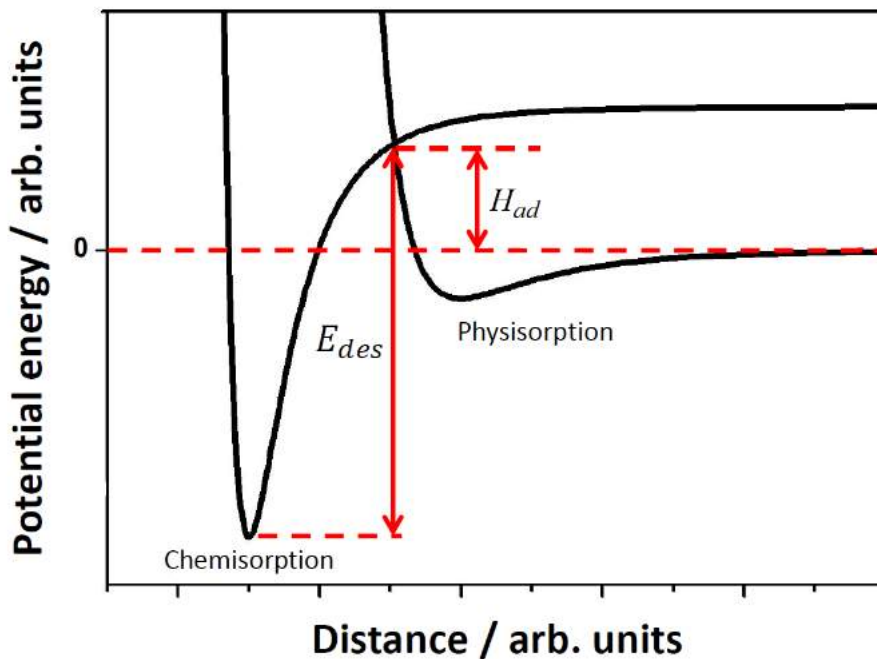


**Figure 2.4:** Potential energy curves illustrating the difference between chemisorption and physisorption. From [122].

adsorption is barrierless, and so any atoms and molecules are able to physisorb onto a surface, but the binding energy (BE) is usually only on the order of 50-500 meV or smaller [121]. For this reason, physisorption is generally only efficient for molecule formation at low temperatures. In some cases it is also a precursor to chemisorption.

In the case of chemisorption a chemical bond, *i.e.* a covalent, ionic, or metallic bond, is formed between the adsorbate and the substrate. This results in a much higher adsorption energy, generally on the order of 1-10 eV [121]. This type of reaction typically has an activation barrier, or heat of adsorption ( $H_{ad}$ ), which must be overcome. In some cases the adsorbate will dissociate on the surface and it is the fragments which adsorb. This is known as dissociative adsorption.

Desorption is the process by which an adsorbate leaves the surface. It is an activated process, which requires energy to be added to the adsorbate.

This can be in the form of increased temperature or through stimulation by electrons or photons. It is possible for reactions forming larger molecules to take place during the desorption process. This is known as associative desorption, and is the reverse of to the dissociative adsorption process.

An important parameter to consider when performing TPD experiments is film growth, the process by which layers of adsorbate are built up on the substrate. The absolute coverage of a surface, *i.e.* the number of atoms or molecules adsorbed on the surface, can be difficult to determine, and so one normally operates with relative coverage,  $\theta$ , the ratio of the number of occupied sites on the surface to the number of total sites on the surface. For a coverage of 1 monolayer (ML)  $\theta = 1$ .

Films can grow on a surface by different processes, depending on the relative strengths of the interaction between adsorbates, and adsorbate and surface. There are three different models which describe the types of growth that can occur.[123, 120]

1. Frank-van der Merve growth, also known as layer-by-layer growth. In this type of growth the interaction between the adsorbate and the surface is much stronger than that between adsorbates. This results in the formation of a full monolayer before multilayers start to grow.
2. Volmer-Weber growth, or island growth. In this type of growth the interaction between adsorbate and surface is much weaker than that between adsorbates, resulting in the formation of islands which are several layers thick, rather than the formation of a monolayer.
3. Stranski-Krastnov growth, or layer-plus-island growth. This is an intermediate type of growth to the other two, where the interaction between the adsorbate and surface is of the same approximate magnitude as that between adsorbates. As a result multilayers will start to grow before the monolayer is complete.

### 2.3.2 Thermally Induced Desorption

The desorption experiments described in this thesis were all performed using thermally induced desorption, rather than electron or laser induced desorption, and so only this will be discussed in detail. The process of thermally

induced desorption can be described using a rate equation known as the Polanyi-Wigner equation, where the rate of desorption is

$$r_{des} = -\frac{d\theta}{dt} = \nu\theta^n \exp\left[\frac{-E_{des}}{k_B T}\right].$$

Here,  $\nu$  is a pre-exponential factor, related to the change in entropy during desorption and  $n$  is the desorption order. It is often more useful to look at desorption as a function of temperature rather than time, so a linearly increasing temperature ramp is used. This allows for the desorption rate to be written as

$$\frac{d\theta}{dt} = \frac{d\theta}{dT} \frac{dT}{dt} = \frac{d\theta}{dT} \beta,$$

where  $\beta$  is the temperature ramp rate. From this the Polanyi-Wigner equation can be modified to

$$r_{des} = -\frac{d\theta}{dT} = \frac{\nu}{\beta} \theta^n \exp\left[\frac{-E_{des}}{k_B T}\right].$$

For this model to work we assume that the TPD signal measured by the QMS is proportional to the desorption rate. For this to be fulfilled a constant pumping speed, sufficiently high to prevent readsorption, is needed, which is normally achieved at UHV.

In order to determine the coverage of a surface, the TPD peak is integrated, and the area under the curve is compared to that of a known coverage (*e.g.* 1ML). The desorption order,  $n$ , is generally related to the number of steps involved in the desorption. First order desorption is typically associated with monolayer systems, where adsorbed atoms or molecules leave the surface individually. In this case, the rate of desorption only depends on the concentration of adsorbates on the surface. Second order desorption is also typically associated with monolayer systems, but where the adsorbates need to react to leave the surface, *i.e.* it is associated with associative desorption involving two partners. In this case the desorption rate is dependent on the concentration squared. Zeroth order desorption is associated with multilayer systems, where the influence from the surface becomes gradually negligible, until the bonding resembles that of a condensed bulk solid. Here the desorption rate is independent of concentration, and increases exponentially until all adsorbates have been desorbed.

The desorption order influences the shape of the TPD curve, because it

changes the dependency of the desorption rate on the peak desorption temperature. The peak temperature,  $T_P$ , is the temperature at which the desorption is at a maximum, i.e.

$$\frac{d^2\theta}{dT^2} = 0.$$

If the modified Polanyi-Wigner equation is differentiated and this criterion inserted, we get

$$\frac{E_{des}}{k_B T_P^2} = \frac{\nu}{\beta} n \theta^{n-1} \exp\left[\frac{-E_{des}}{k_B T_P}\right].$$

From this it is clear that for first order desorption,  $T_P$  is independent of the coverage, while in the case of 2nd order desorption,  $T_P$  decreases with increasing coverage.

When depositing coronene molecules on a HOPG surface the film grows according to layer-plus-island growth, *i.e.* multilayers start to grow before the monolayer is complete. Fortunately, the multilayers desorb at a lower temperature than the monolayer, so it is possible to deposit a full monolayer by dosing long enough to build up a few multilayers, then anneal the sample to a temperature just high enough to desorb the multilayers, leaving an intact and saturated monolayer on the surface. An example of this is shown in Fig 2.5.

The molecules leave the surface independently, making it a 1st order desorption process. In the case of coronene on HOPG, the molecules are physisorbed to the surface, and mobile at room temperature. In the case of hydrogen on silicon, which is used to calibrate the flux of the cracker, the atoms are chemisorbed to the surface, and immobile.

## 2.4 Scanning Tunnelling Microscopy - STM

Scanning tunnelling microscopy (STM) was developed by Heinrich Rohrer and Gerhard Binnig at IBM in the early 1980s [124, 125, 126], and it won them the Nobel Prize in Physics in 1986. The technique is based on quantum mechanical tunnelling and is used to provide three dimensional (3D) images of the electronic density of states of a surface at atomic scale resolution.

A quantum mechanical particle, such as an electron, is not completely confined by a finite potential barrier, but has a non-zero decay length into the

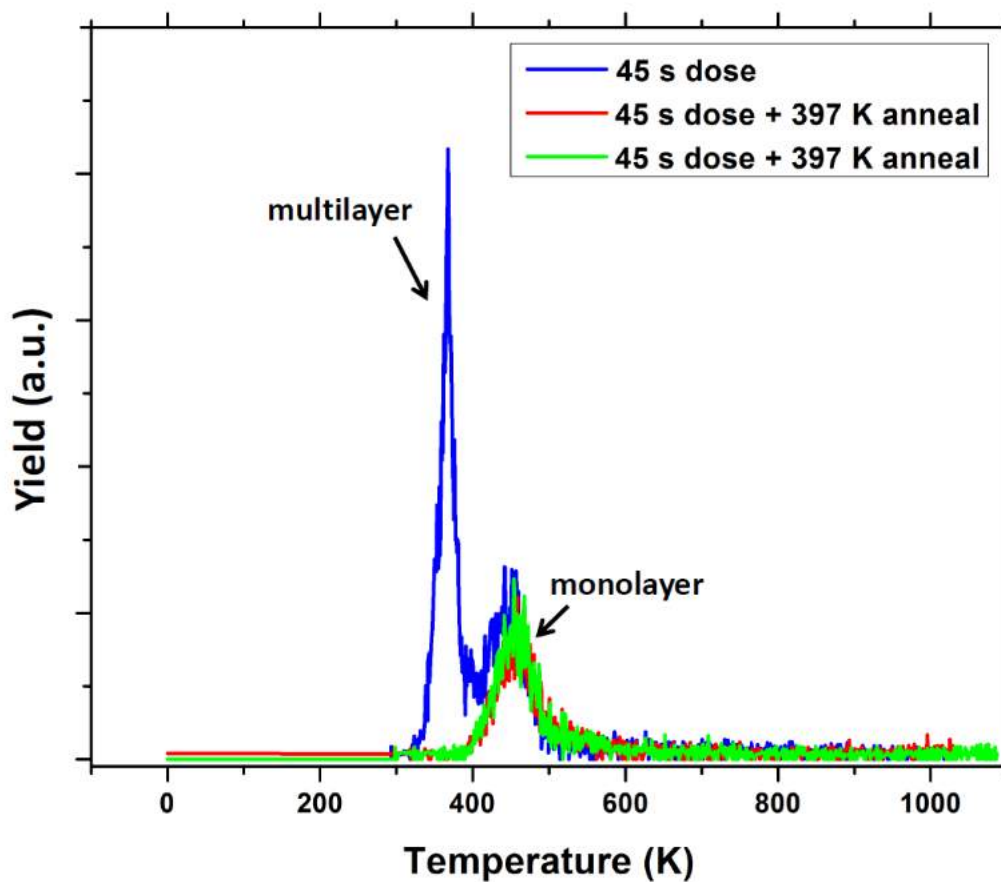


**Figure 2.5:** TPD curves of three 45 s doses of coronene on HOPG, two of them annealed to 397 K after dosing. This show how a consistent, saturated monolayer is deposited.

classically forbidden region. For a metal, this decay length is smallest at the Fermi energy, where the potential is given as the work function  $\Phi$ . The decay length can be described as

$$\kappa = \sqrt{\frac{2m_e\Phi}{\hbar^2}}.$$

STM works by placing a sharp metal tip at a distance,  $z$ , of a few Å above a conducting surface. If the tip and the surface are sufficiently close, the non-zero decay length of the electron wavefunction permits the transmission of electrons between the tip and the surface across the vacuum barrier. The wavefunction of the tip will then overlap with that of the surface, and thus electrons can tunnel over the vacuum barrier from tip to surface or vice versa. This rapid charge transfer will continue until an equilibrium is reached through alignment of the Fermi levels of the tip and surface. Now, if a voltage difference,  $V_t$ , is applied between the tip and the surface, the Fermi levels will shift, and electrons will tunnel from filled states in the tip to empty states in the surface, or vice versa, depending on the polarity of the applied voltage. This results in a constant measurable tunnelling current,  $I_t$ , which depends on the distance  $z$  between the tip and the surface [120],

$$I_t \propto e^{-2\kappa z}.$$

The STM used in the experiments described in this thesis is the Aarhus STM [119]. The mechanical precision needed to fully utilise the tunnelling principle is obtained with piezo-elements, the size of which can be controlled with sub-Å precision, provided the input voltages are precise enough.

The STM is usually operated in "constant current" mode, where  $I_t$  is kept constant for a given bias voltage, and the height of the tip above the surface is adjusted to facilitate this. The movement of the tip perpendicular to the sample ( $z$ ) as a function of position on the sample ( $x, y$ ) then results in an STM image, depicting the topography of the surface with a constant LDOS. It is also possible to run the STM in "constant height" mode, where  $z$  is kept constant for a given bias voltage and the tunnelling current is recorded as a function of position. This mode is faster, as it does not rely on a feedback loop to change the height of the tip, however there is a significant risk of destroying the tip by crashing it into the sample. For this reason the mode is rarely used. The operating principle of STM is illustrated in Fig. 2.6

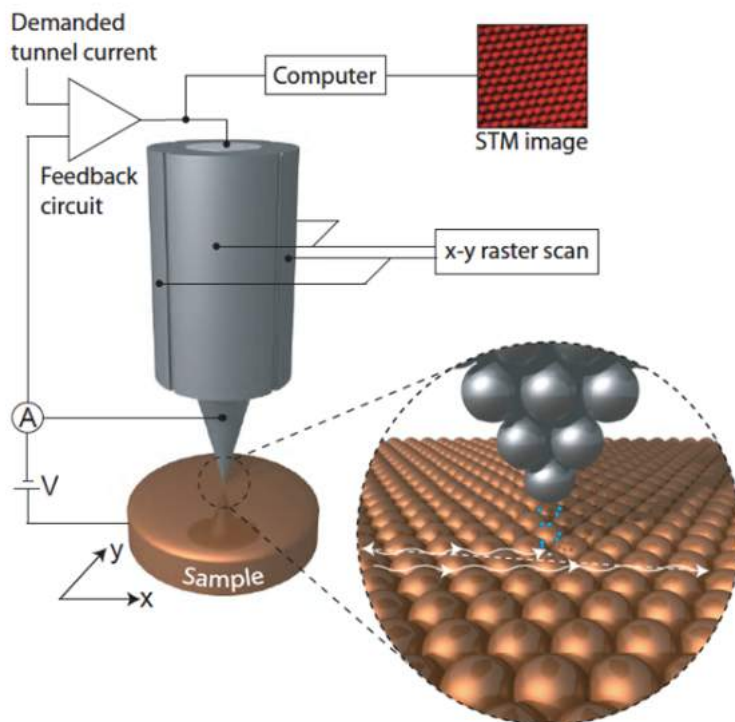


**Figure 2.6:** Illustration of the working principle of STM. An atomically sharp tip is moved across a conductive surface at a short distance. A bias voltage is applied between the tip and the surface, facilitating the tunnelling of electrons from the surface to the tip, or vice versa, and inducing a tunnelling current. This makes it possible to create a topological image of the surface. Figure courtesy of Jakob Kibsgaard.

## 2.5 Minor Techniques

Aside from TPD and STM, LEED and AES were used in the hydrogen flux measurement experiments. They will be discussed very briefly.

### 2.5.1 Low Energy Electron Diffraction - LEED

LEED, is a very surface sensitive technique with two main applications. The first is to gain information about the surface order and quality through inspection of the electron diffraction pattern. The second is to obtain quantitative information about the structure of the sample. The latter is quite

difficult, and, since we only utilise LEED to check the reconstruction of our silicon (Si) sample in our hydrogen flux measurements (chapter 3), irrelevant for the purpose of this project. Therefore it shall not be discussed further. The LEED apparatus consists of an electron gun and a detector component. The electron gun emits a beam of low energy electrons along the surface normal. The low energy of the electrons make the technique very surface sensitive as a) their low energy ensures that they will not penetrate far into the bulk of the sample and b) their de Broglie wavelength is of the same order as the distance between atoms in a crystal structure, ensuring that diffraction phenomena are present. The detector component consists of four metal grids at different voltages and a fluorescent screen. The first and fourth grids from the sample are kept at ground potential, while the two middle grids are kept at a retarding potential slightly lower than the energy of the incoming electrons. This is done in order to deflect inelastically scattered electrons, making sure that only elastically scattered electrons make it to the fluorescent screen. The screen is set at a high voltage, and when an electron hits it, it causes fluorescence, causing it to light up. The dots on the fluorescent screen are thus a direct representation of the diffraction pattern, which corresponds to the reciprocal lattice of the surface, and the surface structure can be derived directly from it.

The surface sensitivity of the technique comes from the universal curve, which describes the inelastic mean free path (IMFP) of an electron into a crystal as a function of it's kinetic energy. For most elements the curve has a minimum around 5 Å at a kinetic energy of the electrons of approximately 50 eV.

### 2.5.2 Auger Electron Spectroscopy - AES

AES utilises the characteristic binding energy of core electrons to gain information about the different elements present on a surface. If an atom has a core electron hole (level A) the hole can be filled by an electron from a higher lying level (level B), and the excess energy can knock out an Auger electron from level C. The process is illustrated in Fig. 2.7. The kinetic energy of the Auger electron from level C is described by the equation [120]

$$E_{kin} = E_A - \frac{1}{2}(E_B^Z + E_B^{Z+1}) - \frac{1}{2}(E_C^Z + E_C^{Z+1}) - \phi,$$

where  $\phi$  is the work function and the energies of levels B and C are averaged over the energies of the original atom and those of an atom with increased

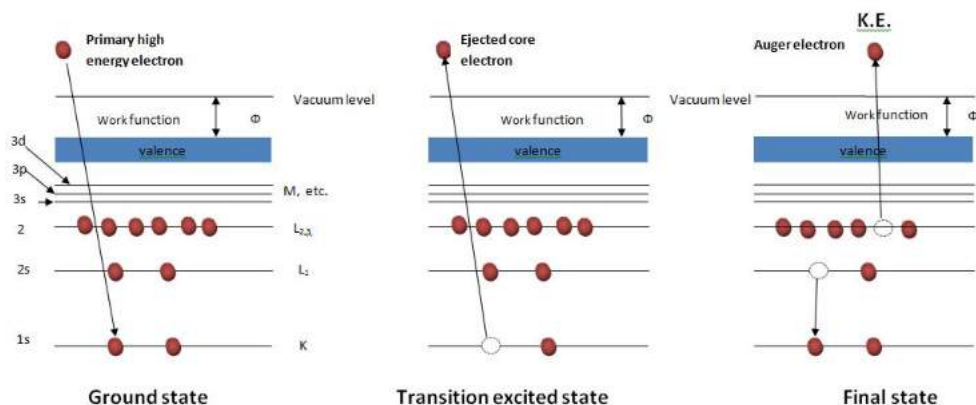


**Figure 2.7:** Illustration of the Auger process. A core electron is knocked out of the atom by a high energy electron. The hole is filled by an electron from a higher lying level, and the excess energy knocks out another high level electron. The resulting kinetic energy of the Auger electron is element specific. From [127]

charge, to account for the core electron hole. The core holes are usually generated by a beam of high-energy electrons. The kinetic energy of the Auger electrons depend only on the atomic energy levels and the work functions, making AES a very element sensitive technique

AES is not, however, a good technique for detecting very small elemental contributions, as it is not possible to detect contaminations of less than 1-2%. However, it is a simple method, and perfectly good for our purpose: Ensuring that the Si surface used in the hydrogen flux measurements (chapter 3) is clean enough for hydrogenation.

### 2.5.3 Density Functional Theory - DFT

Density functional theory is a computational quantum mechanical method used to solve the n-body Schrödinger equation, and is one of the most commonly used computational procedures in molecular electronic structure calculations [36]. The basic idea is to describe the energy of the n-electron system in terms of the electron probability density  $\rho(\mathbf{r})$ , at a particular point. The electronic energy of the system can be treated as a functional of the electron density  $E[\rho]$ , *i.e.* for a given function  $\rho(\mathbf{r})$  there corresponds a single energy.

There are several advantages to using DFT to calculate the electronic structure of molecules. Chief among them is that it uses a single 3D function  $\rho$  for an  $n$ -electron molecule. This is in contrast to a wave function approach, which relies on the properties of a  $3n$ -dimensional function, on which a large number of constraints are imposed to ensure that it is fully anti-symmetric. However, DFT does rely on a number of assumptions, mainly that the electron density determines the properties of the molecule or surface and that the energy is correctly given by a variational principle.

The first assumption is based on the Hohenberg-Kohn theorem [128], which states that "the ground state energy, and any other ground state electronic properties, are uniquely determined by the electron density". This confirms that it is possible to express the ground state energy as a functional of the ground state electron density

$$E[\rho] = T[\rho] + V_{ee}[\rho] + \int (\rho(r)V(r))dr.$$

Here  $T$  is the kinetic energy functional and  $V_{ee}$  the electron-electron potential energy functional, which in turn is the sum of a classical Coulombic contribution and a quantum mechanical contribution. Now it is sufficient to know the ground state electron density in order to determine the properties of the molecule. However, determining the electron density means solving the Schrödinger equation and finding the electron wave functions which is not possible.

In order to simplify the procedure of finding the ground state electron density, the Kohn-Sham equations are used [129]. Here a system of  $n_e$  non-interacting electrons in an external potential,  $V_{ref}$  is used. The system is chosen such that the electron density of the reference system  $\rho_{ref}(r)$  is identical to the true electron density  $\rho(r)$ . Then the energy of the system can be expressed as

$$E[\rho] = T_{ref}[\rho] + J_{ref}[\rho] + \int (\rho(r)V(r))dr + E_{XC}[\rho],$$

with  $J[\rho]$  being the Coulombic potential and  $E_{XC}$  being the exchange correlation term

$$E_{XC}[\rho] = T[\rho] + V_{ee}[\rho] - (T_{ref}[\rho] + J[\rho]).$$

What remains is to find a suitable functional for the exchange correlation. Several approximations exist for this purpose. The simplest one is the

local density approximation (LDA) [130], where the exchange correlation is assumed to be dependent on the local electron density. An improvement on the LDA functional is the general gradient approximation (GGA), which also accounts for the gradient in electron density. The most commonly used GGA functional is the Becke 3-parameter Lee-Yang-Par (B3LYP) functional [131].

# Chapter 3

## The Hydrogen Doser Flux

*She says nothing at all, but simply stares  
upward into the dark sky and watches, with sad  
eyes, the slow dance of the infinite stars.*

— Neil Gaiman, *Stardust*

In order to properly analyse the TPD data, it is necessary to know the flux of atoms at the sample. When there is no nozzle attached this flux can be calculated, based on the diffuseness of the beam exiting the cracker, its temperature, and the pressure of gas through the cracker [117, 132]. This makes it possible to obtain an atomic flux at the sample as a function of distance to the cracker. However, when a cooling nozzle is attached to the cracker it is very difficult to accurately estimate the loss due to recombination in the nozzle, and how dispersed the beam is at the end of the nozzle, and so a simple calculation is not possible. For this reason an experiment to measure it was performed.

### 3.1 Measuring the Hydrogen Flux

The measurements of the flux of the hydrogen beam exiting the nozzle is measured through hydrogenation of the Si(100) $2\times 1$  surface. This system and its interaction with hydrogen is well known, and has been studied several times [133, 134, 135, 136, 137, 138, 139, 140, 141, 142, 143], and thus can be used for calibration.

### 3.1.1 The Si(100) Surface

The interaction between the Si(100) surface and atomic hydrogen is a well known system. When the surface is  $2\times 1$  reconstructed, for a hydrogen coverage below 1 ML (one hydrogen bound to each Si atom), hydrogenation is expected to happen very quickly, with coverage rising almost linearly. When a coverage of 1 ML is reached it levels off and increases very slowly toward a saturation coverage just below 2 ML. A schematic of how hydrogen binds to the Si(100) surface for different surface reconstructions is shown in Fig. 3.1 [143]. For the  $2\times 1$  reconstruction the Si atoms form dimers, leaving one dangling bond per atom, resulting in a Si atom being able to bind exactly one hydrogen (monohydride phase), whereas for the  $1\times 1$  reconstruction, the surface has two dangling bonds per Si atom, which can bind two hydrogen atoms (dihydride phase). In the  $3\times 1$  reconstruction every third Si atom is a dangling bond, and can bind two hydrogen atoms, whereas the rest can bind only one [138, 139].

In theory, when the sample and beam are at room temperature the hydrogen atoms first bind to the available dangling bonds of the Si-dimers creating a monohydride Si(100) $2\times 1$ -H phase. Then impinging atoms break the bonds between the Si-dimers, leading eventually to the creation of a dihydride Si(100) $1\times 1$ -H phase. In reality however, the two processes overlap, and the dihydride phase will start to grow before the monohydride phase is saturated. This makes it impossible to accurately count the number of adsorption sites on the surface [138, 139].

However, it is possible in the  $2\times 1$  Si(100) reconstruction to preserve a saturation coverage of 1 ML [144], ensuring that the system is well defined and can be used as a calibration system. At temperatures higher than 625 K, the dihydride phase becomes unstable, ensuring that only monohydride states can be hydrogenated. Thus, as long as the sample is kept above this temperature during the atomic dose, no dihydride states should exist [133, 140, 141].

### 3.1.2 H/Si(100) TPDs and Flux Measurement

Prior to performing the calibration measurements the sample must be cleaned. This is done through sputtering of the surface with  $\text{Ar}^+$ -ions (for 30 minutes at the beginning of each day and 5-10 minutes between every measurement), followed by annealing to 1000 K for 5 minutes. The sample reconstruction is then checked with LEED and the cleanliness with AES. Examples of these

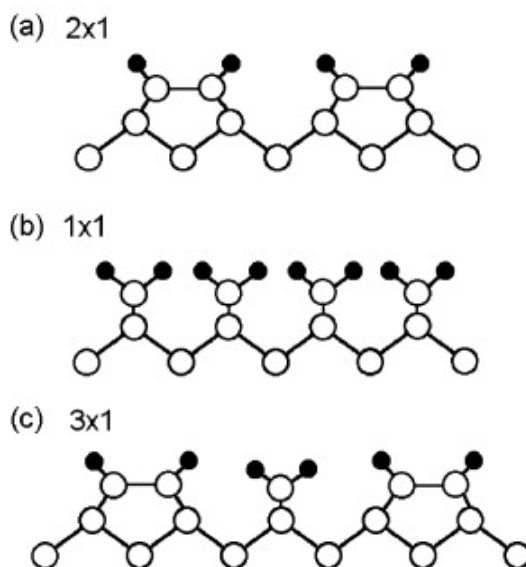
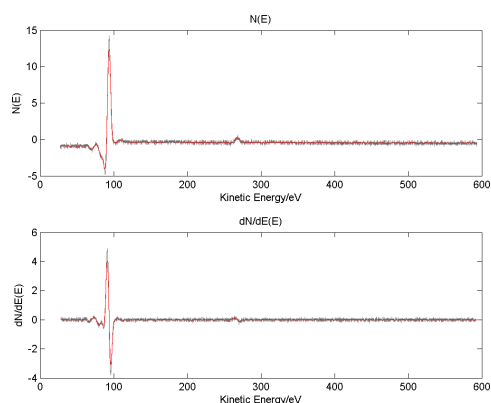


**Figure 3.1:** Different reconstructions of the Si(100) surface and how they bind to hydrogen. Adapted from [143]



(a) LEED pattern of Si(100) 2x1 reconstruction



(b) Auger spectrum of clean Si(100)

**Figure 3.2:** a) LEED pattern of a  $2 \times 1$  reconstructed Si(100) surface. A square pattern of bright spots, with a secondary offset square pattern of fainter dots. b) An AES spectrum of Si(100). The large peak at 96 eV is a Si peak, while the smaller peak just below 300 eV arises due to a small carbon contamination.

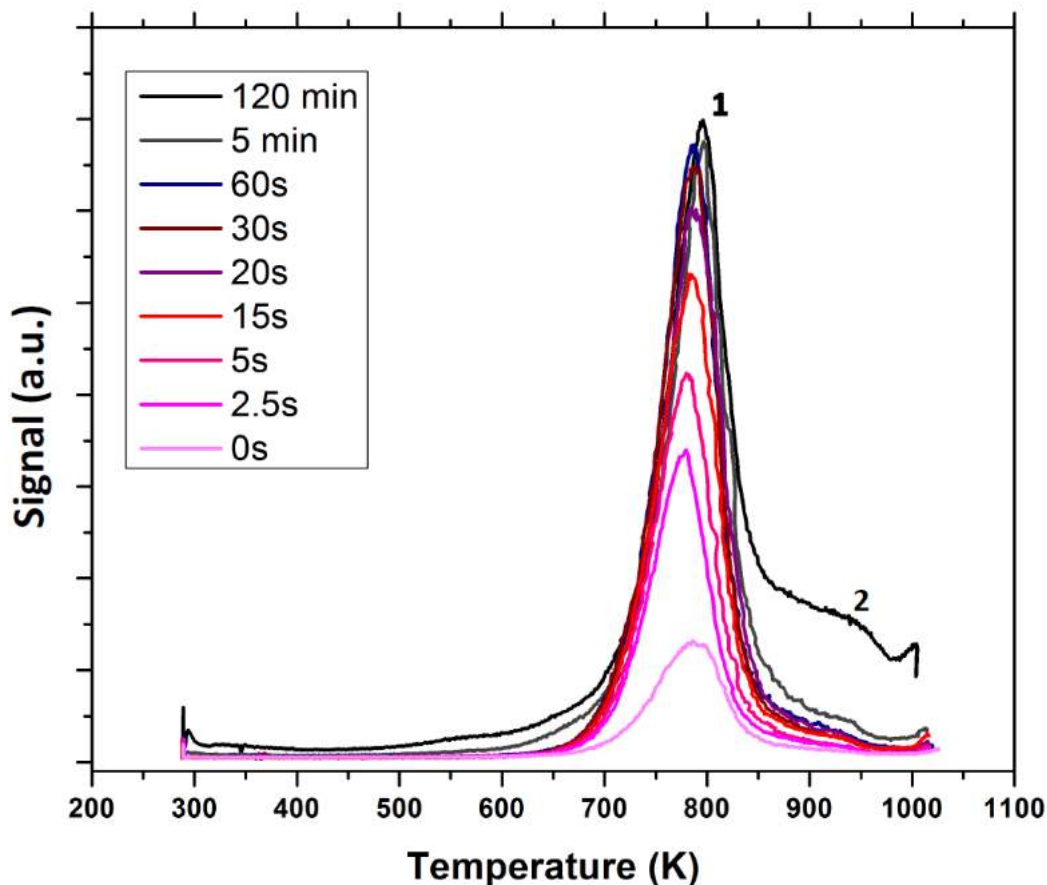


**Figure 3.3:** Collection of TPD curves of  $D_2$  from  $Si(100)2\times 1$ . The peak labelled 1 is the monohydride peak, while the peak labelled 2 is the peak arising due to absorption into the bulk.

for a clean  $Si(100)2\times 1$  surface are shown in Fig. 3.2. Once the sample is ready it is heated to 700 K and exposed to an atomic hydrogen or deuterium beam for a set amount of time. After exposure a TPD measurement is performed.

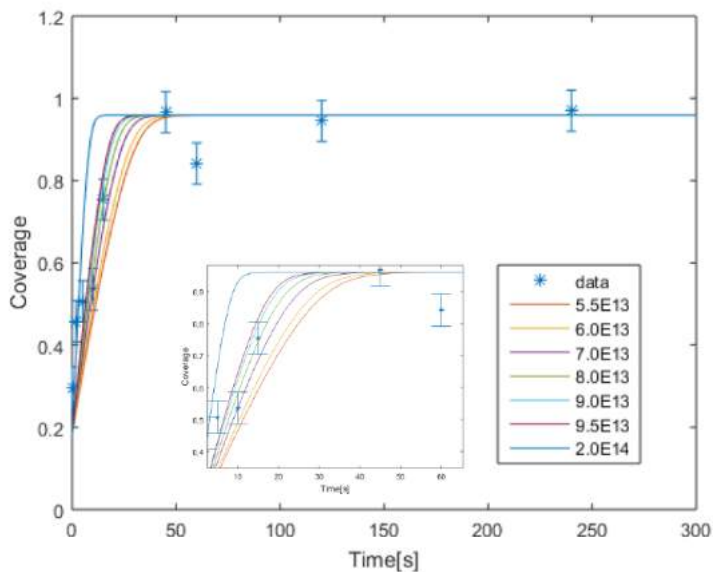
The resulting TPD curves have a two peak structure. A collection of TPD curves of  $D/Si(100)$  is shown in Fig. 3.3, and a clear tendency towards a two peak structure is evident, especially for longer dose times. The first peak (labelled "1" in the figure) is the monohydride peak, and the one interesting for our analysis. The second peak ("2" in the figure) grows rapidly with increasing dose time, and is attributed to hydrogen in the bulk of the sample.

In some cases, if the reconstruction is not perfect, a shoulder may appear on the low temperature side of the main peak, which can be attributed to a small contamination from the dihydride phase. The main peak is fitted with an asymmetric function and the bulk peak with a gaussian function, the parameters of which are manually tweaked to ensure the best overall fit. The main peak is then integrated to find the relative coverage of the the sample.

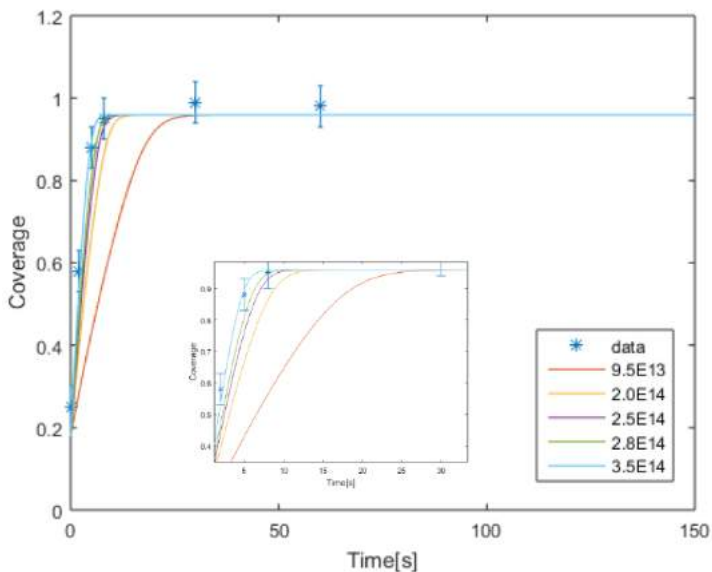
Knowing the relative coverage of the surface, the flux of atoms can be found by fitting to the following equation [145]

$$\frac{d\theta}{dt} = \frac{\theta dt}{N_0} \left( \frac{P_{ad}^0}{1 + \frac{L\theta}{(1-\theta)}} - \frac{P_{ab}^0}{1 - \frac{E(1-\theta)}{\theta}} \right).$$

The flux is varied until the best fit to the data is found. Fig. 3.4 shows the data for deuterium (a) and hydrogen (b) with a number of fits. For deuterium the best is found for a flux of  $7.75 \pm 1.25 \times 10^{13} \text{ cm}^2\text{s}^{-1}$  while for hydrogen it is significantly higher at  $2.8 \pm 0.7 \times 10^{14} \text{ cm}^2\text{s}^{-1}$ . This difference is probably explained by the experiments being run with the guage on the gas line showing the same reading. The guage is calibrated for deuterium, and as a result it is possible that a significantly larger amount of hydrogen is needed for the guage to read the same pressure.



(a) Deuterium flux calculation



(b) Hydrogen flux calculation

**Figure 3.4:** Coverage of H/D on Si(100) as a function of dose time, with several fluxes fitted. (a) shows the data for deuterium, where a flux of  $7.75 \pm 1.25 \times 10^{13} \text{ cm}^2\text{s}^{-1}$  is found to yield the best fit. (b) shows the data for hydrogen, where the best fit gives a flux of  $2.8 \pm 0.7 \times 10^{14} \text{ cm}^2\text{s}^{-1}$ . A zoom of the regions where the coverage saturates is inserted in both figures for clarity.

# Chapter 4

## Experimental Results - PAHs

*It is sometimes an appropriate response to reality to go insane.*

— Philip K. Dick, *Valis*

In this chapter I will describe and discuss the results from TPD experiments with deuteration and hydrogenation of the PAH molecule coronene. These experiments were done in close collaboration with former PhD student Anders W. Skov and current PhD student Frederik D. S. Simonsen, and the analysis was done by me.

### 4.1 Deuteration of coronene

The experiments which were carried out as part of this thesis were done with a cooling nozzle attached to the HABS in order to reach a more realistic gas temperature with respect to the interstellar environments where these experiments are of interest. As mentioned in chapter 2 the cooling nozzle results in a kinetic gas temperature of approximately 1000 K.

Superhydrogenation reactions have been studied using the heavy hydrogen isotope deuterium. Deuterium is used because its higher mass makes it possible to detect abstraction reactions involving the hydrogen atoms on the edge of the coronene molecule. Furthermore, it is easier to detect with a mass spectrometer than regular hydrogen because there is not a high background of  $D_2$  present in the vacuum system. The results of experiments with superdeuteration of coronene are described in this section.

Before analysis the data is plotted after baseline subtraction. The baseline is found based on the signal at mass 364. This is higher than the mass of fully superdeuterated coronene ( $C_{24}D_{36}$ ), and so any signal at this mass can be attributed to noise, and thus baselined away. This baselining routine assumes a constant level of noise across the data. After smoothing and baselining, the data is presented in contour plots. Fig. 4.1(a-e) shows the contour plots of the TPDs of deuterated coronene for different atomic dose times. The temperature at which the molecules desorb from the graphite surface is plotted on the x-axis, while the mass of the molecule is plotted on the y-axis. The intensity of the contours show the signal at a particular mass and temperature coordinate. From these plots it can be seen that for higher dose times, higher masses (corresponding to the addition of more deuterium atoms) can be reached, and that the high-mass molecules desorb from the HOPG surface at lower temperatures than the pristine coronene, suggesting that the superdeuterated molecules are more weakly bound to the surface (see also section 4.4).

Although for the most part, high-mass molecules desorb at low temperatures, and even pristine coronene desorbs at approximately 460 K, high temperature tail is present. For pristine coronene the high temperature desorption can be attributed to the sample holder. However, this does not explain the high temperature signal for the highly superdeuterated species, where a tail is clearly present for masses 340 to 360. It is possible that the high temperature tail for the highly superdeuterated species can be explained by a tendency towards clustering of the molecules, resulting in having to break not only the bond to the graphite, but also to other molecules in order to desorb, resulting in a higher desorption energy, and thus a higher temperature. This hypothesis still remains to be tested.

From the contour plot a TPD spectrum can be obtained at every mass. A sample of these are shown in Fig. 4.2, for masses 300, 304, 306, 248, 354, and 360 amu. The tendency of lower desorption temperature for higher masses is clearly evident in the figure. The black curve traces the desorption of a monolayer of pristine coronene. This has a much higher intensity than desorption peaks of the higher masses, mainly because the masses are spread out over a wider distribution.

The yield of each mass for a given atomic dose is found by integrating the TPD spectrum at each mass. The integration is stopped at 600 K, to avoid any contribution to the mass distribution attributable to dosing on the sample holder.

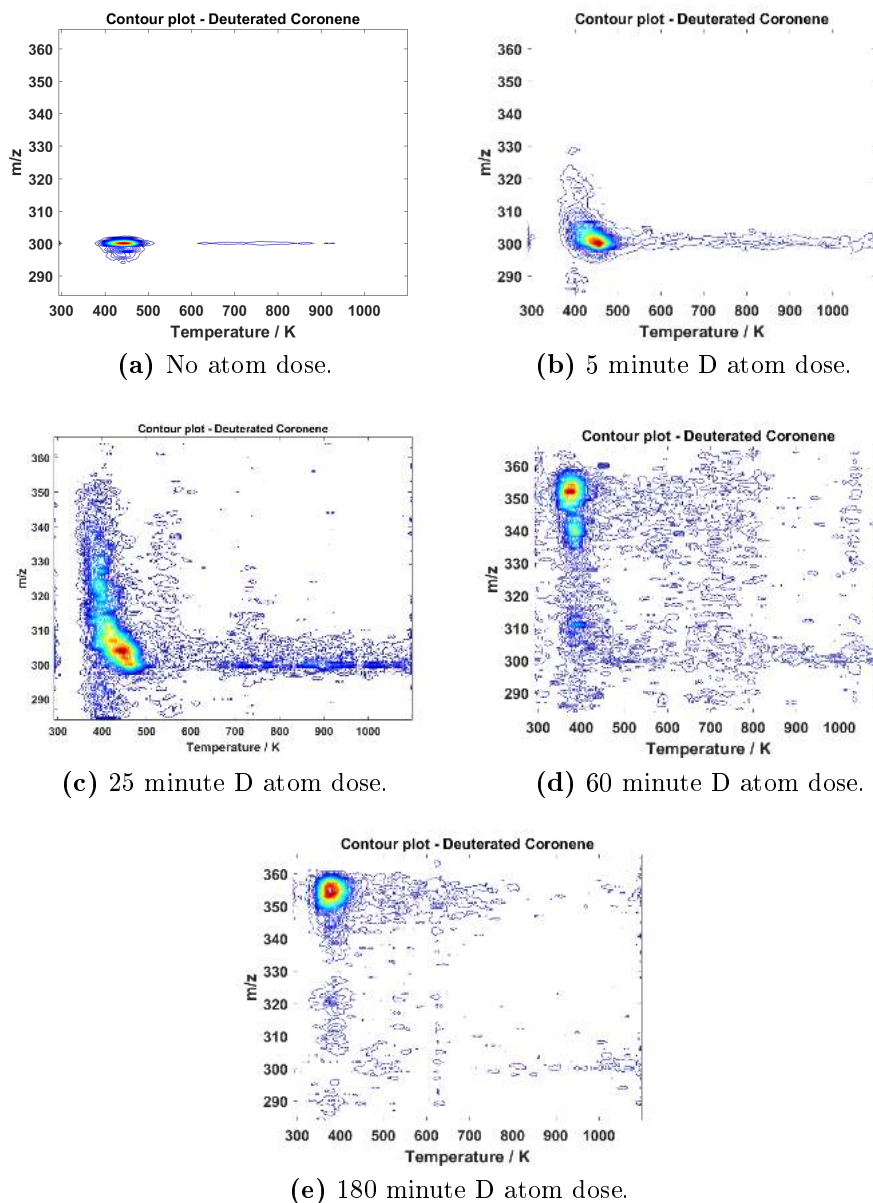


**Figure 4.1:** contour plots after baselining of deuterated coronene for different atom dose times ranging from no atomic dose (a) to a 180 minute atom dose (e).

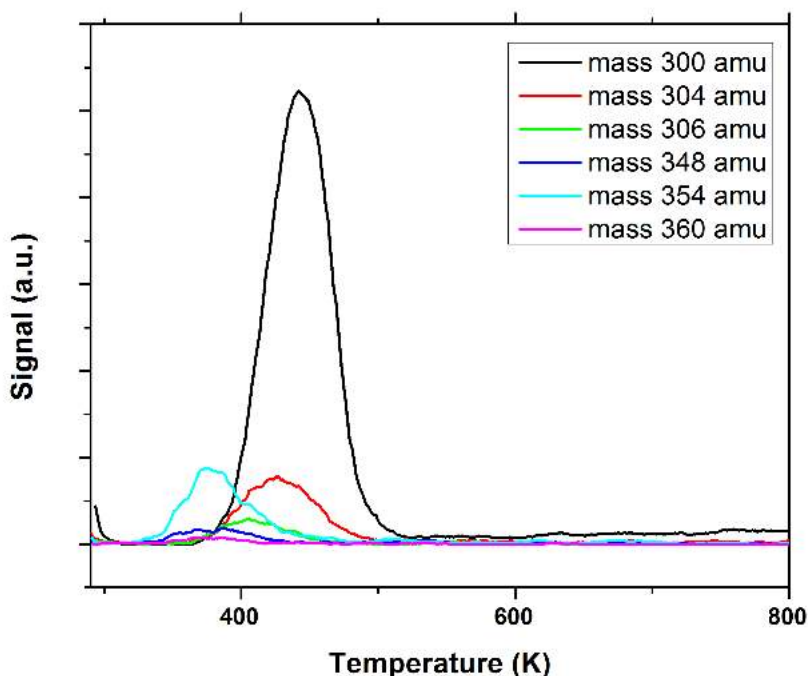


**Figure 4.2:** TPD spectrum of a monolayer of pristine coronene (black curve) and a sample of higher mass TPD spectra from low to high degree of superdeuteration.

In Fig. 4.3 the mass distributions of superdeuterated coronene are shown for different atomic dose times, from no atom dose to 180 minutes atom dose. The masses range from 300 to 360 amu, 300 amu being the mass of pristine coronene, and 360 amu being the mass of fully superdeuterated coronene. The figure is color coded. The red masses can be reached by deuterating the outer and inner edge sites on the coronene molecules. The green masses can be reached by either deuterating the centre sites or abstracting the edge hydrogen atoms, replacing them with deuterium, while the blue masses can only be reached if both those processes take place. Masses lower than 300 amu occur due to fractionation in the mass spectrometer.

An interesting thing to note about the mass distribution, once masses higher than around 336 amu are reached, is that there is a tendency towards a two-peak structure. The peaks move slightly, but are always 12 amu apart,

corresponding to six deuterium atoms. A two peak structure was never seen before, with the hot deuterium atoms. A possible explanation for this might be the existence of a barrier to the first centre site addition. The peaks move because different numbers of edge hydrogen atoms may have been switched out with deuterium, but remain 12 amu apart because once the first addition to a centre site takes place, the rest of the molecule is easily deuterated. At this point this is still a hypothesis, which further study and analysis is needed to confirm.

The evolution of the relative yield of certain key masses with D atom dose time is shown in Fig. 4.4. A clear increase is seen for masses higher than 300 amu, even at low dose times. For intermediate masses, e.g. 312 and 342 amu, a saturation level is reached, after which their yield starts to decline again, as higher deuteration levels are reached. The yield of higher masses, 354 and 360 amu continue to grow. If dosing were to be extended eventually these masses would also reach a maximum, which in the case of 360 would not subsequently decline, as 360 amu corresponds to fully superdeuterated coronene.

### 4.1.1 Low Temperature Deuteration

A longer cooling nozzle was made to cool the atomic beam down to roughly 500 K. Unfortunately this nozzle broke before a full data set could be completed. Preliminary results exist though, showing that it is possible to fully superdeuterate coronene with a low temperature atomic beam, as shown in Fig. 4.5. Mass distributions are shown for three different dose times: no atomic dose, 45 minutes and 720 minutes. The nozzle broke before a flux calibration could be made, so it is not possible to say anything about the fluence needed to superdeuterate coronene with this nozzle, *i.e.* if it is more difficult to add deuterium at low temperatures or if the flux of atoms at the sample is simply lower than for the higher temperature atomic beam. However the data clearly shows that superdeuteration is possible, and that the double peak structure seen for the 1000 K data at high degrees of deuteration is also seen at lower temperatures.

## 4.2 Hydrogenation of coronene

In order to further investigate the addition barriers the experiments were repeated with hydrogen instead of deuterium. If the same peak structure is

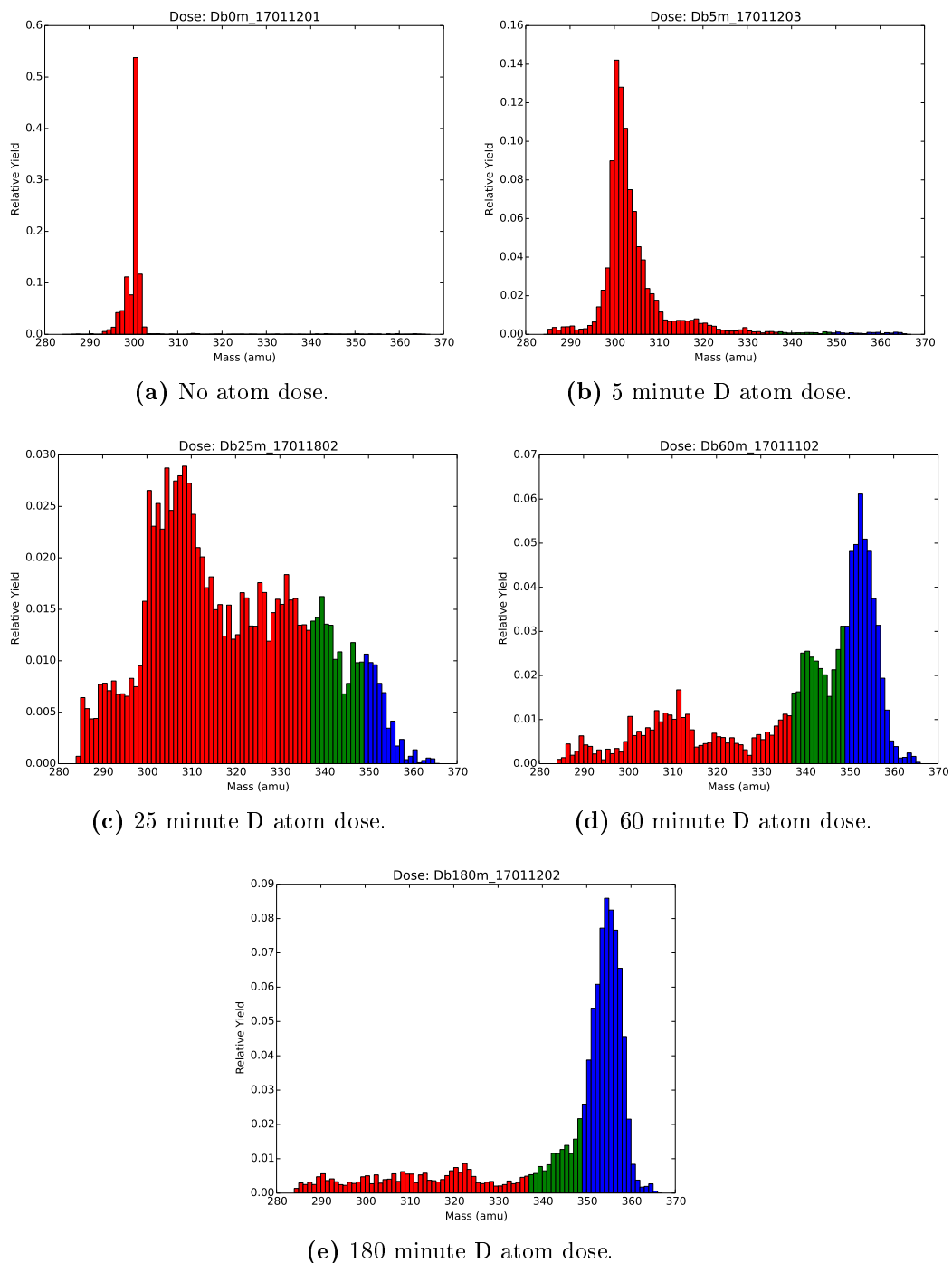


**Figure 4.3:** Mass distribution of deuterated coronene for different atom dose times, ranging from no dose to an atom dose time of 180 minutes.

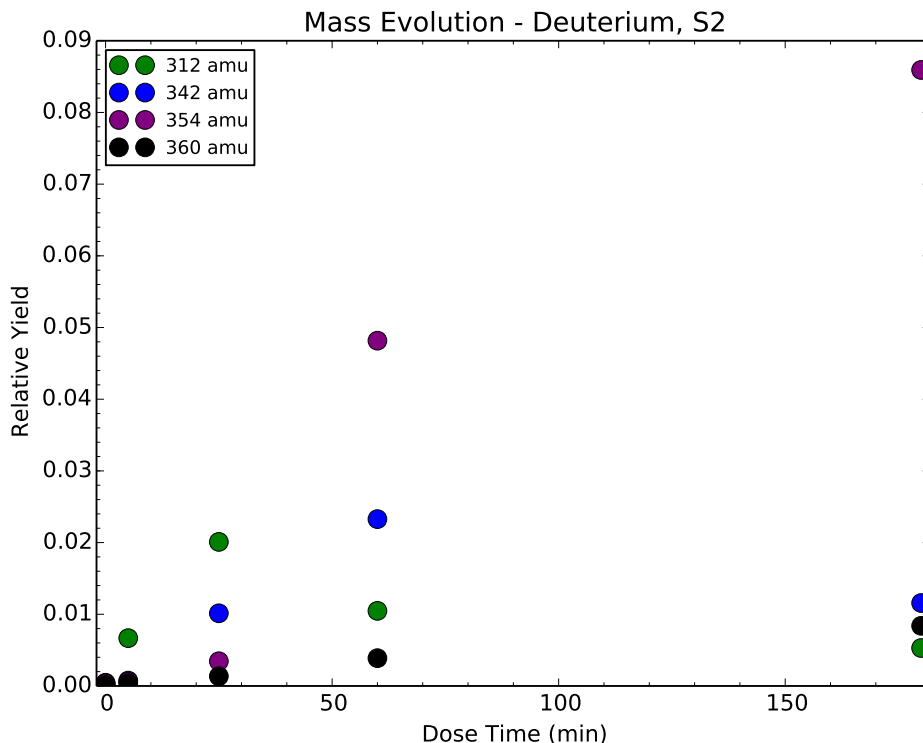
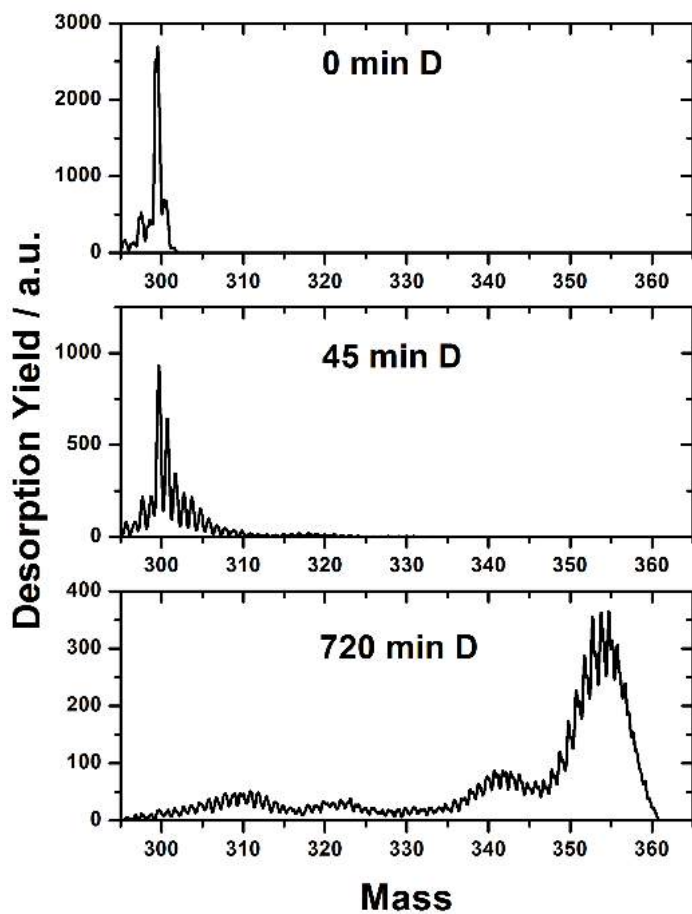


**Figure 4.4:** Evolution of key masses with deuterium dose time.

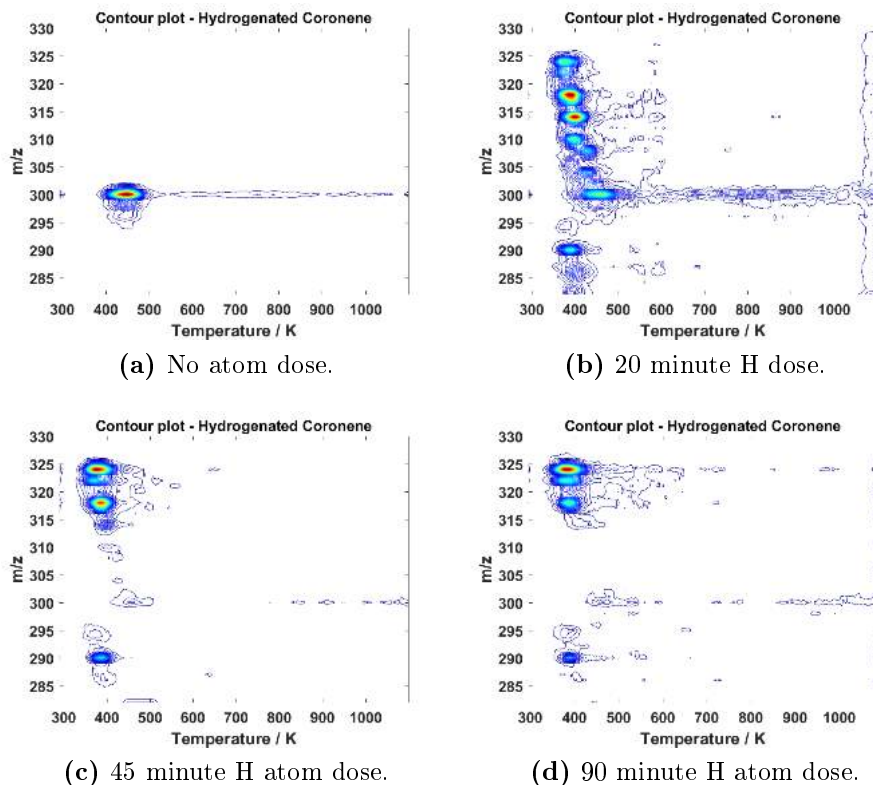
seen, it will likely be due to a barrier for center site addition, as abstraction reactions cannot be directly observed. This will result in peaks at distinct masses, rather than the broader, moving peaks of the deuterium experiments.

Fig. 4.6 shows the contour plots of superhydrogenated coronene for different atom dose times. Just as with deuterium, the plots show at which temperatures the molecules with different numbers of additional hydrogen atoms leave the graphite surface, and generally, the higher the mass of the molecule, the lower the desorption temperature. The data also exhibits the same tendency of a high temperature tail for the high-mass desorption products.

One notable difference from this trend is the molecule with mass 290 amu. Molecules with this mass leave the surface at the same temperature as molecules with mass 318 amu, suggesting the 290 amu may be a fragment of  $C_{24}H_{30}$ . The mass difference corresponds to the loss of  $C_2H_4$ , and since



**Figure 4.5:** Mass distribution of superdeuterated coronene for three different low temperature fluences.



**Figure 4.6:** Contour plots of coronene exposed to hydrogen, for atom dose times ranging from no dose (a) to a 90 minute dose (d). The data is plotted after smoothing and baselining routines have been applied.

the molecules leave the surface at the same temperature, fragmentation is believed to happen in the QMS during the ionisation process, rather than on the surface.

As with deuterium addition, a TPD spectrum can be constructed at every mass, from the data shown in the contour plot. The TPD spectra of the main stable mass configurations are shown in Fig. 4.7. As above, there is a clear tendency for higher mass products to desorb at lower temperatures, and the signals of the higher mass products are smaller than that of the monolayer.

Just as for the deuterated coronene data, the peaks at every mass are integrated to get the mass distribution for a given dose time. Again the integration is stopped at 600 K to avoid a contribution attributable to the

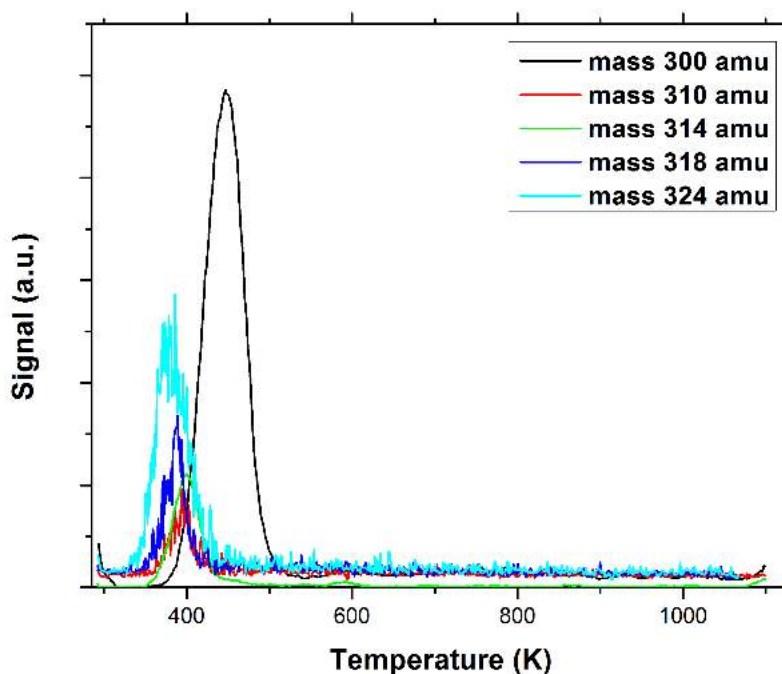


**Figure 4.7:** TPD spectra of the coronene monolayer and four masses corresponding to stable higher degrees of superhydrogenation.

sample holder.

The mass distributions for eight different fluences are shown in Fig. 4.8, going from no atom dose in the top trace to a 90 minute atom dose in the bottom trace. Vertical black lines mark the masses where peaks appear, specifically 300, 310, 314, 318, 322, and 324 amu. A peak also appears at 290 amu, a lower mass than that attributed to pristine coronene. Some of these masses seem to appear together: 290 amu only appears with 318, and the same seems to be true for 322 and 324. In Fig. 4.9 the sizes of specific peaks are traced as a function of dose time and we can follow the evolution of the peaks together. The figure tells the same story as above, some of the peaks (290 and 318, and 322 and 324) appear together. A likely explanation for this is that the higher mass molecules (318 and 324) fracture in the mass spectrometer, and have a favoured fractionation route - the loss of  $C_2H_4$  and the loss of  $H_2$  respectively. This observation is supported by

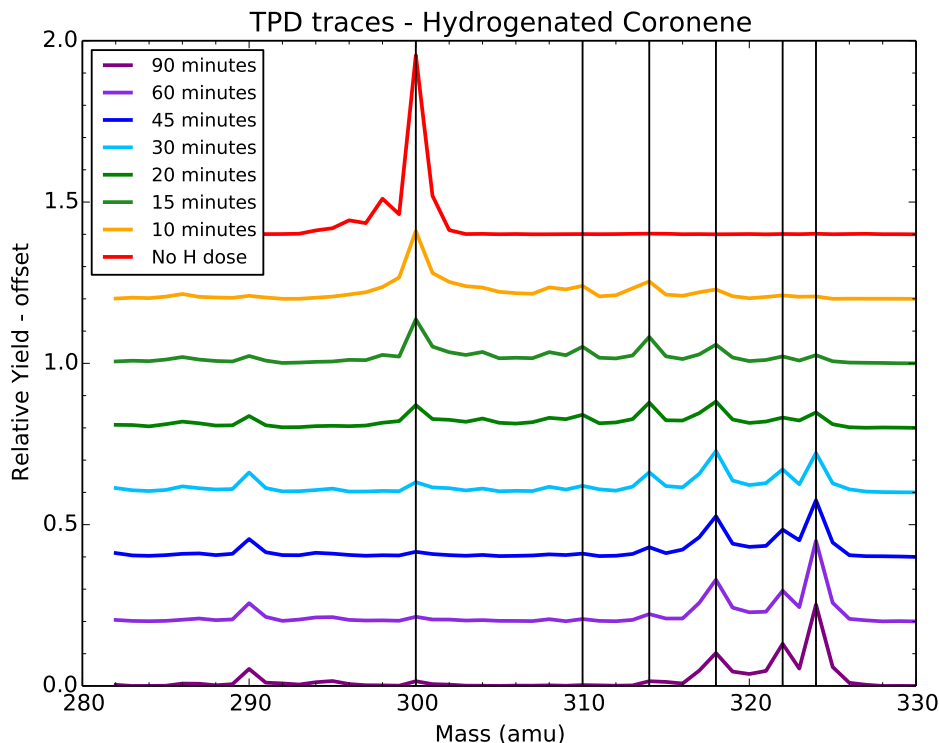


**Figure 4.8:** Mass distribution of superhydrogenated coronene for different atomic dose times.

the contour plots in Fig. 4.6, where we can see that mass 290 desorbs at the same temperature as mass 318, and the same is true for masses 322 and 324.

### 4.2.1 Stable Configurations

The appearance of peaks at distinct masses in the mass distribution of superhydrogenated coronene suggests that certain stable configurations can be reached. The first stable peak after pristine coronene appears at 310 amu, suggesting that the first 10 atoms are added very quickly. Rauls and Hornekær [74], studied the addition of the first eight atoms to coronene using DFT, and found that, once the barrier for the first addition had been overcome, subsequent additions happened fast and at low to vanishing barriers. Keeping this in mind, the experimental results are not unexpected.

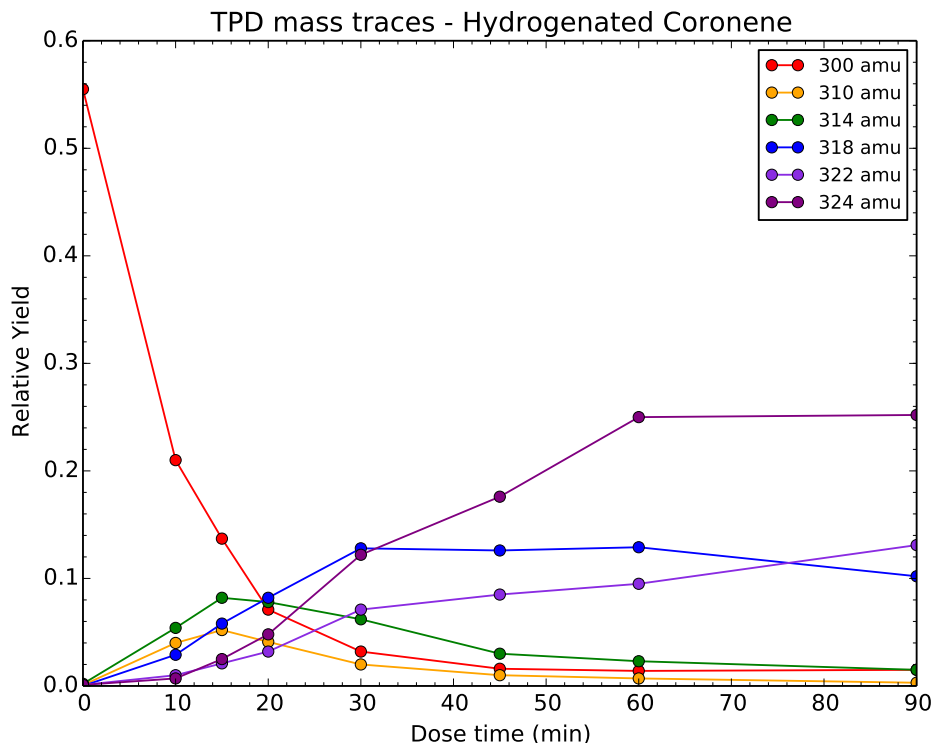


**Figure 4.9:** Evolution of the relative yield specific masses with dose time.

Subsequent peaks are seen at 314 and 318 amu, likely corresponding to stable configurations of superhydrogenated coronene.

The peak at 322 amu is likely a fragment of the fully superhydrogenated molecule, with mass 324 amu. This hypothesis is based on the fact that the two masses desorb at the same temperature and the two masses follow the same evolutionary trend in Fig. 4.9.

If it is indeed the case that the peak at 322 amu is merely a fragment of a molecule with mass 324 amu, the last real peaks in the mass distribution are 318 and 324 amu. These peaks are separated by 6 amu, and could therefore likely be the result of a barrier for centre site addition. This would suggest a different hydrogenation route than that found by Rauls and Hornekær [74].

The stable configurations and their hydrogenation routes are being studied with DFT calculations Rocco Martinazzo from Milan, but at the time of writing these are not yet complete.

### 4.3 Addition Cross Sections

In order to investigate the efficiency of PAHs as catalysts of H<sub>2</sub> formation in the ISM, it is necessary to find the addition and abstraction cross sections of hydrogen. The addition cross section for the first hydrogen atom  $\sigma_{add}(0)$  can be found experimentally. This is done by plotting the relative yield of pristine coronene as a function of H atom fluence, and fitting the following exponential decay:

$$I_{300} = I_0 \exp(-\Phi_D \sigma_{add}(0)) + I_{inf}.$$

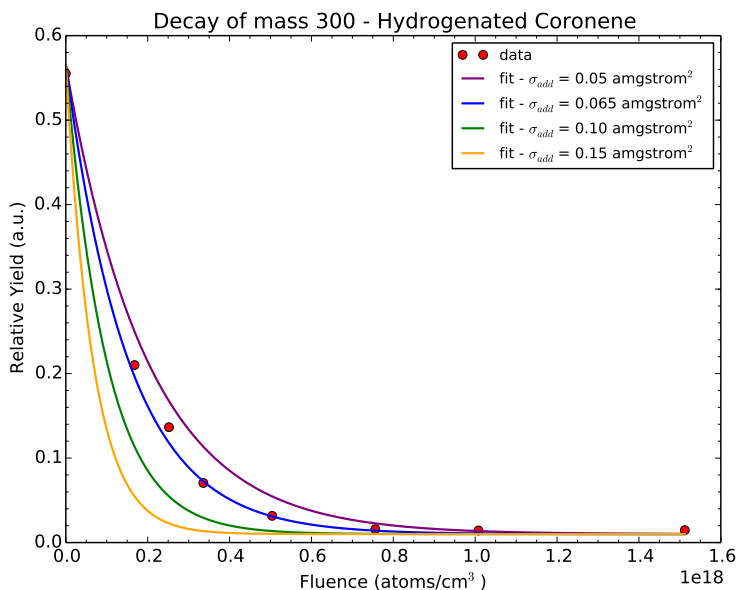
Here  $I_{300}$  is the relative yield of pristine coronene,  $I_0$  is the initial relative yield of pristine coronene, without dosing hydrogen, and  $I_{inf}$  is the relative yield of pristine coronene at an infinite H atom dose.  $\Phi_D$  is the H atom fluence. All quantities, except for the addition cross section are known, and  $\sigma_{add}$  can be varied until the best fit to the data is achieved.

The fits for both deuteration and hydrogenation are shown in Fig. 4.10 (a) and (b) respectively. For deuterium a cross section of  $\sigma_{add}(0) = 0.25 \pm_{0.05}^{0.14} \text{ \AA}^2$  is found, whereas for hydrogen a significantly lower addition cross section of  $\sigma_{add}(0) = 0.065 \pm_{0.05}^{0.1} \text{ \AA}^2$  is found. If this lower cross section is a true result, it could suggest that a high temperature route to deuterium enrichment of PAHs exist. However, this will need further investigation to confirm, and it is worth noting that the exponential function does not fit the deuterium data very well at higher fluences.

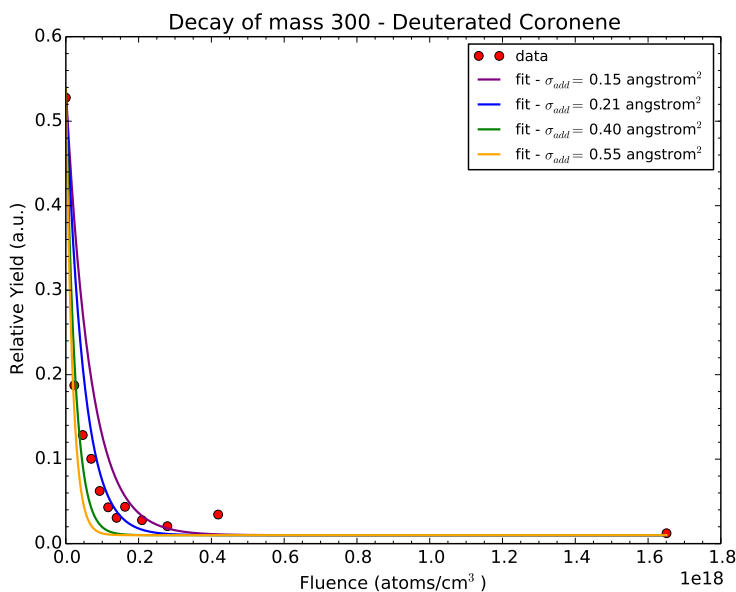
It is not possible to calculate the subsequent addition and abstraction cross sections directly from the experimental data. Simple kinetic simulations have been used previously [82], with hot deuterium. However, the peak structure of the data for colder atoms necessitates the use of site specific kinetic Monte Carlo simulations, which are underway in collaboration with Dr. Herma Cuppen in Nijmegen.

### 4.4 Binding Energies to HOPG

The binding energies of superdeuterated coronene to the HOPG surface has been studied experimentally and by DFT previously [83], and the results of that study were discussed briefly in chapter 1 of this thesis. In that study the coronene on HOPG was deuterated using a beam of atoms at a kinetic temperature of 2300 K. The mass distribution of the superdeuterated coronene in this case, shows no sign of peak structure [80], in the way

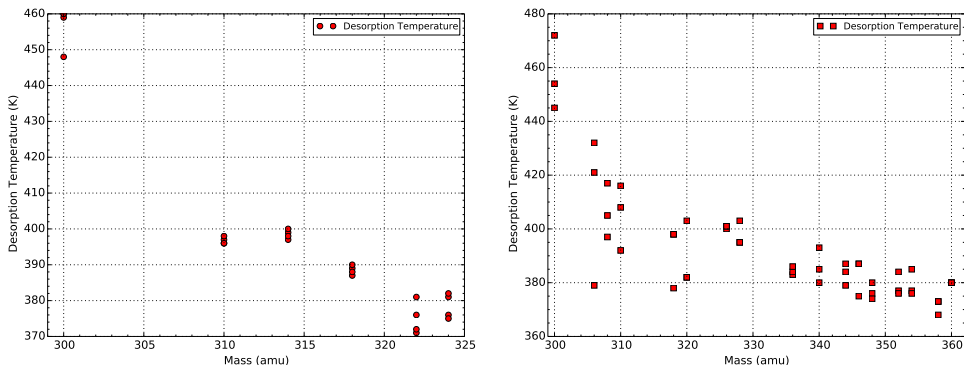


(a) Decay of pristine coronene for hydrogen addition.



(b) Decay of pristine coronene for deuterium addition.

**Figure 4.10:** The decay of the pristine coronene signal as a function of hydrogen (a) and deuterium (b) fluence. Each decay is fitted with multiple curves for different addition cross sections for the first atom. The best fit is found for cross sections of  $0.065 \text{ \AA}^2$  for hydrogen and  $0.25 \text{ \AA}^2$  for deuterium.



(a) Peak desorption temperatures for su- (b) Peak desorption temperatures for superdeuterated coronene.

**Figure 4.11:** The peak desorption temperature for a range of masses for hydrogen (a) and deuterium (b) addition to coronene on graphite, using atoms at a kinetic temperature of roughly 1000K.

which is seen for deuteration and hydrogenation with colder atoms. As a result it is worth re-examining the binding energy of the superdeuterated and superhydrogenated species.

When the peak desorption temperature of a molecule is known the desorption energy (the binding energy to the substrate) can be determined using the Redhead equation [146]:

$$E_{des} = k_B T_P \ln \left[ \left( \frac{\nu T_P}{\beta} \right) - 3.46 \right],$$

where  $T_P$  is the peak desorption temperature,  $\nu$  is a pre-exponential factor,  $\beta$  is the temperature ramp rate, and  $k_B$  is the Boltmann constant. The pre-exponential factor is assumed to be between  $8.9^{17} \text{s}^{-1}$  and  $4.8 \times 10^{18} \text{s}^{-1}$ , which has been determined for pristine coronene [84]. A pre-exponential factor of  $\nu = 2.9 \times 10^{18}$  was used to calculate the desorption energies.

The desorption temperatures for a range of mass configurations of hydrogenated and deuterated coronene on HOPG are plotted in Fig. 4.11. The desorption temperature is found for different peaks a different dose times. The desorption temperatures for superhydrogenated coronene are shown in Fig. 4.11(a) and those for superdeuterated coronene are shown in Fig 4.11(b). These temperatures are used to calculate the desorption energies of the species, which are shown in Fig. 4.12, for hydrogen (red circles)

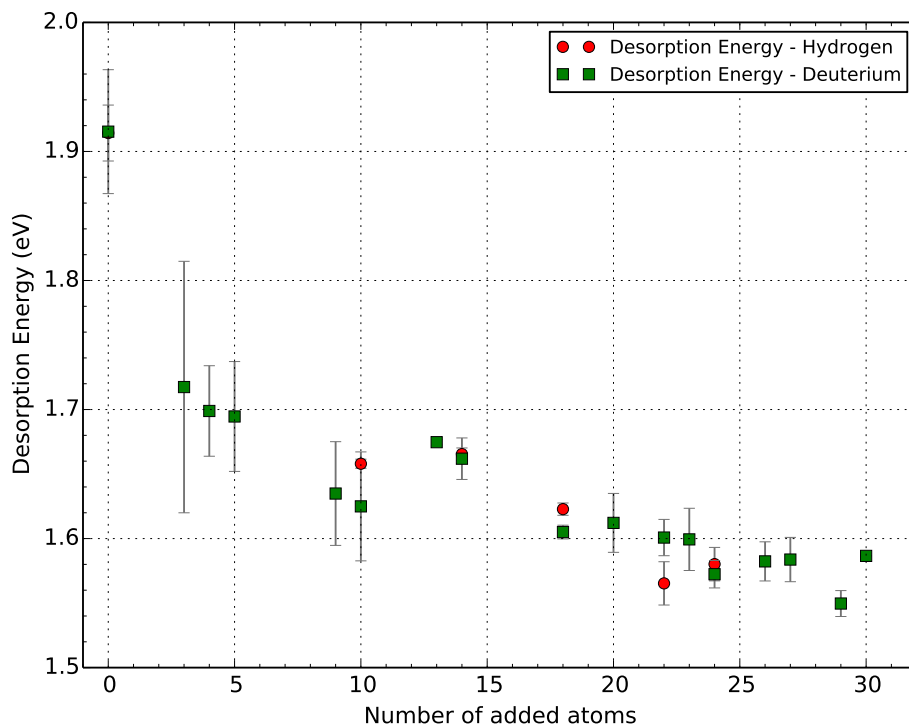


**Figure 4.12:** Desorption energies of superhydrogenated coronene (red circles) and superdeuterated coronene (green squares) from HOPG.

and deuterium (green squares) addition respectively. In this figure the desorption energies are plotted as a function of number of added atoms rather than mass, to allow direct comparison between hydrogenated and deuterated species.

The evolution of the binding energies with added atoms follow the same trend whether the coronene molecules are hydrogenated or deuterated, and the values are comparable within uncertainties, and so it does not appear to have an effect on the binding energy to the substrate whether hydrogen or deuterium is used in the addition reactions.

In order to compare the results to the previous study [83], the binding energies of superdeuterated coronene to HOPG are plotted in Fig. 4.13 for molecules exposed to hot (2300 K, blue triangles) and cold (1000 K, red squares) atoms. The data for the hot atoms is borrowed from [83], and their calculations were done using the same parameters as used here.

For the first 10 or so additions (masses 300 amu to 320 amu), the two curves

follow the same trend of decreasing desorption energy. There is a slight off-set, which may be explained by different temperature calibrations, and is corrected by normalising to the desorption temperature of the pristine coronene monolayer. When higher deuteration states are reached there is a clear diversion in the curves for the hot and cold atoms. Where the binding energies for the molecules deuterated with hot atoms continue to decrease rapidly until a mass of roughly 348 amu, only then to increase again, the binding energies for molecules exposed to cold atoms seems to level off after a mass of 320 amu, at a (normalised) binding energy of about 1.5 eV.

This difference in binding energies may be explained if the deuteration routes differ depending on the temperature of the atoms. This will probably be the case if barriers exist for deuterium or hydrogen addition to specific sites. It is worth noting that the diversion only appears after the addition of 10 atoms, the same number at which the first peak appears in the superhydrogenated coronene mass distribution. This then lends credit to the suggestion that there is a barrier for further additions, but that these may be more stable.

## 4.5 Summary

It has been shown that it is possible to superhydrogenate and deuterate the PAH molecule coronene with low temperature atoms down to 500 K. Some mass configurations are more stable than others, and could indicate potential barriers for some additions. It appears there is a difference of 6 atoms between the two last stable superhydrogenation stages, which could potentially be attributed to a barrier towards centre site addition. This is a hypothesis which will need to be tested further, through DFT calculations and further experiments. If it is confirmed it would mean that coronene on HOPG undergoes a different hydrogenation route than that proposed for a free standing coronene molecule by Rauls and Hornekær [74].

The cross section of addition of the first atom was calculated from the experimental data, and was found to be significantly higher for deuterium than for hydrogen. The theoretical model does not fit the deuterium data very well for high atom fluences, however, and it is possible that this is what causes the discrepancy. Another possibility is that functionalisation of coronene with hydrogen isotopes presents a route of deuterium enrichment of PAHs in the ISM. Further studies will be needed to confirm this hypothesis.

Finally, the binding energies of the superhydrogenated coronene species to

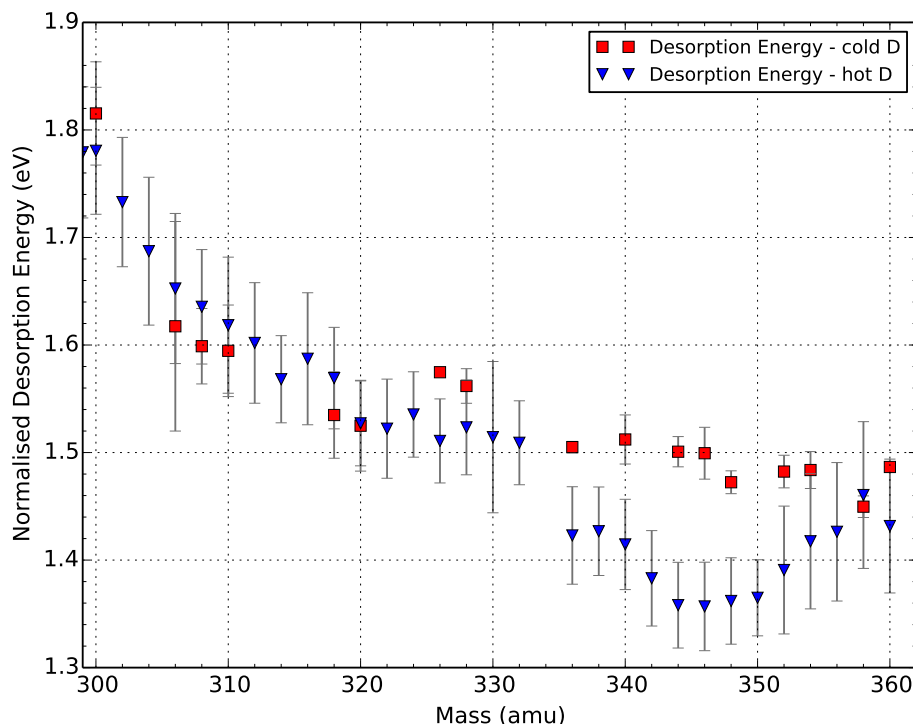


**Figure 4.13:** The binding energies to graphite measured for deuterated coronene with hot deuterium (blue triangles) and cold deuterium (red squares). Data for hot deuterium borrowed from [83].

the HOPG surface were investigated. It was found that for low degrees of hydrogenation and deuteration (up to 10 excess atoms), the binding energies follow the same decreasing trend as seen by Skov et al. [83], where deuteration was carried out at a higher atom beam temperature. However, for additions of more than 10 atoms, the binding energies start to diverge depending on the atom temperature. The binding energies of the molecules deuterated by hot atoms continue to decrease, until a minimum is reached, then increase slightly again. The binding energies of the molecules deuterated with colder atoms level off and remain almost constant within the uncertainties. This could suggest that different hydrogenation routes, leading to different molecular structures, are achieved depending on the temperature of the atomic beam.

# Chapter 5

## Experimental Results - Fullerenes

*It never hurts to keep looking for sunshine.*

— A. A. Milne, *Winnie the Pooh*

The buckminster fullerene  $C_{60}$  has been identified in only a few PNe and RNe in the ISM, and is expected to have a lifetime of only a few millions of years [112, 113]. However, it is very stable towards UV irradiation, and the interstellar radiation field is not enough to efficiently dissociate the pristine molecule.

Adding hydrogen to the molecule will disturb its aromaticity, and may well weaken the carbon skeleton sufficiently for it to become unstable against UV irradiation. In these experiments we aim to grow a monolayer of  $C_{60}$  molecules on a substrate, hydrogenate it, and UV irradiate it. Every step will be analysed using STM.

The experiments and image selection presented here were performed in collaboration with Dr. Martha Scheffler. The analysis was carried out by me. A very limited time window of two weeks was available for these experiments, and as a consequence, the results presented here are very preliminary, and while a hydrogenated monolayer of  $C_{60}$  on Au(111) was obtained, there was not enough time to complete the UV irradiation part of the experiment, not to transfer the system to a HOPG surface.

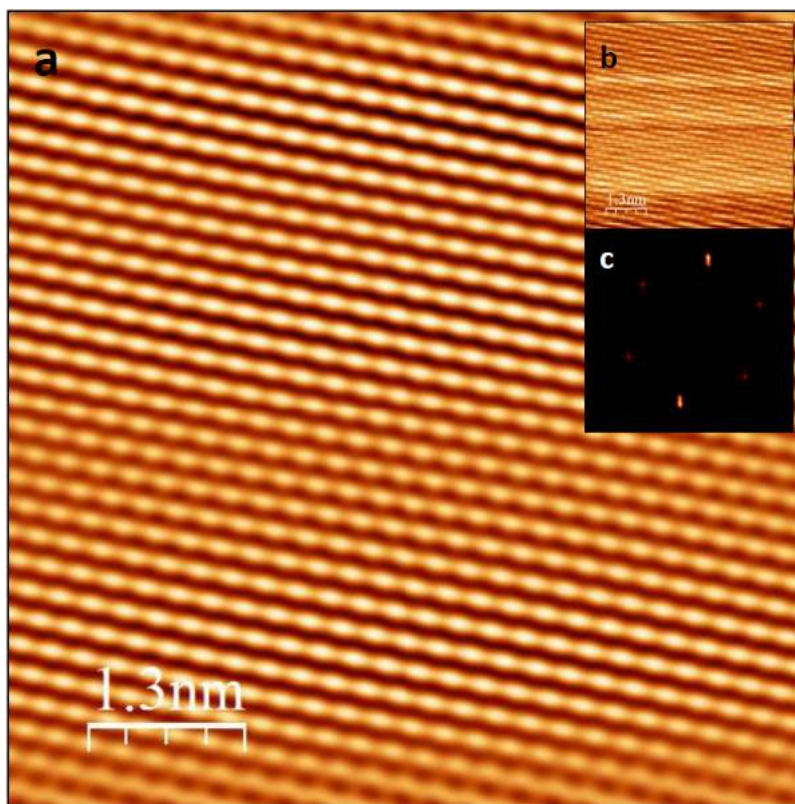


**Figure 5.1:** Atomically resolved clean HOPG, used for calibrating the piezo elements. Scanning parameters:  $I_t = -0.900$  nA,  $V_t = -5.2$  V.

## 5.1 $C_{60}$ on HOPG and Au(111)

The STM is calibrated using clean HOPG. Fig. 5.1 shows an STM image of atomically resolved clean HOPG. The main image (a) has been filtered to remove noise, using the Fourier transform. The original image is shown in the insert (b). The insert (c) shows the Fourier transform used in the calibration. The distance between opposite dots in the Fourier transform is measured as the inverse of the wavevector,  $1/k$ . In the case of HOPG, where every second atom is seen in an atomically resolved image, this should have a value of 2.13. The measured value is 1.71, and a correction factor of 1.25 must be applied to the images to obtain the correct scaling. The scale bar in Fig. 5.1 and every subsequent image shows the corrected scale. Furthermore filters have been applied to flatten the images and heighten the contrast.

### 5.1.1 HOPG

HOPG is often used as a substrate in astrochemical experiments to model carbonaceous dust grains in the ISM. It is also a useful substrate for studying reactions independent of the surface because it, in the case of physisorption, has a lower interaction with the adsorbate than various metal surfaces. This is because it is very difficult to create a dipole-dipole interaction between the adsorbate and the graphite structure, owing to the electronic structure of graphite.

As a result performing the  $C_{60}$  hydrogenation experiments on HOPG would be preferable. Fig. 5.2 shows the growth of  $C_{60}$  on HOPG. In this case  $C_{60}$  was dose at a sublimation temperature of 652 K for 30 s.

The molecules cluster together and grow in a dendritic fashion from the stepped edges of the graphite. Annealing the sample in steps up to 900 K had no effect on the structure of the molecules, and it was not possible to clean the crystal sufficiently to prevent further dosing from growing from the structures already present on the surface. As a consequence of the problems with dosing  $C_{60}$  on HOPG and the very limited time allotted for the experiment, a decision was made to switch to a gold surface (specifically Au(111) foil on Mica, which from now on will be referred to as Au(111)), where  $C_{60}$  is known to form ordered structures [147].

### 5.1.2 Au(111)

The Au(111) foil was cleaned through sputtering with  $Ar^+$  ions at a pressure of  $3 \times 10^{-6}$  mbar for 10 minutes, followed by annealing to 720 K for 5 minutes. This cycle was repeated a total of seven times overnight.

The first attempt at dosing  $C_{60}$  on Au(111) is shown in Fig. 5.3 (a,b). In this case the molecules were dosed at a sublimation temperature of 648 K for 45 s. The result is a very low coverage, with only a few molecules sticking to the step edges of the surface, and the herringbone reconstruction of the clean surface easily distinguishable on the terraces. Dosing another 5 min at a higher sublimation temperature of 662 K results in the kind of coverage shown in Fig. 5.3(c), where the step edges on the surface are completely saturated with molecules, but the coverage in general is still very low.

When the step edges are saturated, islands start to grow, shown in Fig. 5.4. The dosing parameters in this case is an additional 15 minutes at a sublimation temperature of 673 K. A large scale image of the islands is shown in Fig. 5.4(a), showing many small islands, some 20-30 nm across

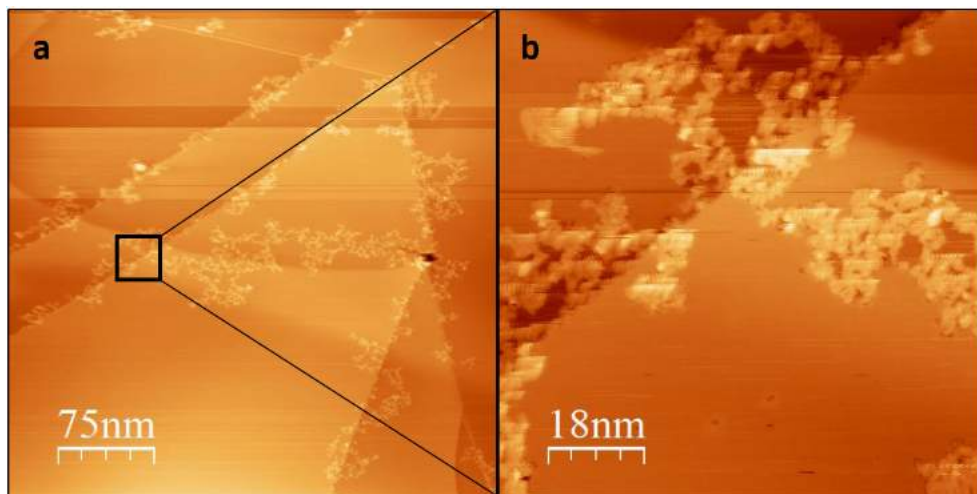


**Figure 5.2:**  $C_{60}$  molecules on HOPG. The growth happens from the step edges in a dendritic fashion, and some clustering is observed. Scanning parameters: (a)  $I_t = -2.29$  nA,  $V_t = -1277.1$  mV; (b)  $I_t = -0.650$  nA,  $V_t = -1164.8$  mV.

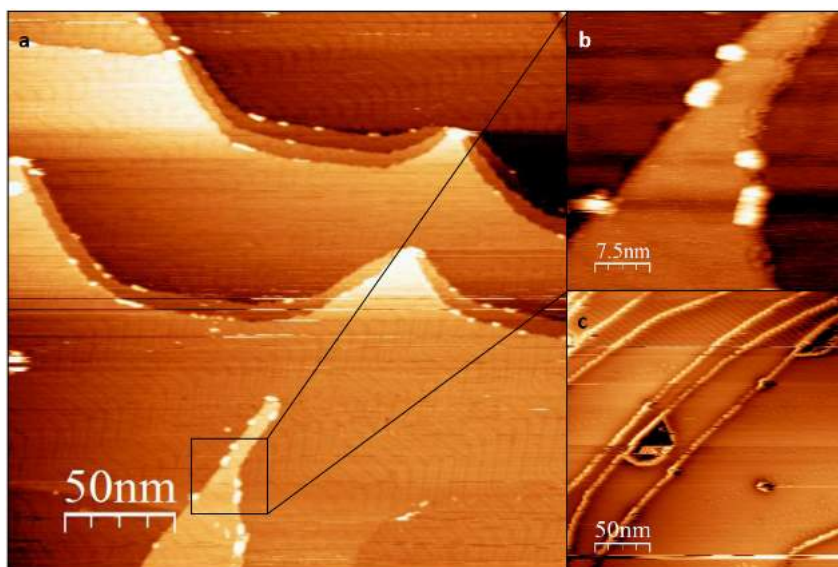


**Figure 5.3:**  $C_{60}$  growth on Au(111) after a 45 s dose at 603 K (a, b), and a further 45 s at 648 K (c). Scanning parameters: (a)  $I_t = 0.350$  nA,  $V_t = 2087.1$  mV; (b)  $I_t = 0.140$  nA,  $V_t = 2087.1$  mV; (c)  $I_t = -0.250$  nA,  $V_t = -2152.4$  mV.

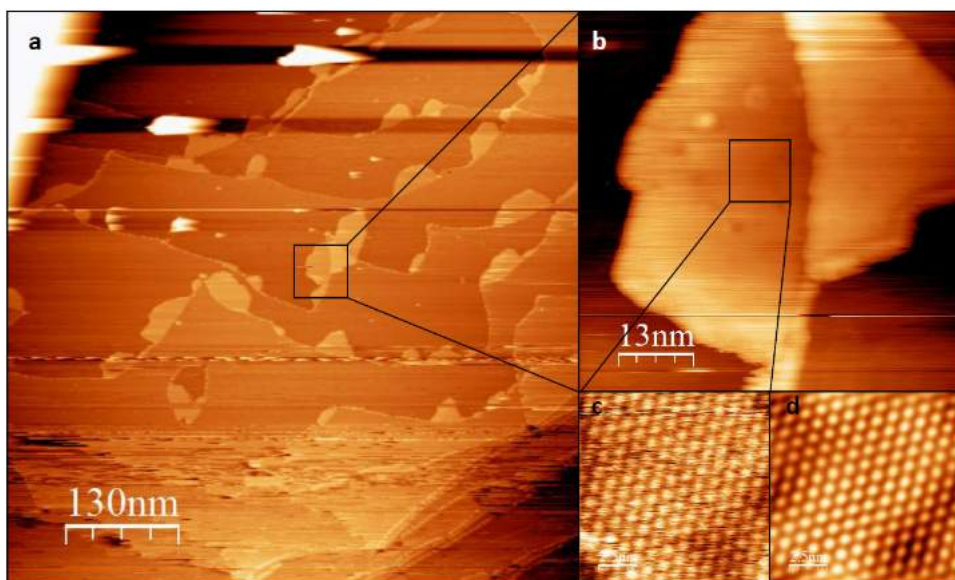


**Figure 5.4:** When step edges have been saturated  $C_{60}$  on Au(111) starts to grow small, densely packed islands, on which molecular resolution is obtained. Scanning parameters: (a)  $I_t = 0.350$  nA,  $V_t = 2087.1$  mV; (b)  $I_t = -0.140$  nA,  $V_t = -2087.1$  mV; (c)  $I_t = -0.170$  nA,  $V_t = -2152.4$  mV. d) is the same image as c) with a FFT filter applied to remove noise.

growing from step edges on the Au(111) surface. A zoom in on one of the islands is shown in Fig. 5.4(b). It is possible to obtain molecular resolution on the island, shown in the zoom in in Fig. 5.4(c). A FFT filter is applied in Fig. 5.4(d) to remove noise. At this coverage the surface is not very uniform, and many tip changes result, and a higher coverage is needed to obtain a stable surface, where hydrogenation will be possible to study. From these results it seems growth of  $C_{60}$  on Au(111) starts at the step edges and island growth will not begin until the edges are completely saturated. Growth takes place in an orderly fashion, and once the molecules are at a step edge or part of an island they are no longer mobile on the surface.

A ML of  $C_{60}$  on Au(111) is obtained by dosing at a sublimation temperature of 713 K for 20 minutes on a clean sample. This dose results in a coverage slightly above 1 ML, and as a result the structure is somewhat disordered. Annealing to 420 K desorbs the multilayers and results in a well-ordered, densely packed monolayer with few defects, as shown in Fig.

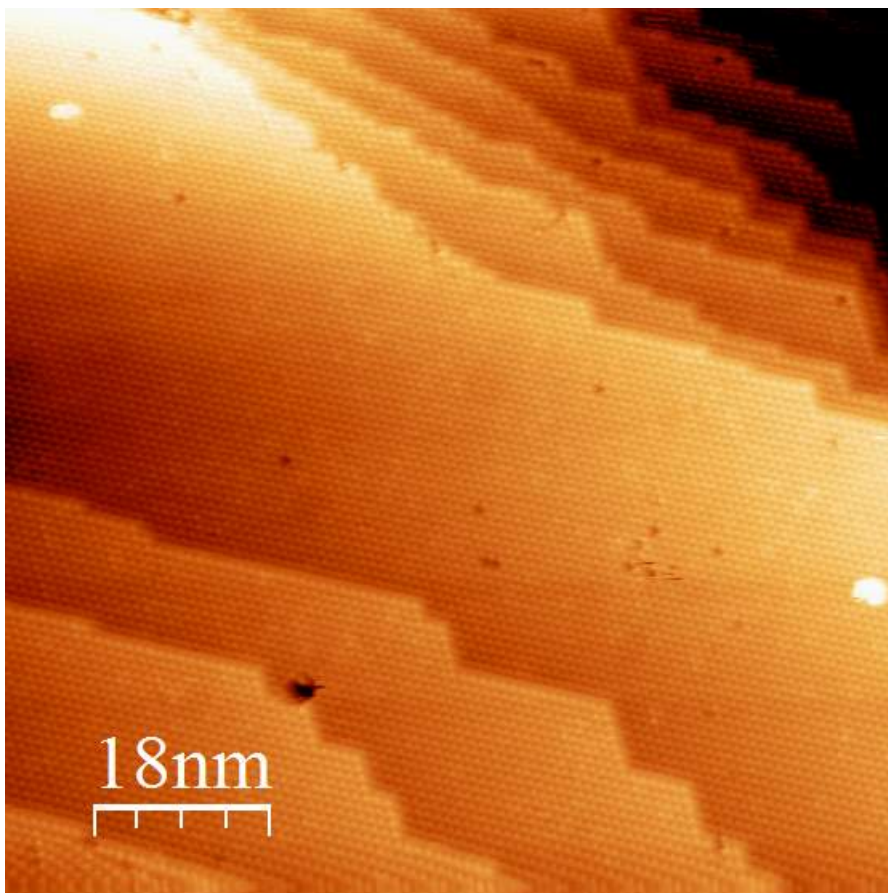


**Figure 5.5:** Monolayer of  $C_{60}$  on Au(111). Scanning parameters:  $I_t = -0.140$  nA,  $V_t = -1632.7$  mV.

5.5, where molecular resolution is easily achieved, even at a relatively large scale.

## 5.2 Deuteration of $C_{60}$ on Au(111)

A relatively low degree of deuteration of the  $C_{60}$  ML is shown in Fig. 5.6. This degree of hydrogenation was obtained by backfilling the chamber with D atoms through the cracker to a base pressure of  $3 \times 10^{-8}$  mbar for approximately 10 minutes, while the sample was still in the STM, followed by annealing the sample to 420 K.

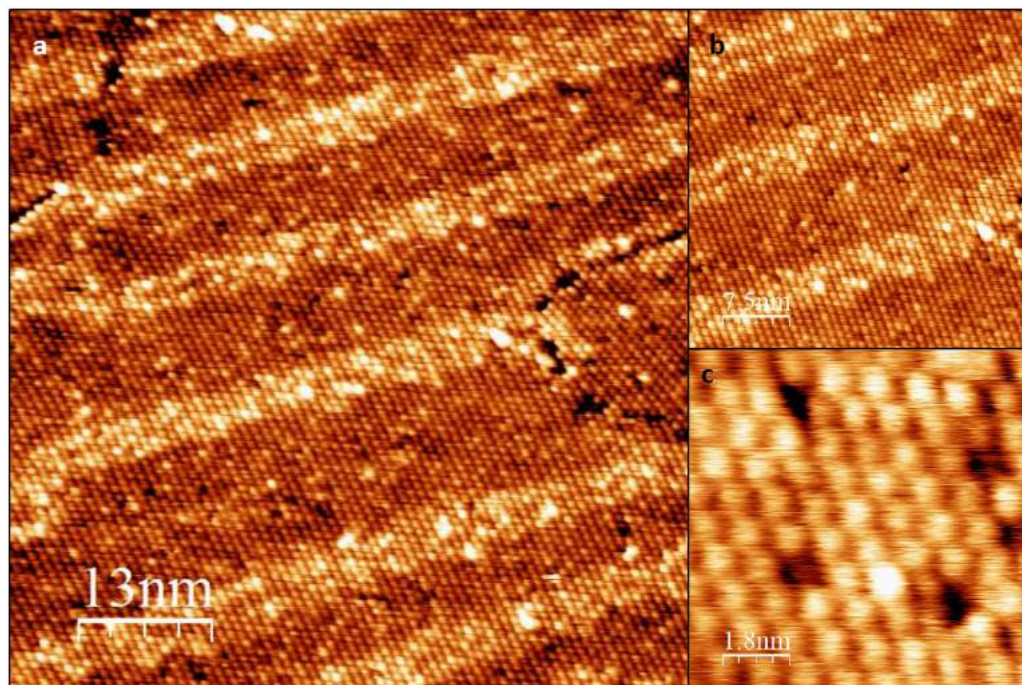


**Figure 5.6:** Low degree of deuteration of  $C_{60}$  on  $Au(111)$ . Deuterated by backfilling the chamber with deuterium through the H cracker at a pressure of  $3 \times 10^{-8}$  mbar for between 5 and 10 minutes while sample resided in the STM, followed by an anneal to 420 K. Scanning parameters: (a,b)  $I_t = -0.110$  nA,  $V_t = 0.260$  nA,  $V_t = 1846$  mV.

The molecules are still resolvable, but appear in varying degrees of brightness, corresponding to brighter molecules being deuterated. At least three different brightnesses are observed, likely corresponding to pristine  $C_{60}$  and two or more deuteration states, with the brightest molecules exhibiting the highest degree of deuteration. At this overall degree of deuteration more than half the ML still appears undeuterated, and the herringbone reconstruction of the  $Au(111)$  surface is visible under the layer of molecules.

To obtain a higher degree of deuteration the sample was exposed to a beam of deuterium atoms directly in front of the H cracker, for 5 s, and annealed to 500 K. This results in just over two thirds of the molecules appearing deuterated to various degrees. This is shown in Fig. 5.7. From direct comparison with Fig. 5.6, it is clear that many more molecules are deuterated, and from the increase in very bright dots, it seems higher deuteration

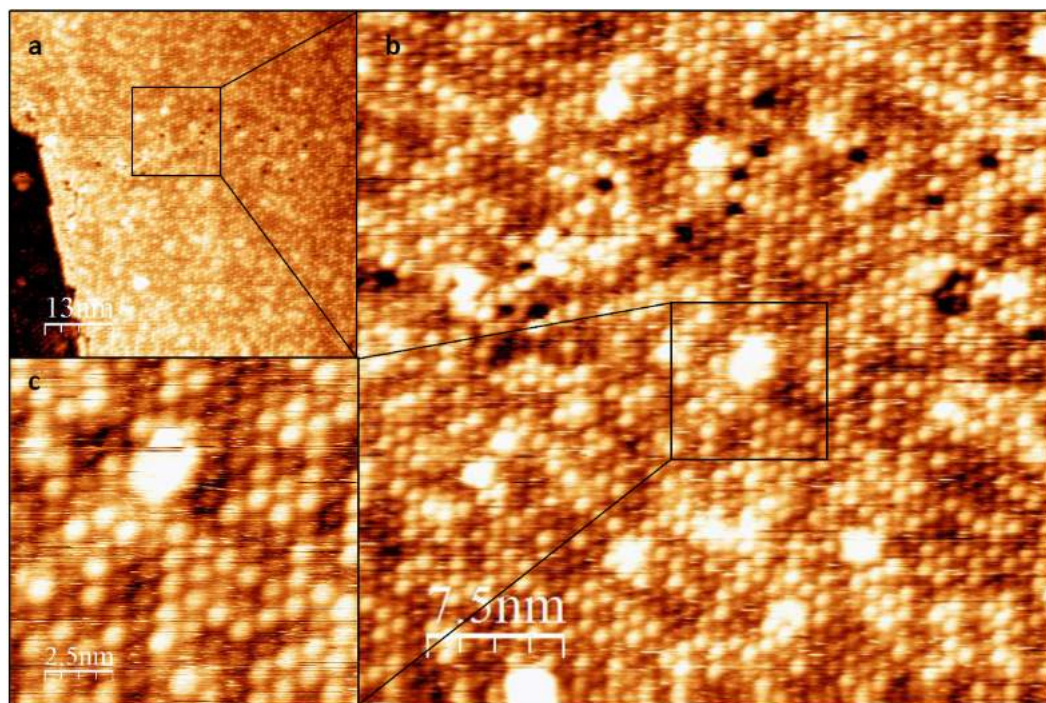


**Figure 5.7:** High degree of deuteration of  $C_{60}$  on Au(111), achieved by exposing sample directly to a beam of deuterium atoms at 2300K for 5 s, followed by an anneal to 500 K. Scanning parameters: (a)  $I_t = -0.120$  nA,  $V_t = -1790.1$  mV; (b)  $I_t = -0.140$  nA,  $V_t = -1790.1$  mV; (c)  $I_t = -0.110$  nA,  $V_t = -1962.9$  mV.

states are achieved. In addition to the same three or so different brightnesses seen for the low degree of deuteration there are also a number of very bright, extended blobs. These could possibly be attributable to either a very high degree of deuteration of one molecule, or a cluster of moderately deuterated molecules. It is possible to get rid of the extended bright blobs by annealing to 500 K a second time, the result of which is shown in Fig. 5.8. The  $C_{60}$  layer maintains a very high deuteration state with the molecules showing three different brightnesses, but the very bright, extended blobs are not present.

It has not been possible to resolve the lobe structure of the molecules, either in deuterated or pristine form. As a result it is difficult to speculate on the actual degree of deuteration obtained for the individual molecules. It is clear though, that some degree of deuteration of most of the molecules in

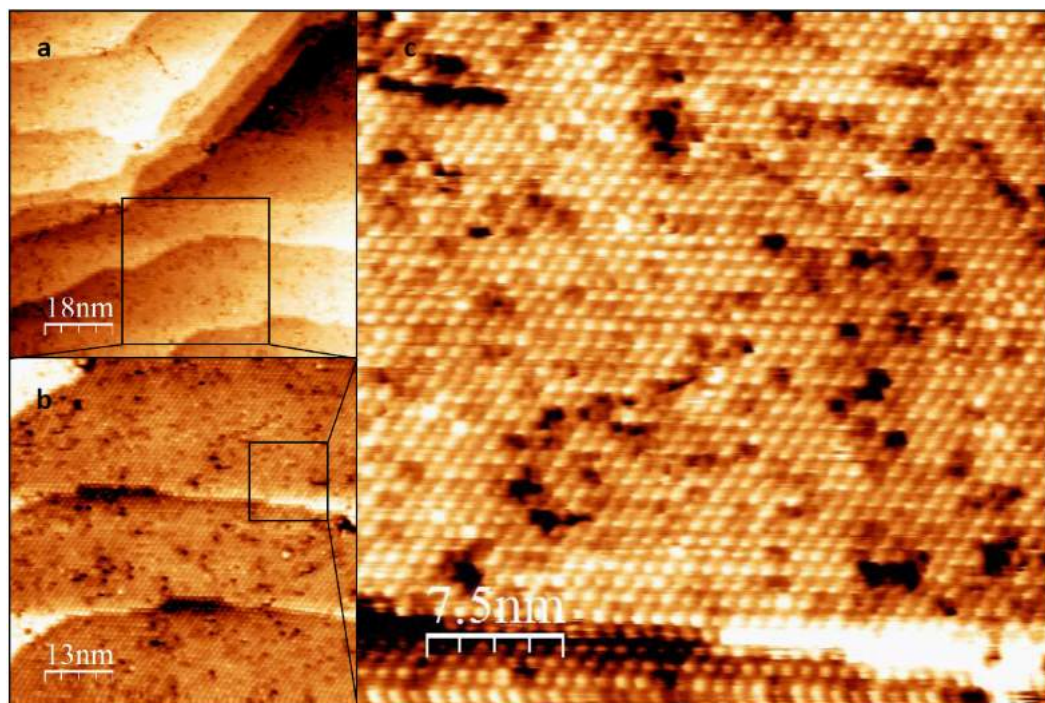


**Figure 5.8:** High degree of deuteration of  $C_{60}$  on Au(111), achieved by exposing sample directly to a beam of deuterium atoms at 2300K for 5 s, followed by annealing to 500 K twice. Scanning parameters: (a)  $I_t = -0.110$  nA,  $V_t = -1164.8$  mV; (b)  $I_t = -0.120$  nA,  $V_t = -1164.8$  mV; (c)  $I_t = -0.130$  nA,  $V_t = -1164.8$  mV

the monolayer is easily achievable.

The next step is to UV irradiate the deuterated monolayer of  $C_{60}$ . This can be done while scanning, and it will be possible to observe any polymerisation or other changes in real time.



# Chapter 6

## Astrophysical Observations

*It is not in the stars to hold our destiny, but in ourselves.*

— William Shakespeare, *Julius Ceasar*

The work presented in this chapter was carried out over a four months stay at University of Western Ontario, under the supervision of prof. Els Peeters, and with support from Drs. Matthew Shannon and David Stock. The aim of this investigation is to relate the results of my experiments to an astronomical environment, and to determine whether superhydrogenated PAHs can be found in space, and where. I also investigate whether there is a relation between the astronomical PAH class of an object and the degree of aromaticity of the emitting population. The work has led to the article Aliphatic Features in the 6-12  $\mu\text{m}$  Mid-Infrared Polycyclic Aromatic Hydrocarbon Spectra [66], which is ready to be submitted to the journal *Astronomy and Astrophysics*.

### 6.1 Introduction

It is well established that the emitting PAH population, and by extension their physical and chemical environment, can be characterised through comparison between observed and experimentally measured spectra, see e.g. [48, 49, 50, 51, 52, 54, 55, 56, 57]. The spectral profiles and peak positions of the PAH features may vary between objects, and even spatially within extended objects, and based on this variation the spectra are divided into

four PAH classes, A, B, C, and D, as discussed in section 1.3.2. The PAH classes are found to vary somewhat depending on object type, with class A emission usually found in ISM objects, class B emission covering a large variety of objects from YSOs to PNe, and classes C and D mostly found in pAGB stars, prior to the PN stage. The spectral variation between the PAH classes reflect a change in the emitting population, and it is possible that it may be caused by a varying importance of aliphatic material, see e.g. [61, 12, 62, 63, 64, 65], which we study in more detail here.

The degree of aromaticity can be studied directly through bands at 3.4, 6.9, and 7.25  $\mu\text{m}$ , which are aliphatic in nature [67, 68, 69, 42, 43]. However, it is not obvious what type of aliphatic material is the cause of these bands in the ISM, as they are present in many types of aliphatic molecules, like hydrocarbon chains, methyl sidegroups on larger molecules, and superhydrogenated PAHs. The object here is to study the aliphatic bands at 6.9 and 7.25  $\mu\text{m}$  in the PAH spectra of a large sample of objects, in order to determine what type of aliphatic material causes them to appear, and whether there is a preference for certain types of object and any correlation with PAH class.

## 6.2 Sample

The sample consists of 63 galactic and Magellanic Cloud sources in total, sixty-two spectra selected from literature [47, 12, 13, 63, 148, 149, 150, 44, 59], and one previously unpublished spectrum, observed with the FORCAST instrument [151] on SOFIA [152, 153]. Two selection criteria were applied to the sources previously observed with the Short Wavelength Spectrometer [154, SWS] on the Infrared Space Observatory [155, ISO], and the Infrared Spectrograph [156, IRS] on the Spitzer Space Telescope [157] to determine the sample. Firstly we considered all sources which had previously shown evidence of emission at 3.4, 6.9, and/or 7.25  $\mu\text{m}$ . Secondly we looked at a large number of sources classified as B, C, or D sources [47, 58, 59], as these are the sources expected to show the strongest aliphatic emission [12, 13].

The sample also includes six class A or AB spectra. These were included because they have either previously shown evidence of aliphatic emission or previously been misclassified. Evidence of the aliphatic feature at 6.9  $\mu\text{m}$  was found in two of the sources, whereafter all class A or AB sources from Sloan et al. [12, 13] were investigated in case the aliphatic feature had been missed in any of those. No evidence for aliphatics was found in any

further sources. Twelve of the 63 sources were observed with ISO-SWS and the remainder with Spitzer-IRS.

IRAS05341+0852 was observed with the FORCAST instrument on SOFIA (PI: Peeters, ID: 03\_0032), and it was chosen because it has previously shown an unusually strong aliphatic feature at  $3.4 \mu\text{m}$  [11], but no mid-IR spectrum has previously been published. The observation was carried out using the FORCAST cross-dispersed grisms, FOR\_XG063 and FOR\_XG111.

Of the total sample of 63 objects, thirty-four exhibit an emission feature at  $6.9$  and/or  $7.25 \mu\text{m}$ , detected at a signal-to-noise ratio of 3 or higher. Eleven exhibit a feature at  $7.25 \mu\text{m}$ , while 31 exhibit a feature at  $6.9 \mu\text{m}$ .

The sources in the sample were identified using the SIMBAD database [158] and the SAGESpec (Surveying the Agents of Galaxy Evolution: Spectroscopy) Spitzer legacy program [159], by following Sloan et al. [13]. Using these tools it was possible to identify the object type of 60 of the 63 sources. The sample contains 33 pAGB stars, 16 PNe, five Herbig AeBe stars, three variable stars, and two emission line stars. The full list of sources, including their object type, PAH class, and whether or not they exhibit aliphatic emission, can be found in Table. 6.1.

## 6.3 Analysis Methods

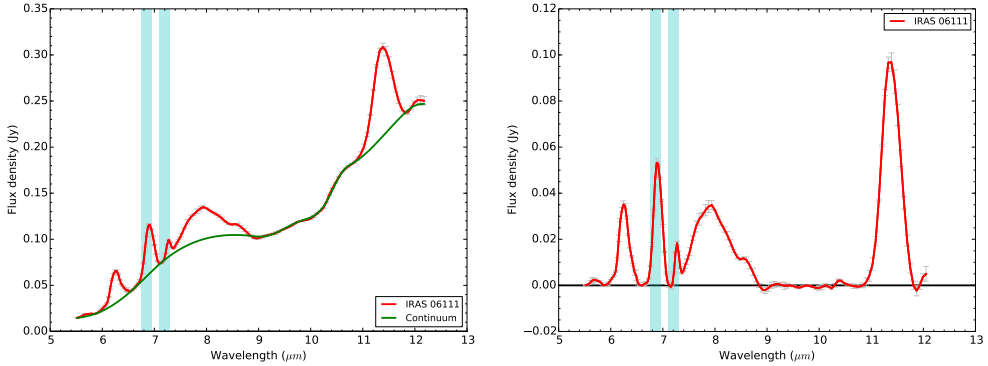
First, a dust continuum is fit to every spectrum in the sample, using a spline function anchored on points adjacent to known PAH features. This is a method which has been used successfully a number of times before [160, 47, 148, 161, 162, 163, 164]. The continuum is drawn under the full  $7.7 \mu\text{m}$  complex rather than anchoring it between the  $7.7$  and  $8.6 \mu\text{m}$  features, to ensure consistent classification of all spectra [12, 13]. An example of a spectrum before and after continuum subtraction can be seen in Fig. 6.1(a,b).

After continuum subtraction the integrated fluxes of the relevant features are measured. To find the integrated fluxes of the  $6.2$  and  $11.2 \mu\text{m}$  features, we simply integrate across the feature, starting the integration at  $6.1$  and  $11.1 \mu\text{m}$  respectively, to avoid contamination from the  $6.0$  and  $11.0 \mu\text{m}$  features. The aliphatic bands at  $6.9$  and  $7.25 \mu\text{m}$  are fitted with one Gaussian function each, which is then integrated to find the flux. A  $3\sigma$  SNR criterion

Table 6.1: The sample

Source	AOR key / TDT	Object type	PAH class	Aliphatics?	Instrument	Reference
BD+30 3639	86500540	PN	B	no	ISO/SWS	9
CRL 2688	35102563	post-AGB	C	no	ISO/SWS	9
HD 34282	3577856	Herbig AeBe star	B	yes	Spitzer/IRS	1
HD 44179	70201801	post-AGB	B	no	ISO/SWS	7
HD 135344	3580672	Herbig AeBe star	B	yes	Spitzer/IRS	1
HD 139614	3580928	Herbig AeBe star	B	yes	Spitzer/IRS	1
HD 141569	3560960	Herbig AeBe star	B	no	Spitzer/IRS	1
HD 169142	3587584	Herbig AeBe star	B	yes	Spitzer/IRS	1
He2 113	43400768	PN	B	no	ISO/SWS	9
HR4049	17100101	post-AGB	B	no	ISO/SWS	9
IRAS f05110-6616	25992704	post-AGB	D	yes	Spitzer/IRS	2
IRAS f05192-7008	24314624	post-AGB	B	yes	Spitzer/IRS	2, 6
IRAS z05259-7052/J052520	25996032	post-AGB	D	yes	Spitzer/IRS	2, 6
IRAS 00350-7436	27517184	post-AGB	B	yes	Spitzer/IRS	6
IRAS 05063-6908	19006720	post-AGB	D	yes	Spitzer/IRS	2, 6
IRAS 05073-6752/J050713	24317184	post-AGB	D	yes	Spitzer/IRS	2, 6
IRAS 05092-7121	25992448	post-AGB	B	yes	Spitzer/IRS	2, 6
IRAS 05127-6911/J051228	24316928	post-AGB	A	no	Spitzer/IRS	2, 6
IRAS 05185-6806	19011840	post-AGB	B	yes	Spitzer/IRS	6
IRAS 05341+0852	-	post-AGB	-	yes	SOFIA/FORCAST	-
IRAS 05360-7121	19008256	post-AGB	B	yes	Spitzer/IRS	6
IRAS 05370-7019	24315648	post-AGB	B	no	Spitzer/IRS	6
IRAS 05413-6934/Cluster35	23884032	post-AGB	D	yes	Spitzer/IRS	6
IRAS 05537-7015	27084032	post-AGB	B	no	Spitzer/IRS	2, 6
IRAS 05588-6944	25992960	post-AGB	B	yes	Spitzer/IRS	2, 6
IRAS 06111-7023	19013120	post-AGB	D	yes	Spitzer/IRS	6
IRAS 07027-7934	73501035	PN	B	no	ISO/SWS	9
IRAS 13416-6243	62803904	post-AGB	C	no	ISO/SWS	7
IRAS 14429-4539	25453824	post-AGB	B	yes	Spitzer/IRS	4
IRAS 15482-5741	25454336	post-AGB	D	yes	Spitzer/IRS	4
IRAS 17047-5650	13602083	PN	B	yes	ISO/SWS	9
IRAS 17311-1553	-	-	B	no	ISO/SWS	9
IRAS 17347-3139	87000939	PN	B	yes	ISO/SWS	9
IRAS 18379-1707	17502976	post-AGB	B	no	Spitzer/IRS	3
IRAS 19306+1407	17509888	post-AGB	B	no	Spitzer/IRS	3
IRAS 20462+3416	17504512	post-AGB	B	no	Spitzer/IRS	3
IRAS 22023+5249	17505024	post-AGB	B	no	Spitzer/IRS	3
J00444111-7321361	27525120	Variable star	D	yes	Spitzer/IRS	6
J01054645-7147053	27518464	emission line star	D	yes	Spitzer/IRS	6
J05204385-6923403	27985920	Variable star	D	yes	Spitzer/IRS	2, 6
MSX SMC 029	10656256	post-AGB	B	yes	Spitzer/IRS	7
MWC 922	70301807	emission line star	B	no	ISO/SWS	9
NGC 1978 WBT2665	11239680	post-AGB	D	yes	Spitzer/IRS	6
SMP LMC 008	15902464	-	B	no	Spitzer/IRS	6, 8
SMP LMC 013	4947968	PN	B	no	Spitzer/IRS	8
SMP LMC 025	14701568	-	A	no	Spitzer/IRS	6
SMP LMC 036	4949248	PN	B	no	Spitzer/IRS	8
SMP LMC 038	12633600	post-AGB	B	no	Spitzer/IRS	8
SMP LMC 051	22421504	PN	B	no	Spitzer/IRS	6
SMP LMC 058	4950784	post-AGB	B	yes	Spitzer/IRS	6, 8
SMP LMC 061	12633856	post-AGB	B	no	Spitzer/IRS	8
SMP LMC 075	25993984	PN	B	yes	Spitzer/IRS	2
SMP LMC 076	4951296	post-AGB	B	yes	Spitzer/IRS	6, 8
SMP LMC 078	15902208	PN	B	no	Spitzer/IRS	8
SMP LMC 085	4952320	PN	AB	no	Spitzer/IRS	8
SMP LMC 099	14705664	PN	B	no	Spitzer/IRS	5
SMP SMC 001	4953088	post-AGB/PN	B	yes	Spitzer/IRS	6, 8
SMP SMC 003	4953600	PN	B	no	Spitzer/IRS	8
SMP SMC 006	4954112	PN	B	yes	Spitzer/IRS	6, 8
SMP SMC 011	15902976	PN	A	yes	Spitzer/IRS	6, 8
SMP SMC 018	14707456	post-AGB	A	no	Spitzer/IRS	6
SMP SMC 020	14707968	PN	AB	yes	Spitzer/IRS	6
XX-Ophiuchus	46000601	Variable star	B	yes	ISO/SWS	9

(1) keller2008; (2) matsu2014; (3) cerri2009; (4) cerri2011; (5) CASSIS cassis; (6) sloan2014; (7) sloan2007; (8) bernard2009; (9) peeters2002 The AOR (Astronomical Observation Request) key uniquely defines a *Spitzer* observation. The TDT (Target Dedicated Time) uniquely identifies an ISO-SWS observation. [Ar II] means that an argon line was at first misidentified as an aliphatic feature.



(a) The spectrum of IRAS06111 with the continuum drawn in green. (b) The continuum subtracted spectrum of IRAS06111.

**Figure 6.1:** The spectrum of IRAS 06111, showing the continuum spline fit (a) and the continuum subtracted spectrum (b).

is applied for a positive detection.

To decompose the  $7.7 \mu\text{m}$  complex, four Gaussian functions are fitted to the complex from approximately  $7\text{--}9 \mu\text{m}$ . This is done in order to i) be able to isolate the  $8.6 \mu\text{m}$  feature in spectra where it is clearly separate from the rest of the complex and ii) make it easier to deal with noisy spectra [165, 166]. Four Gaussian functions are used because it is the smallest number which can fit the entire complex. The central wavelengths and full width half maxima (FWHM) of the Gaussian functions are allowed to vary to ensure the best fit to a given spectrum. This is necessary since the  $7.7 \mu\text{m}$  complex shifts as a whole [47]. This is especially true for class B spectra. An example of the decomposition of the  $7.7 \mu\text{m}$  feature is presented in Fig. 6.2.

### 6.3.1 Classification

The central wavelength of the  $7.7 \mu\text{m}$  complex is determined by finding its bisector [12, 13], accepting an error less than 1%. The sources are then classified according to the central wavelength and shape of their  $7.7 \mu\text{m}$  complex.

Class A sources have a central wavelength  $\lambda_c > 7.7 \mu\text{m}$ , and the feature at  $8.6 \mu\text{m}$  is a clearly distinguishable, separate feature. For class B sources  $7.7 < \lambda_c < 8.0 \mu\text{m}$ . The feature at  $8.6 \mu\text{m}$  is still a separate feature, though

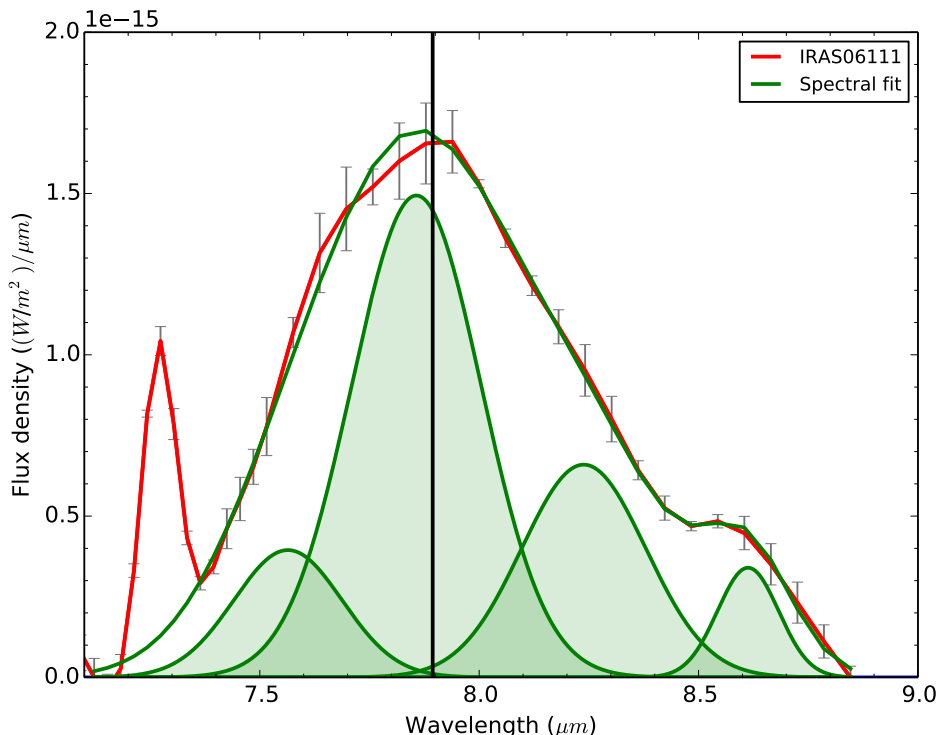


**Figure 6.2:** The  $7.7 \mu\text{m}$  complex of IRAS06111. The Gaussian functions used to decompose the spectrum are filled in, and the green curve shows the total fit to the spectrum. The vertical black line marks the central wavelength of the complex.

it may appear more blended than in class A sources. There is much variation across the class. Class C sources have very red central wavelengths, with  $8.15 \mu\text{m} < \lambda_c < 8.20 \mu\text{m}$ , and do not show a separate feature at  $8.6 \mu\text{m}$ . The entirely  $7.7 \mu\text{m}$  complex in a class C source is one broadened feature reaching from approximately  $7.5$  to  $9 \mu\text{m}$ . Class D sources tend to have a redder central wavelength than class B sources, but without quite as much variation, and not as red as class C. Typically,  $7.9 \mu\text{m} < \lambda_c < 8.0 \mu\text{m}$ . The feature at  $8.6 \mu\text{m}$  tends to be weak and/or very blended. The different PAH classes are discussed in further detail in [47, 58, 59].

A typical spectrum belonging to each of the four classes can be seen in Fig. 6.3, clearly illustrating the differences between the classes in shape and wavelength of the  $7.7 \mu\text{m}$  complex. This sample contains four class A

sources, and two sources which were neither obvious class A or B sources, but somewhere in between. There are also 44 class B sources, two class C sources, and 11 class D sources.

The source IRAS 05341+0852 was observed using FORCAST/SOFIA, which has a gap in the spectrum from approximately 7 to 9  $\mu\text{m}$ , and so cannot be classified according to its 7.7  $\mu\text{m}$  complex. However it has been shown that the peak wavelengths of the 6.2 and 11.2  $\mu\text{m}$  bands are correlated to the central wavelength of the 7.7  $\mu\text{m}$  complex, and therefore also reflects PAH class [47, 58, 12], and so IRAS 05341+0852 can be tentatively classified using those bands.

We measure  $\lambda_p(6.2) = 6.27 \pm 0.02 \mu\text{m}$  and  $\lambda_p(11.2) = 11.35 \pm 0.02 \mu\text{m}$ . The peak wavelength of the 6.2  $\mu\text{m}$  feature is redder than the expectation for class A sources, but close to the red end of what is expected for class B. The wavelength of the 11.2  $\mu\text{m}$  feature however is much longer than would be expected for either A and B. Comparing to [12], based on the central wavelengths of the 6.2 and 11.2  $\mu\text{m}$  features, the central wavelength of the 7.7  $\mu\text{m}$  complex is expected to fall between 8.15 and 8.20  $\mu\text{m}$ , and thus IRAS 05341+0852 is most likely a C class source.

## 6.4 Results

The results can be divided into three parts. First band profile variations in the different PAH classes are investigated, then the profiles of the aliphatic features are studied, and lastly any correlations present between features are determined.

### 6.4.1 PAH Class and Band Profiles

The sample spans all four PAH classes and a large range of astronomical objects. Insofar as the objects could be identified, we have studied any correlations and trends between object type and PAH class. The C and D class sources in our sample were mostly pAGB stars, with some variable stars present among the class D sources as well. IRAS 05341-0852, which is expected to exhibit C class emission is also a pAGB star. The C and D class sources in the sample contain no PNe or YSOs. This would suggest that C and D class sources are mainly circumstellar environments where significant mass loss and dust formation is ongoing or has very recently taken place.

The B class sources in the sample encompass a large variety of objects from

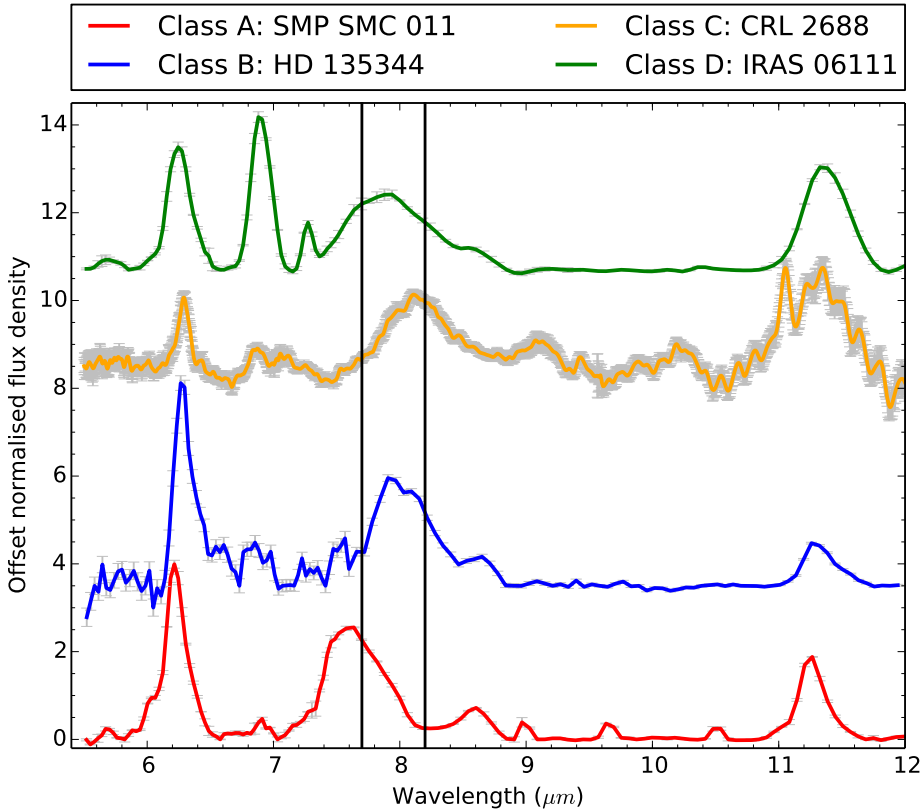


**Figure 6.3:** Four spectra showing typical class A, B, C, and D profiles respectively.

YSOs to PNe and anything in between, whereas all the class A sources in this sample are PNe. The sample contains no ISM objects, most probably because our sample selection criteria are biased towards B, C, and D class sources.

It has previously been shown that class A and C spectra vary very little between objects, whereas there is a very large variation in B class spectra across different objects [47, 58]. Here we investigate whether there is any variation in D class spectra across different objects.

There are 11 D class objects in the sample, the average spectrum of which is shown in Fig. 6.4. The three D class spectra showing the most variation with respect to the average are plotted on top, and the average central wavelength ( $\lambda_{P,avg}$ ) is marked with a solid vertical line. There is clearly some variation

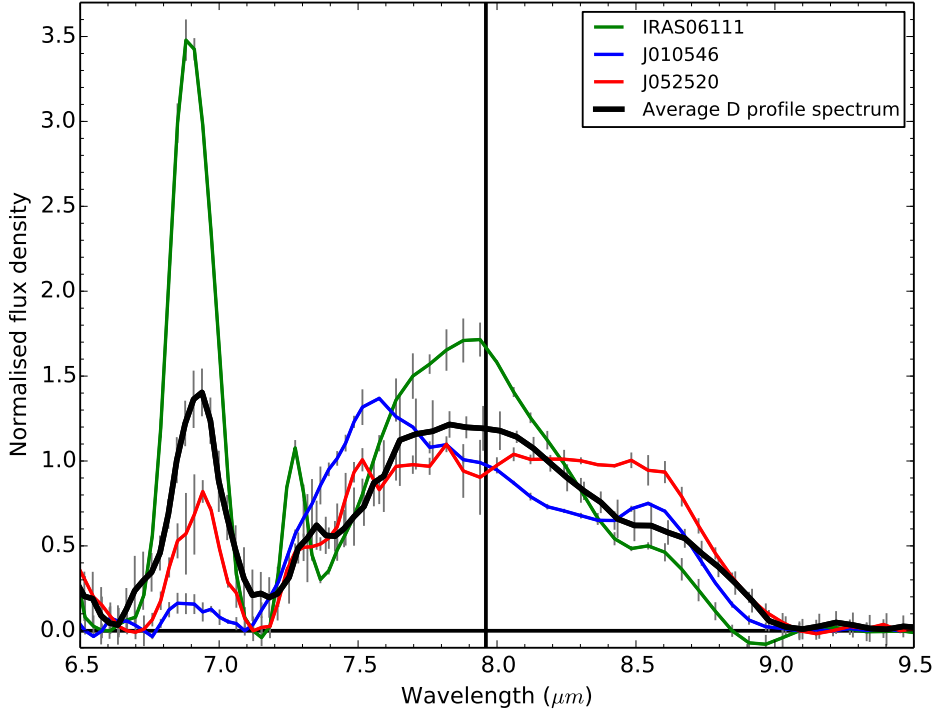


**Figure 6.4:** The average D class profile, with the three spectra which vary the most compared to the average overplotted. The vertical line marks the average peak wavelength of the 7.7  $\mu\text{m}$  complex. The spectra are normalised to the flux of the 7.7  $\mu\text{m}$  complex.

in the shape and peak wavelength of the 7.7  $\mu\text{m}$  complex, though it is much less than that seen in class B spectra [47]. The average central wavelength of the 7.7  $\mu\text{m}$  is found to be  $\lambda_{P,avg} = 7.96 \pm 0.09 \mu\text{m}$ . The large standard deviation is mainly caused by two outliers, NGC1978WBT2665 and IRAS 05063-6908, with  $\lambda_P = 7.79$  and  $8.14 \mu\text{m}$  respectively. For the other class D sources the 7.7  $\mu\text{m}$  complex peaks between 7.9 and 8.0  $\mu\text{m}$ . All the sources in class D have a broadened 7.7  $\mu\text{m}$  complex, similar to class C sources, though it is not quite as redshifted. It also tends to have a weak feature or shoulder at 8.6  $\mu\text{m}$ , which is completely washed out in C class sources [47]. The peak positions of the 6.2, 6.9, and 11.2  $\mu\text{m}$  features do not seem to vary much across the class, but the strengths do. Furthermore, all 11 D class sources exhibit emission at 6.9  $\mu\text{m}$ . This feature is discussed in more detail in section 6.4.2.

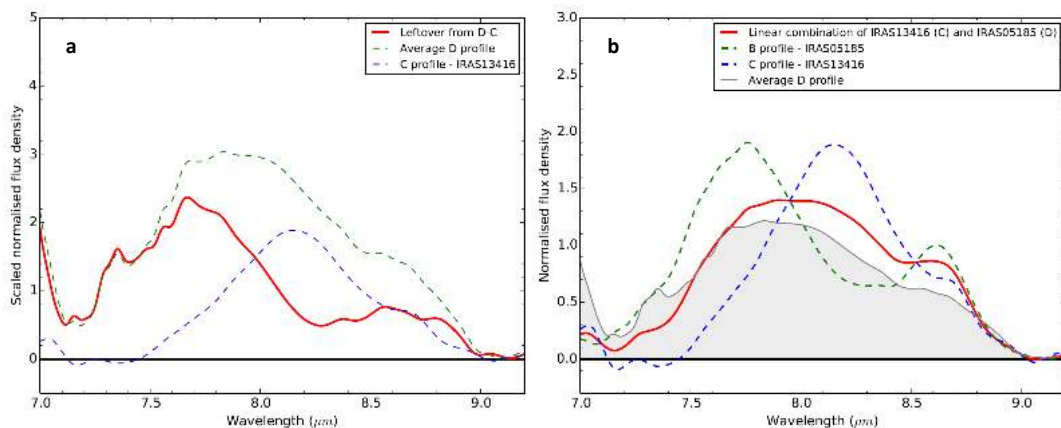


**Figure 6.5:** (a) the green dashed curve represents the average D class spectrum and the blue dashed curve the C class spectrum of IRAS13416, both normalised to the flux of the  $7.7 \mu\text{m}$  feature and scaled. The solid red curve is the result of subtracting a C class spectrum from the average D class spectrum, and bears a strong resemblance to a D class spectrum. (b) The dashed curves represent a C and B class spectrum respectively, both normalised to the flux of the  $7.7 \mu\text{m}$  complex, and the solid red curve is the linear combination of the two. The average D profile spectrum is filled in in grey.

Next the possibility of an evolution between the PAH classes is investigated, by studying the relation between B, C, and D class profiles. The results are shown in Fig. 6.5. First a C class spectrum is subtracted from the average D class spectrum (Fig 6.5(a)), and the result very closely resembles the profile of a B class spectrum. Then in Fig. 6.5(b) the linear combination of a B and C class spectrum is shown to be very similar to the average D class spectrum. This suggests that class D fits in between classes B and C in an evolutionary sequence.

### 6.4.2 Band Profiles of the Aliphatic Features

Of the 63 sources in the sample, 34 (54.0%) show emission at one or both aliphatics features at  $6.9$  and  $7.25 \mu\text{m}$  features. These sources are listed in Table 6.2, along with fluxes and peak positions of the relevant PAH features.

There are 31 sources (49.2%) in the sample exhibiting B emission at  $6.9 \mu\text{m}$ .

Table 6.2: Intensities and Central Wavelengths of sources with aliphatic emission

Source	$\Phi \left(\frac{W}{m^2}\right)$	$\lambda_c (\mu\text{m})$	$\Phi \left(\frac{W}{m^2}\right)$	class						
	$6.9 \mu\text{m}$	$6.9 \mu\text{m}$	$7.25 \mu\text{m}$	$7.25 \mu\text{m}$	$6.2 \mu\text{m}$	$7.7 \mu\text{m}$	$7.7 \mu\text{m}$	$7.7 \mu\text{m}$	$11.2 \mu\text{m}$	
HD 34282	$5.01 \times 10^{-14}$	6.89	$3.83 \times 10^{-14}$	7.25	$2.05 \times 10^{-12}$	$4.97 \times 10^{-12}$	$4.97 \times 10^{-12}$	7.87	$4.71 \times 10^{-13}$	B
HD 135344	$1.20 \times 10^{-13}$	6.86	$5.70 \times 10^{-14}$	7.27	$7.06 \times 10^{-13}$	$8.31 \times 10^{-13}$	$8.31 \times 10^{-13}$	7.96	$2.41 \times 10^{-13}$	B
HD 139614	$8.91 \times 10^{-14}$	6.85	-	-	$1.42 \times 10^{-12}$	$2.47 \times 10^{-12}$	$2.47 \times 10^{-12}$	7.99	$5.01 \times 10^{-13}$	B
HD 169142	$1.60 \times 10^{-13}$	6.97	-	-	$5.09 \times 10^{-12}$	$1.13 \times 10^{-11}$	$1.13 \times 10^{-11}$	7.91	$1.87 \times 10^{-12}$	B
IRAS f05110-6616	$3.92 \times 10^{-16}$	6.90	$7.86 \times 10^{-17}$	7.28	$2.94 \times 10^{-16}$	$1.06 \times 10^{-15}$	$1.06 \times 10^{-15}$	7.95	$6.83 \times 10^{-16}$	D
SMP LMC 075	$1.32 \times 10^{-17}$	6.85	-	-	$7.78 \times 10^{-16}$	$1.60 \times 10^{-15}$	$1.60 \times 10^{-15}$	7.84	$6.49 \times 10^{-16}$	B
IRAS 14429-4539	$3.75 \times 10^{-15}$	6.91	-	-	$6.93 \times 10^{-14}$	$1.44 \times 10^{-13}$	$1.44 \times 10^{-13}$	7.94	$2.44 \times 10^{-14}$	B
IRAS 15482-5741	$1.33 \times 10^{-16}$	6.90	-	-	$8.27 \times 10^{-16}$	$2.73 \times 10^{-15}$	$2.73 \times 10^{-15}$	8.01	$7.39 \times 10^{-16}$	D
IRAS 05413-6934/Cluster035	$1.13 \times 10^{-16}$	6.86	$4.49 \times 10^{-17}$	7.12	$5.27 \times 10^{-14}$	$6.32 \times 10^{-16}$	$6.32 \times 10^{-16}$	7.97	$2.39 \times 10^{-16}$	D
IRAS 00350-7436	$1.91 \times 10^{-17}$	6.95	$4.63 \times 10^{-17}$	7.24	$5.99 \times 10^{-16}$	$1.48 \times 10^{-15}$	$1.48 \times 10^{-15}$	7.80	$1.67 \times 10^{-16}$	D
IRAS 05063-6908	$3.25 \times 10^{-17}$	6.92	-	-	$1.15 \times 10^{-16}$	$1.51 \times 10^{-16}$	$1.51 \times 10^{-16}$	8.14	$2.71 \times 10^{-16}$	D
IRAS 05092-7121	$7.36 \times 10^{-17}$	6.89	-	-	$1.07 \times 10^{-15}$	$1.90 \times 10^{-15}$	$1.90 \times 10^{-15}$	7.80	$6.37 \times 10^{-16}$	B
IRAS 05186-6806	$2.07 \times 10^{-16}$	6.95	-	-	$2.13 \times 10^{-15}$	$5.06 \times 10^{-15}$	$5.06 \times 10^{-15}$	7.80	$1.38 \times 10^{-15}$	B
IRAS 05361-7121	$7.63 \times 10^{-17}$	6.92	-	-	$1.44 \times 10^{-15}$	$3.34 \times 10^{-15}$	$3.34 \times 10^{-15}$	7.81	$1.05 \times 10^{-15}$	B
IRAS 05588-6944	$1.22 \times 10^{-17}$	6.92	-	-	$1.28 \times 10^{-15}$	$2.44 \times 10^{-15}$	$2.44 \times 10^{-15}$	7.80	$1.32 \times 10^{-15}$	B
IRAS 06111-7023	$4.51 \times 10^{-16}$	6.91	$5.92 \times 10^{-17}$	7.27	$5.88 \times 10^{-16}$	$9.68 \times 10^{-16}$	$9.68 \times 10^{-16}$	7.91	$8.92 \times 10^{-16}$	D
IRAS f05192-7008	$5.36 \times 10^{-17}$	6.95	-	-	$4.26 \times 10^{-16}$	$8.10 \times 10^{-16}$	$8.10 \times 10^{-16}$	7.90	$6.20 \times 10^{-16}$	B
J00444111-7321361	$1.53 \times 10^{-16}$	6.89	$2.55 \times 10^{-17}$	7.28	$1.86 \times 10^{-16}$	$5.08 \times 10^{-16}$	$5.08 \times 10^{-16}$	7.91	$2.75 \times 10^{-16}$	D
J01054645-7147053	$1.93 \times 10^{-17}$	6.90	-	-	$2.22 \times 10^{-16}$	$8.37 \times 10^{-16}$	$8.37 \times 10^{-16}$	7.87	$1.52 \times 10^{-16}$	D
J05204385-6923403	$3.36 \times 10^{-17}$	6.90	-	-	$9.41 \times 10^{-17}$	$2.42 \times 10^{-16}$	$2.42 \times 10^{-16}$	7.98	$1.35 \times 10^{-16}$	D
IRAS z05259-7052/1052520	$3.35 \times 10^{-17}$	6.93	-	-	$1.19 \times 10^{-16}$	$3.13 \times 10^{-16}$	$3.13 \times 10^{-16}$	8.08	$2.91 \times 10^{-16}$	D
MSX SMC 029	-	-	$9.92 \times 10^{-18}$	7.30	$1.08 \times 10^{-16}$	$1.27 \times 10^{-16}$	$1.27 \times 10^{-16}$	7.93	$8.28 \times 10^{-17}$	B
NGC 1978 WBT 2665	$4.22 \times 10^{-16}$	6.92	-	-	$2.78 \times 10^{-16}$	$1.43 \times 10^{-15}$	$1.43 \times 10^{-15}$	7.79	$5.30 \times 10^{-16}$	D
IRAS 05073-6752/1050713	$1.70 \times 10^{-16}$	6.90	-	-	$3.03 \times 10^{-16}$	$4.90 \times 10^{-16}$	$4.90 \times 10^{-16}$	7.93	$4.69 \times 10^{-16}$	D
SMP LMC 058	-	-	$1.06 \times 10^{-17}$	7.17	$3.70 \times 10^{-16}$	$6.82 \times 10^{-16}$	$6.82 \times 10^{-16}$	7.87	$3.10 \times 10^{-17}$	B
SMP LMC 076	$1.23 \times 10^{-17}$	6.95	-	-	$1.03 \times 10^{-16}$	$1.51 \times 10^{-16}$	$1.51 \times 10^{-16}$	7.79	$8.36 \times 10^{-17}$	B
SMP SMC 001	$7.55 \times 10^{-18}$	7.00	$5.85 \times 10^{-18}$	7.15	$2.47 \times 10^{-16}$	$2.70 \times 10^{-16}$	$2.70 \times 10^{-16}$	7.75	$6.02 \times 10^{-17}$	B
SMP SMC 006	$9.81 \times 10^{-18}$	6.92	-	-	$2.40 \times 10^{-16}$	$3.81 \times 10^{-16}$	$3.81 \times 10^{-16}$	7.77	$2.29 \times 10^{-16}$	B
SMP SMC 011	$4.87 \times 10^{-17}$	6.90	-	-	$6.98 \times 10^{-16}$	$9.28 \times 10^{-16}$	$9.28 \times 10^{-16}$	7.67	$4.18 \times 10^{-16}$	A
IRAS I7047	$3.60 \times 10^{-14}$	6.89	-	-	$5.36 \times 10^{-13}$	$9.94 \times 10^{-13}$	$9.94 \times 10^{-13}$	7.85	$2.38 \times 10^{-13}$	B
IRAS I7347	$4.38 \times 10^{-15}$	6.95	-	-	$4.63 \times 10^{-14}$	$1.19 \times 10^{-13}$	$1.19 \times 10^{-13}$	7.95	$2.47 \times 10^{-14}$	B
XX-Ophiucus	-	-	$3.49 \times 10^{-15}$	7.23	$5.77 \times 10^{-14}$	$7.41 \times 10^{-14}$	$7.41 \times 10^{-14}$	7.79	$1.34 \times 10^{-14}$	B
IRAS 05341+0852	$7.57 \times 10^{-15}$	6.87	-	-	$1.33 \times 10^{-14}$	$5.12 \times 10^{-17}$	$5.12 \times 10^{-17}$	-	$1.42 \times 10^{-14}$	-
SMP SMC 020	$1.37 \times 10^{-17}$	6.85	-	-	$5.42 \times 10^{-17}$	$9.71 \times 10^{-17}$	$9.71 \times 10^{-17}$	7.63	$6.35 \times 10^{-18}$	AB

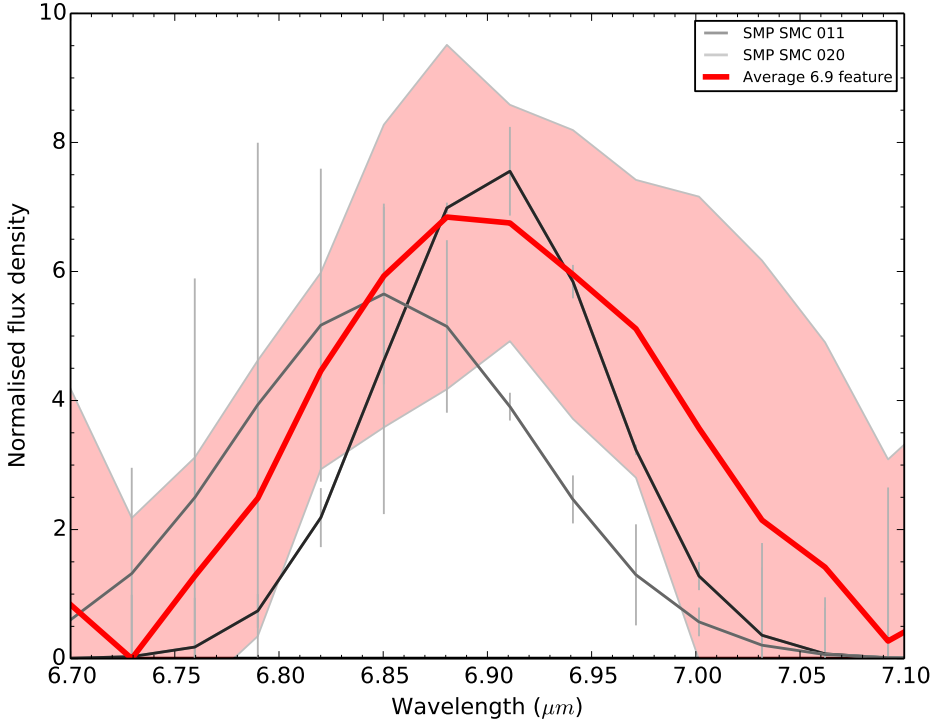


**Figure 6.6:** The average 6.9  $\mu\text{m}$  band profile, based on 31 detections, with the 6.9  $\mu\text{m}$  bands from A class sources shown. The shaded region marks the standard deviation.

The peak wavelength of the 6.9  $\mu\text{m}$  feature seems to vary continuously from 6.80 to 6.95  $\mu\text{m}$  across the sample, with an average  $\lambda_{P,avg} = 6.91 \pm 0.05 \mu\text{m}$ . This picture changes however, if we split the whole sample into subsamples according to their PAH class.

In Fig. 6.6 the average profile of the 6.9  $\mu\text{m}$  feature is plotted along with the 6.9  $\mu\text{m}$  features from the class A sources in the sample. The shaded region around the average profile marks the standard deviation. There is little variation between the two features, and though they peak at a slightly shorter wavelength than that of the average, there is not much difference.

The difference between the peak position of the 6.9  $\mu\text{m}$  features is much greater in B class sources, as shown in Fig. 6.7, where the average band profile is plotted with its standard deviation, along with a representative sample of 6.9  $\mu\text{m}$  features from B class sources. In this class the peak wavelength of the feature varies continuously across the range mentioned

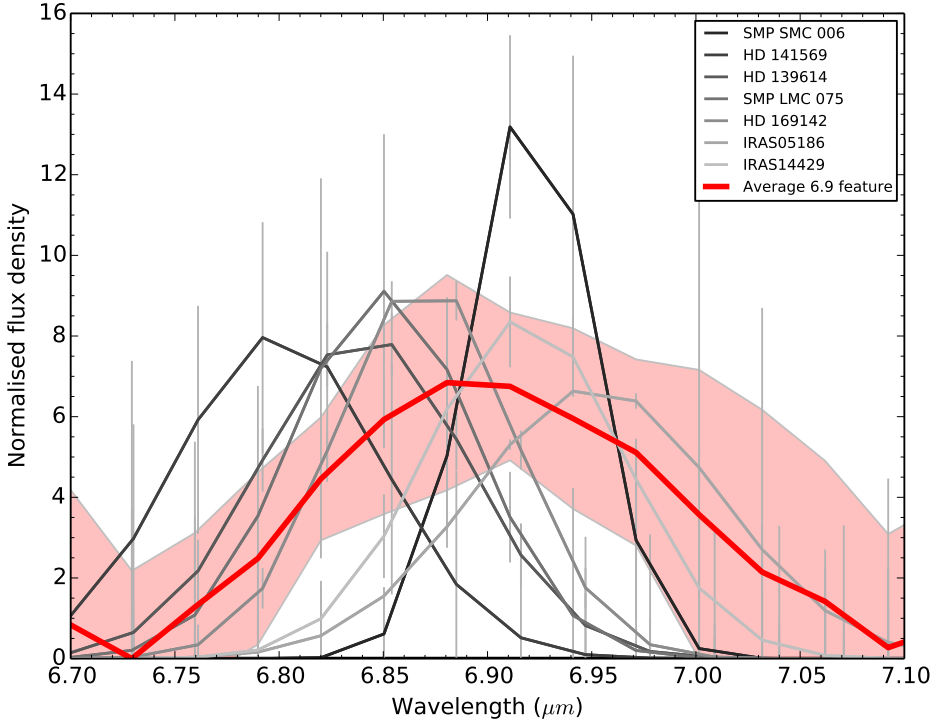


**Figure 6.7:** The average 6.9  $\mu\text{m}$  band profile, based on 31 detections, with a representative sample of the 6.9  $\mu\text{m}$  bands from B class sources shown. The shaded region marks the standard deviation.

above. This is not unexpected, as the same is true for most other PAH features in B class spectra [47, 58].

In D class sources there is little variation in peak wavelength of the 6.9  $\mu\text{m}$  feature from that of the average. This is shown in Fig. 6.8, where the 6.9  $\mu\text{m}$  features from the D class sources are plotted along with the average profile. The average peak wavelength of the D class 6.9  $\mu\text{m}$  features is  $6.90 \pm 0.02 \mu\text{m}$ , so very close to that of the average, but with a much smaller standard deviation.

Furthermore, all D class sources exhibit emission at 6.9  $\mu\text{m}$  as previously noted by Matsuura et al. [59] and Sloan et al. [13]. While its peak position does not vary greatly across the sources, its strength does, and is observed to be anywhere from 2 to 150 % of the strength of the 6.2  $\mu\text{m}$  feature. This makes the class D 6.9  $\mu\text{m}$  feature much stronger than those observed in other PAH classes [13], and is stronger than expected for minimally hydrogenated

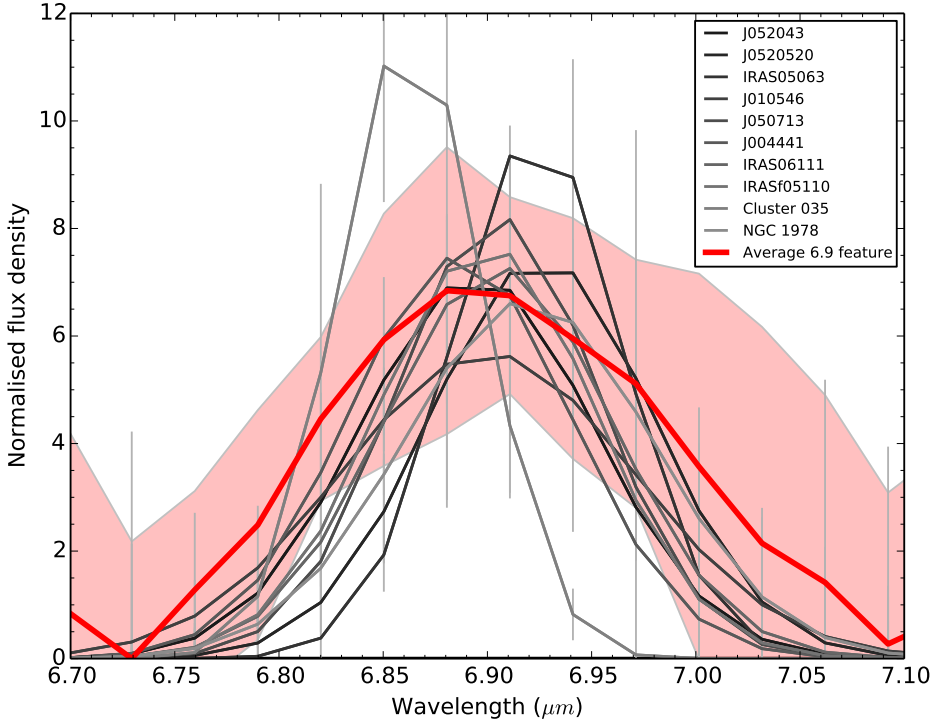


**Figure 6.8:** The average  $6.9 \mu\text{m}$  band profile, based on 31 detections, with the  $6.9 \mu\text{m}$  bands from D class sources shown. The shaded region marks the standard deviation.

PAH species [43].

The average profile of the  $7.25 \mu\text{m}$  feature, based on 11 detections, is shown in Fig. 6.9, with the shaded area representing its standard deviation. Plotted on top is a representative sample of  $7.25 \mu\text{m}$  profiles. The average profile is much broader than any of the features, reflecting a large variation across the sample of features. This may in part be due to our detection criteria, which required a signal-to-noise ratio (SNR) of more than  $3\sigma$ . While most of the detection of the  $6.9 \mu\text{m}$  feature were well above  $10\sigma$ , most of the  $7.25 \mu\text{m}$  features were detected at  $3\text{-}4\sigma$ . This feature thus appears to be significantly weaker than its counterpart. The  $7.25 \mu\text{m}$  feature also sits on top of the blue wing of the  $7.7 \mu\text{m}$  complex, which needs to be removed prior to characterisation. All in all, this leads to large uncertainties and variation in the feature, and the central wavelength varies between the 11 features between  $7.14$  and  $7.30 \mu\text{m}$ . The average peak wavelength of the

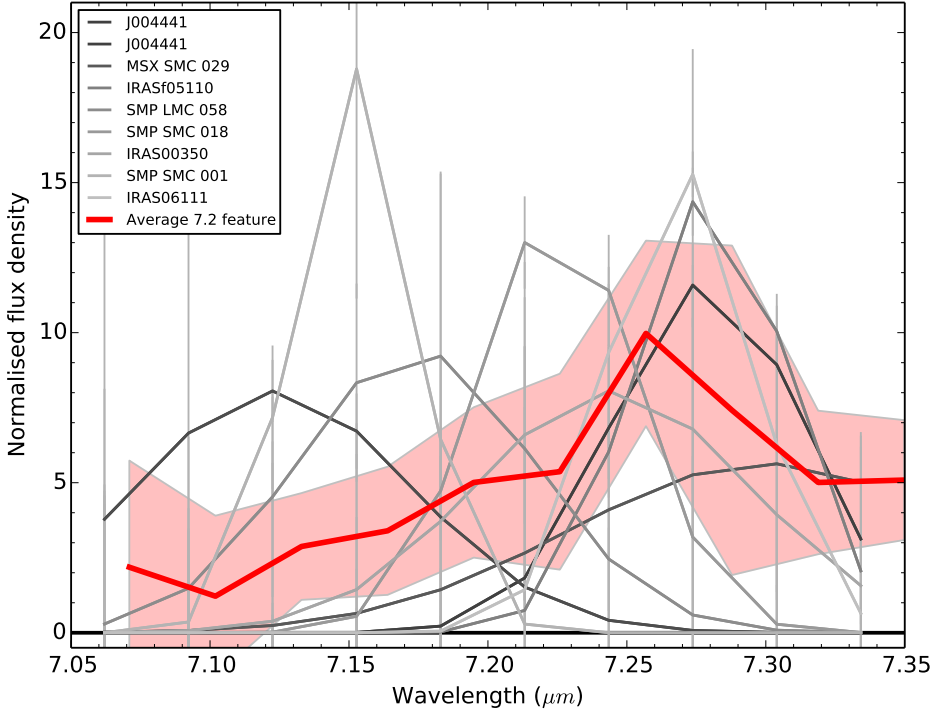


**Figure 6.9:** The average 7.25  $\mu\text{m}$  band profile, based on 11 detections, with a representative sample of the 7.25  $\mu\text{m}$  bands shown. The shaded region marks the standard deviation.

feature is  $7.23 \pm 0.06 \mu\text{m}$ . Four of the sources with emission at 7.25  $\mu\text{m}$  are class D, the rest class B. Only one of those sources does not also exhibit emission at 6.9  $\mu\text{m}$ .

### 6.4.3 Correlation Studies

In order to determine what type of material is responsible for the aliphatic features at 6.9 and 7.25  $\mu\text{m}$ , we examine all possible correlations between the features observed in the mid-IR PAH spectra.

We recover the previously observed correlation between the intensities of the 6.2 and 7.7  $\mu\text{m}$  features. This is shown in Fig. 6.10. The intensities have been normalised to the intensity of the 11.2  $\mu\text{m}$  feature, and the figure is colour coded by class, but the correlation is based on the full sample. A weighted Pearson correlation coefficient (wPcc) of 0.856 is found. The ob-

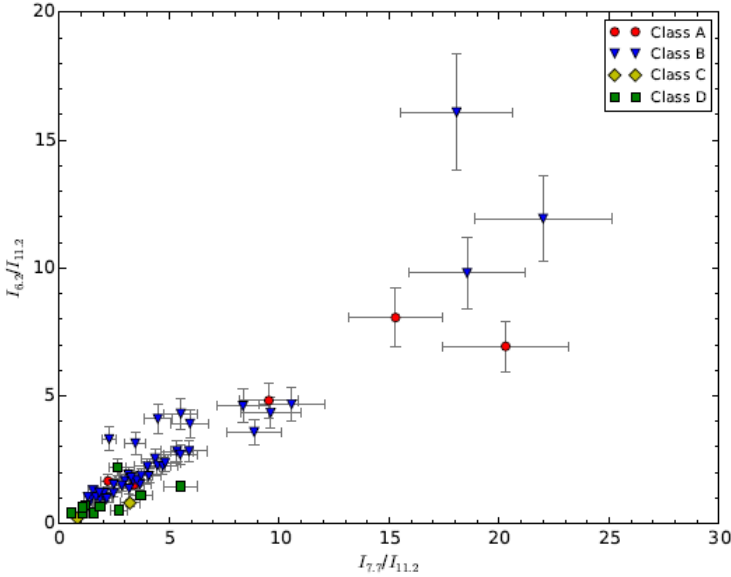


**Figure 6.10:** Correlation between the intensities of the 6.2 and 7.7  $\mu\text{m}$  features, normalised to the intensity of the 11.2  $\mu\text{m}$  feature. Weighted Pearson correlation coefficient: 0.856.

served range of the variations is larger than previously reported in literature, including a sample of galactic PDRs and HII regions, Magellanic HII regions, and galaxies of various types [167], a sample of galactic and Magellanic HII regions and PNe [148], and the RNe NGC7023 [55] and NGC2023 [165].

The sample contains ten sources which exhibit emission at both aliphatic features. Four of these are class D sources, and six a class B sources. Most of these have a very strong 6.9  $\mu\text{m}$  feature, with  $\text{SNR} > 10\sigma$ . The 7.25  $\mu\text{m}$  features tend to be much weaker, as discussed above, with  $\text{SNR} \approx 3 - 4\sigma$ . It is possible that a larger sample of the sources with 6.9  $\mu\text{m}$  feature also show some emission at 7.25  $\mu\text{m}$ . A further six sources in the sample has a detection of the 7.25  $\mu\text{m}$  feature at  $\text{SNR} = 2.5 - 3\sigma$ .

In sources where both aliphatic features are present, their intensities seem to be strongly correlated. This is shown in Fig. 6.11. The figure is correlated by PAH class and the line of best fit is drawn. The intensities have been normalised to that of the 6.2  $\mu\text{m}$  feature. We find a wPcc of 0.843. This would suggest that the two features, at least in sources where they are both present, arise from the same type of material.

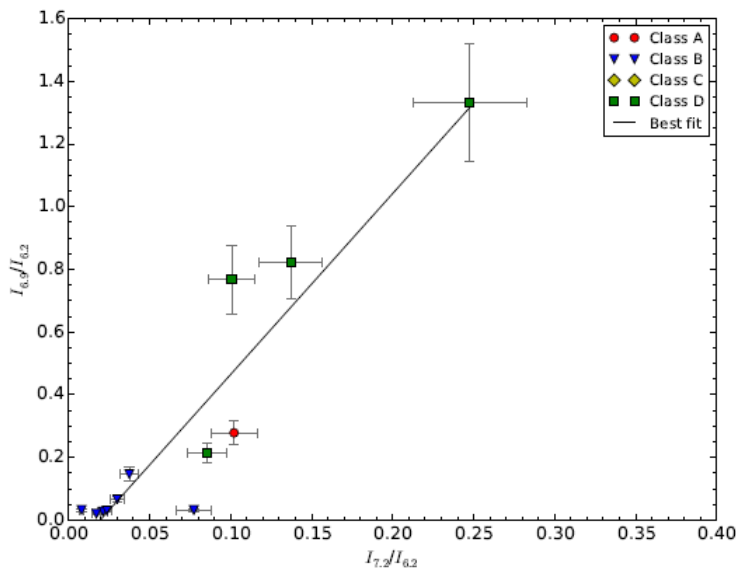


**Figure 6.11:** Correlation between the intensities of the 6.9 and 7.25  $\mu\text{m}$  features, normalised to the intensity of the 6.2  $\mu\text{m}$  feature. Weighted Pearson correlation coefficient: 0.843. A line of best fit is drawn to guide the eye.

In order to determine what type of aliphatic material gives rise to the features at 6.9 and 7.25  $\mu\text{m}$ , it is helpful to examine how they correlate with the aromatic PAH features. A strong correlation would suggest a relation to PAHs, either in the form of superhydrogenation or as aliphatic sidegroups, whereas no correlation would suggest that they arise from a separate type of molecules, e.g. hydrocarbon chains.

In Fig. 6.12 we show the correlation between the intensities of the 7.2 and 11.2  $\mu\text{m}$  features, normalised to the intensity of the 6.2  $\mu\text{m}$  feature. In this case a strong correlation is found with a wPcc of 0.882.

The case is different for the 6.9  $\mu\text{m}$  feature, where at first no correlation is found between its intensity and that of the 11.2  $\mu\text{m}$  feature (Fig. 6.13(a)). In this case, all sources with a 6.9  $\mu\text{m}$  feature were considered. If instead we limit the analysis to sources with both aliphatic features present (Fig. 6.13(b)), a strong correlation is found, with a wPcc of 0.917.

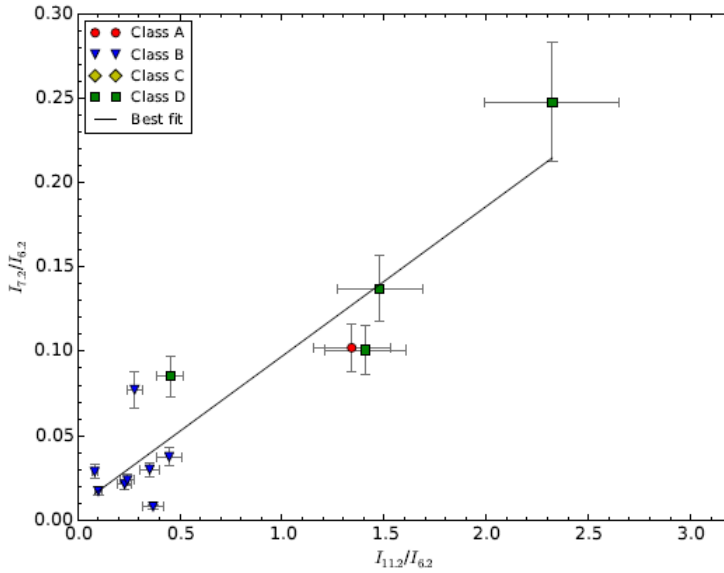


**Figure 6.12:** Correlation between the intensities of the 7.25 and 11.2  $\mu\text{m}$  features, normalised to the intensity of the 6.2  $\mu\text{m}$  feature. Weighted Pearson correlation coefficient: 0.882. A line of best fit is drawn to guide the eye.

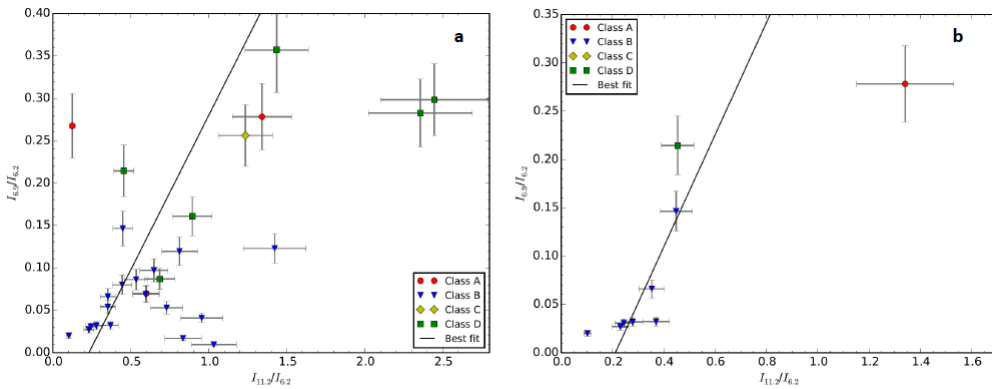


**Figure 6.13:** Correlation between the intensities of the 6.9 and 11.2  $\mu\text{m}$  features, normalised to the intensity of the 6.2  $\mu\text{m}$  feature. Lines of best fit are drawn to guide the eye. In (a) all 6.9  $\mu\text{m}$  detections are considered and no correlation is found. In (b) only sources with both a 6.9 and a 7.25  $\mu\text{m}$  feature are considered. In this case a strong correlation is observed, with a weighted Pearson correlation coefficient of 0.917.

### 6.4.4 Summary

Overall for this project the average profile of the D class sources was studied, the individual aliphatic features were analysed in detail across all PAH classes, and all possible correlations between aromatic and aliphatic features were investigated.

1. When looking at object type and PAH class a trend is apparent. Class A sources in our highly biased sample are solely PNe, while class B contains anything from YSOs over pAGB stars to PNe, class C contains only pAGB stars, while class D consists mainly of pAGB stars, but also contains some variable stars.
2. We find little variation in the peak positions of the various PAH features in class D objects in relation to the average profile, though the strength of the features vary widely. All D class sources exhibit emission at  $6.9 \mu\text{m}$ , and the feature tends to be quite strong, in some cases even stronger than the  $6.2 \mu\text{m}$  feature.
3. The average D class source seems to be a composite of C and B class profiles.
4. Thirty-four out of 63 sources exhibit either a  $6.9$  and/or a  $7.25 \mu\text{m}$  feature. Nineteen of those are class B, eleven class D, two class A and one class C. The last source with an aliphatic feature, IRAS 05341+0852 was observed with the FORCAST instrument on SOFIA, and could therefore not be strictly classified. It is however expected to exhibit a C class emission profile.
5. Thirty-one sources have a  $6.9\mu\text{m}$  feature. There is a large variation in the peak wavelength of the  $6.9 \mu\text{m}$  feature from the average, which arises almost entirely due to variation in B class sources. There is very little variation in the peak position of the  $6.9 \mu\text{m}$  feature in class D.
6. Eleven sources have a  $7.25 \mu\text{m}$  feature. Four are D class sources, the rest are B class sources. There is a large variation in shape and peak position of the feature, resulting in a very broad average feature profile, exhibiting almost a double peak structure. Data with better sensitivity will be required to perform better statistics on the feature.

7. We find strong correlations between the intensities of the 6.2 and 7.7  $\mu\text{m}$  features, normalised to the intensity of the 11.2  $\mu\text{m}$  feature, and between the intensities of 6.9 and 7.25, and 7.25 and 11.2  $\mu\text{m}$  features, normalised to the intensity of the 6.2  $\mu\text{m}$  feature.
8. When considering all sources with a 6.9  $\mu\text{m}$  feature we find no correlation between the intensity of that feature and that of the 11.2  $\mu\text{m}$  feature. The correlation improves significantly when only sources with both aliphatic features are considered.

## 6.5 Discussion

The last section described the results from our investigation of the variations in the band profiles of mid-IR PAH spectra with respect to astrophysical object type and PAH emission class, and with a specific interest in the aliphatic features at 6.9 and 7.25  $\mu\text{m}$ . In this section these results will be discussed in relation to previous observational and experimental work.

### 6.5.1 Chemical and Structural Evolution of the Emitting Population

It has previously been suggested that the PAH emission classes A, B, and C reflect a structural or chemical evolution in the emitting PAH population [168, 47, 12, 50, 51, 63, 64, 65, 60]. A clear evolution across objects exists, with class containing mostly interstellar objects (e.g. PDRs, RNe, HII regions, etc.) and only a few PNe, and class C consisting of pAGB stars, while class B encompasses everything in between. Adding class D seems to corroborate this, being made up of late-type stellar objects like pAGB stars, and some variable stars.

The suggested evolutionary sequence is  $C \rightarrow D \rightarrow B \rightarrow A \rightarrow B$ , or in terms of objects, from late-type stars (like pAGB stars) over PNe to ISM objects and from there to YSOs. In this scenario PAHs are believed to be formed in the circumstellar environments of pAGB stars. The mechanism is still not fully understood, but the most likely scenario involves a bottom-up process [15]. At this point the material is likely a mixture of aromatic and aliphatic compounds. As the star evolves the UV field gets stronger, and the carbonaceous material in the circumstellar environment is processed. UV photoprocessing preferentially destroys aliphatic bonds, thus increasing

the aromaticity of the carbonaceous material. By the time it is ejected into interstellar space, the material is almost entirely aromatic.

The results described in the previous section support this evolutionary scenario, with aliphatic emission exhibited in one (possible) class C source, all the class D sources,  $\simeq$  half of the class B sources and only a few class A sources in the sample. However, if this holds up, aliphatic material should become more important going from ISM sources to YSOs as well, moving from class A emission to class B emission. This may be explained by an active chemical equilibrium in the ISM, where hydrogen addition reactions and UV photodesorption are in competition with each other, and a balance is reached [62]. Our results show evidence of both aliphatic features, at 6.9 and 7.25  $\mu\text{m}$ , in all five YSOs in our sample, lending support to this theory.

### 6.5.2 Aliphatic Band Profiles and Correlations

Previously aliphatic features at 6.8 and 6.9  $\mu\text{m}$  have been discussed, though it has been somewhat unclear whether they are separate features or representations of the same feature [12, 13, 43]. We observe a feature around 6.9  $\mu\text{m}$  in 34 of our 63 sources, and its peak wavelength varies between 6.8 and 6.95  $\mu\text{m}$ , but features at 6.8 and 6.9  $\mu\text{m}$  are never observed together. The peak wavelength of the feature furthermore varies continuously across the range, suggesting there are not two separate features, but rather one feature, the position of which varies depending on the physical and chemical characteristics of the emitter. This is based also on the result that the variation in the 6.9  $\mu\text{m}$  feature is only seen in class B sources, just as it is mainly in this class variation is seen across other features as well.

For the ten sources with emission at both 6.9 and 7.25  $\mu\text{m}$  we find a strong correlation between their intensities. This suggests that the features may be related and arise in the same type of molecule. This is consistent with previous experiments, in which both bands appeared in the IR spectra of superhydrogenated PAHs [43].

We only observe a 7.25  $\mu\text{m}$  feature in 29% of the sources in which a 6.9  $\mu\text{m}$  feature is present. This may in part be because the 7.25  $\mu\text{m}$  feature is inherently weak [43], and it is possible that it is present in more sources, but not at a high enough SNR to be detected. Including detections of the feature with SNR  $\simeq 2.5 - 3\sigma$  in our sample would bring the total number

of 7.25  $\mu\text{m}$  detections up to 17, and almost half of the sources in which a 6.9  $\mu\text{m}$  feature is observed.

The 6.9  $\mu\text{m}$  feature is also known to arise in many different types of aliphatic material [43]. It is possible that the 7-25  $\mu\text{m}$  feature is more specific to one type of molecule.

### 6.5.3 Superhydrogenated PAHs and Their Role in $\text{H}_2$ Formation

To determine whether either of the aliphatic bands can be used as a tracer for superhydrogenated PAHs their correlation with aromatic PAH features are investigated. A strong correlation would suggest the features are a good tracer for superhydrogenated PAHs. Sandford et al. [43] discussed both the 6.9 and the 7.25  $\mu\text{m}$  as tracers of populations of superhydrogenated PAHs, and suggested using the 6.9  $\mu\text{m}$  feature, as it is much stronger, and therefore more likely to be detected, and easier to decompose in such a way as to derive population densities and degrees of hydrogenation of the emitting population.

However, as no correlation is found between the 6.9  $\mu\text{m}$  feature and any aromatic PAH features when all detections of the 6.9  $\mu\text{m}$  feature were considered, it is unlikely that feature on its own makes a good tracer of superhydrogenated PAHs.

There is a strong correlation between the 7.25  $\mu\text{m}$  aliphatic feature and the 11.2  $\mu\text{m}$  feature, attributed to neutral PAHs [169, 160]. The 7.25  $\mu\text{m}$  feature is therefore more likely to trace a population of superhydrogenated neutral PAHs than the 6.9  $\mu\text{m}$  feature. Unfortunately, due to its inherent weakness, it is not a great feature to use in trying to determine any quantitative information about the emitting population, like for example the degree of hydrogenation.

A correlation is found however, between the 6.9 and the 11.2  $\mu\text{m}$  features in sources where both the aliphatic features are present, and it is possible that the 6.9  $\mu\text{m}$  feature in those sources can be used to derive quantitative information about an emitting population of superhydrogenated PAHs.

# Chapter 7

## Summary and Outlook

*I know not all that may be coming, but be it  
what it will, I'll go to it laughing.*

— Herman Melville, *Moby Dick*

The results from three main projects have been presented in this thesis. First an experimental study on the interaction between PAHs (specifically coronene) and hydrogen isotopes at a temperature of  $\simeq 1000$  K was presented, followed by an experimental study on the growth and deuteration of fullerenes (specifically  $C_{60}$ ) on HOPG and gold. Lastly, astronomical spectra of a large sample of circumstellar environments of evolved and young stars were investigated for evidence of the presence of superhydrogenated PAHs. These projects were all performed with the aim of determining and understanding the interaction between large carbon-based molecules in the ISM and atomic hydrogen species.

### 7.1 Polycyclic Aromatic Hydrocarbon Experiments

The primary technique used to study the interaction between PAHs, and hydrogen and deuterium is TPD. Coronene molecules are deposited on a graphite surface and exposed to a beam of H or D atoms at 1000 K for varying lengths of time. After atom exposure the whole system is heated in a controlled manner, and the desorption products are measured with a mass spectrometer.

It is possible to obtain high degrees of superdeuteration and -hydrogenation, even with atoms at low temperatures, and superhydrogenated molecules especially seem to exhibit stable configurations. The cross section for addition of the first atom was found for both hydrogen and deuterium, and was found to be significantly larger for deuterium, although it should be noted that the fit to the data was not as good as for hydrogen. Furthermore, the binding energy of the superhydrogenated and -deuterated species to the HOPG surface was investigated and compared to previous results where the deuteration was done with hot atoms. For low deuteration degrees the binding energies were observed to decrease rapidly for both data sets. However at higher degrees of deuteration the binding energies for the low T data level off while for the high T data they keep decreasing, only to rise again. This suggest that, at least for higher deuteration states, different configurations are obtained depending on the temperature of the deuterium atom beam. No isotope effect was found in the binding energies to HOPG.

### 7.1.1 Outlook

Owing to several issues with the eperimental setup over the last few years, data collection has been slow, and most of the useful data was only obtained close to the submission deadline of this thesis. As a result, some of the analysis which is being done in collaboration with colleagues outside this institute is still ongoing, specifically the DFT calculations of the stable structures of superhydrogenated coronene, and the kMC simulations of the addition and abstraction cross sections of hydrogen and deuterium to coronene .

#### DFT of Stable Hydrogenation Configurations

DFT calculations to investigate the stable configurations of superhydrogenated coronene are being done by Rocco Martinazzo from Milan. These calculations will determine at which sites hydrogen is added to coronene, and which route to superhydrogenation is preferred. It will be possible to determine any addition and abstraction barriers for various configurations, and will give an insight into what a superhydrogenated coronene molecule looks like. It is also possible to calculate the binding energies to HOPG for the different configurations, similar to [83], but with the advantage of knowing which mass configurations are of most interest. These can then be compared to experiments.

### **kMC simulations of addition and abstraction cross sections**

In order to determine quantitatively the role of PAHs in  $H_2$  formation in the ISM, it is necessary to know the cross sections of addition and abstraction of hydrogen on PAHs. While it is possible to determine the addition cross section for the first hydrogen atom directly from experiment, this is not the case for any of the subsequent addition and/or abstraction reactions. The simple kinetic simulations performed by Skov et al. [82] are not sufficiently sophisticated to reproduce the mass distribution of either superdeuterated or superhydrogenated coronene when the atom beam temperature is low, as it lacks site specificity, and therefore cannot take any potential barriers into account.

In order to extract the addition and abstraction cross sections for hydrogen and deuterium on coronene site specific kinetic Monte Carlo simulations are being developed in collaboration with Dr. Herma Cuppen in Nijmegen. These simulations can distinguish between edge and centre sites, and will therefore be able to take certain potential barriers into account.

Knowing the addition and abstraction cross sections pertaining to different hydrogenation sites will allow for determining the  $H_2$  formation rate from abstraction reactions on PAHs in different parts of the ISM, assuming a certain degree of hydrogenation. This can be used to determine the degree of hydrogenation of PAHs required to obtain the necessary formation rate in the different regions of the ISM, which can in turn be compared to observations to determine whether it is feasible. It would also be interesting to study potential isotope effects in these cross sections, both through theoretical simulations and further experiments, to determine whether the difference in addition cross section described in Chapter 4. is a real result, or arises because the exponential function is not a good fit to the data, and cannot be applied.

### **Low Temperature Hydrogenation**

At 1000 K the atoms are still at a higher temperature than is applicable in the regions of the ISM where PAHs are interesting as possible catalysts for  $H_2$  formation. Since a difference is seen between the results using atoms at 2300 K and 1000 K, it is likely that the temperature of the atoms is very important in these reactions, and as a result it is necessary to study the reactions at the temperatures relevant in the galaxy. To that purpose a new

cooling nozzle has been designed which is expected to cool down the atoms to between 300 and 500 K. The aim here is to further probe the barriers for addition of hydrogen to PAHs and to determine what degree of superhydrogenation can possibly be reached in the regions of the galaxy where these reactions might be important.

The kinetic Monte Carlo simulations will have to be repeated to fit the low temperature data, in order to determine whether the rates of addition and abstraction are temperature dependent. From this it will be possible to determine in which temperature range PAHs might be efficient catalysts for H<sub>2</sub> formation.

There are also plenty of opportunities for further experiments involving the interaction between hydrogen isotopes and PAHs. The investigations of stable mass configurations could be extended to deuterium by using a deuterated version of coronene (C<sub>12</sub>D<sub>12</sub>) and a deuterium atom beam. In this case only addition reactions would result in a mass change of the molecule, and it would be possible to investigate whether the same configurations result as for hydrogen.

Another option, to further study abstraction reactions would be to deuterate perhydrocoronene (C<sub>12</sub>H<sub>36</sub>), the fully superhydrogenated coronene analog). In this case only abstraction reactions would result in a mass change, and it would be possible to investigate these in greater detail. Another interesting experiment would be to look at abstraction and dissociation of PAHs with UV light.

## 7.2 Fullerene Experiments

A monolayer of C<sub>60</sub> has successfully been grown on an Au(111) surface and hydrogenated. The growth of the monolayer starts at the step edges of the gold surface, and once these are saturated, islands grow rapidly, eventually forming a full well ordered monolayer. Annealing to 420 K reduces the number of defects, and eliminates any possible multilayers.

The C<sub>60</sub> monolayer is easily hydrogenated, using a thermal cracker. After only a short exposure to the atomic beam a high degree of hydrogenation of the sample is achieved. Three or four different hydrogenation states are likely observed, and more than two thirds of the molecules are hydrogenated after 5 seconds of exposure. A high degree of hydrogenation is maintained,

even after annealing to 500 K.

### 7.2.1 Outlook

The first step to build on this project will be to UV irradiate the hydrogenated C<sub>60</sub> monolayer on Au(111). This can be done while scanning, and it should therefore be possible to detect any changes in real time. It would be useful to attempt this experiment at different degrees of hydrogenation, and different coverages of C<sub>60</sub>, *i.e.* less than a monolayer.

To ensure relevance for astrophysical environments, transferring the system to a HOPG surface and repeating the experiments is necessary.

It is also possible to investigate the system using different analysis techniques, *e.g.* TPD, which could be used to study the dissociation products expected from the UV irradiation. Theoretical studies might also be helpful in this case.

## 7.3 Astrophysical Observations

A large sample of mid-IR spectra of evolved and young stellar objects have been investigated for the presence of aliphatic bands at 6.9 and 7.25  $\mu\text{m}$ . In spectra where the features have been detected they were characterised according to peak position and PAH class, and correlations between their strengths and those of the aromatic PAH features were investigated.

6.9  $\mu\text{m}$  is an inherently stronger feature than 7.25  $\mu\text{m}$ , and is thus easier to characterise in astronomical spectra. If the 6.9  $\mu\text{m}$  feature was found to trace a population of superhydrogenated PAHs, it would be possible to use its characteristics to determine the degree of hydrogenation of the PAH population in the regions where it is present. Unfortunately, this is found not to be the case. The 6.9  $\mu\text{m}$  feature is present in many types of aliphatic molecules, and at the resolution of astronomical spectra it is not possible to distinguish what type of aliphatic material it arises in. And since no correlation was found with PAH features of aromatic nature, it is not possible to make a convincing argument that the 6.9  $\mu\text{m}$  feature is in general related to superhydrogenated PAHs.

Instead it seems that the 7.25  $\mu\text{m}$  feature does trace a population of PAHs with some aliphatic components, likely superhydrogenation. However that

feature is inherently weak, and does not lend itself easily to further characterisation of the emitting population.

### 7.3.1 Outlook

This project has focussed on the mid-IR PAH spectra, but an aliphatic feature is also present at  $3.4 \mu\text{m}$ . Extending the analysis to include the near-IR part of the spectrum for sources where this is available would shed light on how this feature arises. Studying the behaviour of the  $3.4 \mu\text{m}$  feature in relation to both aromatic features and other aliphatic features will help determine whether it is likely to trace a population of superhydrogenated PAHs.

To investigate whether a population of superhydrogenated PAHs contribute to the  $\text{H}_2$  formation rate in the ISM, it will be necessary to extend the study to include more interstellar objects, like PDRs, RNe, etc. These will mainly be class A sources, and it is likely that any aliphatic features will be very weak. This is another reason it would be helpful to have near-IR data included into the analysis, as the  $3.4 \mu\text{m}$  feature is generally stronger than the  $6.9$  and  $7.25 \mu\text{m}$  features [43], and would therefore be easier to detect.

Using experimental and theoretical spectra of superhydrogenated PAHs, and an estimation of the oscillator strengths of the aliphatic features in their vibrational spectra it should be possible to estimate the abundance and hydrogenation degree of superhydrogenated PAHs in astrophysical environments.

# Chapter 8

## Danish Summary - Dansk Resummé

*Det er ikke nogen dårlig egenskab ved en fortælling, at man kun forstår halvdelen af den.*

— Karen Blixen, *Drømmerne*

### 8.1 Sukkersøde Stjernetåger

Mennesker har alle dage forsøgt at besvare livets store spørgsmål. Før i tiden kom svarene fra myter og religion, i dag kommer svaret for manges vedkommende fra videnskaben. Et af de største spørgsmål vi som mennesker kan stille os selv er hvor vi kommer fra, hvordan livet opstod, og svaret er ikke simpelt.

Livets oprindelse er et puslespil med så mange brikker at det kan virke uoverskueligt overhovedet at begynde. Men det afholder ikke videnskabsfolk fra hele verden fra at forsøge. Et puslespil er som regel lettere at samle hvis man samler hjørner og kanter først. I livets tilblivelses puslespil kan hjørnebrikkerne groft sagt siges at være dannelsen af brintmolekyler ( $H_2$ ) i galaksen, og det er disse hjørnebrikker min PhD afhandling koncentrerer sig om.

Ved hjælp af eksperimenter i et vakuumkammer har vi fundet ud af at brint kan dannes katalytisk på en familie af store molekyler. De hedder PAH'er, er bygget op af kulstof og brint, og så findes de overalt i vores galakse.

Det er vigtigt at forstå hvordan brintmolekyler bliver dannet, for de er yderst nødvendige i skabelsen af den kemiske mangfoldighed vi ser i vores galakse, og uden dem kunne stjerner og planeter ikke dannes. I løbet af de seneste årtier har astronomer identificeret næsten 200 molekyler i forskellige stjerne-tåger, og molekylær brint indgår i dannelsen af langt de fleste af dem. Det gælder både helt simple molekyler, som vand og kuldioxid, og mere komplekse molekyler, som formaldehyd og simple sukkerarter. De sidst nævnte er byggesten i store biomolekyler som RNA og DNA, der danner grundlaget for alt liv som vi kender det. Tilstedeværelsen af molekylært brint i galaksens stjerne-tåger er altså helt nødvendig for at mange andre molekyler overhovedet kan dannes. Det har længe været et mysterium for forskere hvordan den brint, der skaber den kemiske mangfoldighed i galaksen, selv dannes.

## 8.2 Internetdating for Atomer

Brintmolekyler kan nemlig ikke dannes i simple kollisioner mellem atomer. Hvis to atomer støder sammen kan de ikke hænge sammen, for reaktionen udleder for meget energi. Det er her PAH-molekylerne kommer ind i billedet. Brintatomer kan nemlig sætte sig fast på overfladen af de store molekyler, og så reagere med hinanden der.

Man kan sammenligne denne proces, kaldet katalyse, med internetdating. To enlige brintatomer vil begge gerne have en partner, men for at finde sammen skal de bruge lidt hjælp. Så de laver en profil på et datingwebsite, i dette tilfælde et PAH-molekyle. Her møder de hinanden, danner par, og rejser videre ud i verdensrummet på molekyleform.

Opdagelsen af PAH-molekyler som katalysator for brintdannelse er ikke ubetydelig, for disse molekyler findes overalt i vores galakse. På jorden kender vi dem bedst som kræftfremkaldende partikler i udstødningsgas og den sorte skorpe der dannes på grillmad. I rummet dannes de bl.a. i supernovaeksplosioner. PAH'er er store molekyler, og derfor svære at slå i stykker, og de rejser efter eksplosionen videre gennem galaksens mange stjerne-tåger, hvor kemien foregår, og her kan de eksistere i mange millioner år.

Alle de ingredienser der indgår i processen for brintdannelse er altså til stede i de områder af galaksen hvor brintmolekyler findes, og det er næppe tilfældigt, så det er nærliggende at tro at dette er en vigtig kilde til dan-

nelsen af molekylær brint. I et forsøg på at bevise dette indledte jeg et samarbejde med en gruppe astronomer fra University of Western Ontario i Canada, for at lede efter tegn på tilstedeværelsen af PAH'er med ekstra brintatomer i dele af galaksen. Resultatet blev at vi har fundet komponenter i astronomiske spektra der tyder på at den type molekyler eksisterer, men der er stadig usikkerhed om hvorvidt de også kan skyldes en anden type molekyle.

Der er stadig mange brikker i livets puslespil vi mangler at finde eller placere korrekt, men med dette projekt får forskere et vigtigt fundament at arbejde videre på i forhold til hvordan livet i sin tid opstod i universet.



# Bibliography

- [1] T. Koupelis and K. F. Kuhn, *In Quest of the Universe*. Jones and Bartlett, 5 ed., 2006.
- [2] J. Christensen-Dalsgaard, *Lecture Notes on Stellar Structure and Evolution*. Department of Physics and Astronomy, Aarhus University, 2008.
- [3] C. Gall, J. Hjorth, and A. C. Andersen, “Production of dust by massive stars at high redshift,” *The Astronomy and Astrophysics Review*, vol. 19, no. 1, p. 43, 2011.
- [4] C. Gall, J. Hjorth, D. Watson, E. Dwek, J. R. Maund, O. Fox, G. Leloudas, D. Malesani, and A. C. Day-Jones, “Rapid formation of large dust grains in the luminous supernova sn 2010jl,” *arXiv preprint arXiv:1407.4447*, 2014.
- [5] A. Tielens, *The Physics and Chemistry of the Interstellar Medium*. Cambridge University Press, 2 ed., 2010.
- [6] J. M. Dickey and R. W. Garwood, “The mass spectrum of interstellar clouds,” *The Astrophysical Journal*, vol. 341, pp. 201–207, June 1989.
- [7] A. G. G. M. Tielens, “The molecular universe,” *Reviews of Modern Physics*, vol. 85, pp. 1021–1081, July 2013.
- [8] E. A. Bergin and M. Tafalla, “Cold dark clouds: the initial conditions for star formation,” *Annu. Rev. Astron. Astrophys.*, vol. 45, pp. 339–396, 2007.
- [9] “Molecules in space.”  
<https://www.astro.uni-koeln.de/cdms/molecules>. date accessed: July 1, 2017.

- [10] A. K. Leroy, A. Bolatto, C. Bot, C. W. Engelbracht, K. Gordon, F. P. Israel, M. Rubio, K. Sandstrom, and S. Stanimirović, “The Structure of a Low-metallicity Giant Molecular Cloud Complex,” *the Astrophysical Journal*, vol. 702, pp. 352–367, Sept. 2009.
- [11] M. Goto, S. Kwok, H. Takami, M. Hayashi, W. Gaessler, Y. Hayano, M. Iye, Y. Kamata, T. Kanzawa, N. Kobayashi, *et al.*, “Diffraction-limited 3  $\mu\text{m}$  spectroscopy of iras 04296+ 3429 and iras 05341+ 0852: Spatial extent of hydrocarbon dust emission and dust evolutionary sequencebased on data collected at subaru telescope, operated by the national astronomical observatory of japan.” *The Astrophysical Journal*, vol. 662, no. 1, p. 389, 2007.
- [12] G. Sloan, M. Jura, W. Duley, K. Kraemer, J. Bernard-Salas, W. Forrest, B. Sargent, A. Li, D. Barry, C. Bohac, *et al.*, “The unusual hydrocarbon emission from the early carbon star hd 100764: The connection between aromatics and aliphatics,” *The Astrophysical Journal*, vol. 664, no. 2, p. 1144, 2007.
- [13] G. Sloan, E. Lagadec, A. Zijlstra, K. Kraemer, A. Weis, M. Matsuura, K. Volk, E. Peeters, W. Duley, J. Cami, *et al.*, “Carbon-rich dust past the asymptotic giant branch: aliphatics, aromatics, and fullerenes in the magellanic clouds,” *The Astrophysical Journal*, vol. 791, no. 1, p. 28, 2014.
- [14] J. Cami, J. Bernard-Salas, E. Peeters, and S. E. Malek, “Detection of c60 and c70 in a young planetary nebula,” *Science*, vol. 329, no. 5996, pp. 1180–1182, 2010.
- [15] I. Cherchneff, “The formation of polycyclic aromatic hydrocarbons in evolved circumstellar environments,” *EAS publications series*, vol. 46, pp. 177–189, 2011.
- [16] T. P. Snow and A. N. Witt, “Interstellar Depletions Updated: Where All the Atoms Went,” *The Astrophysical Journal Letters*, vol. 468, p. L65, Sept. 1996.
- [17] E. L. Gibb, D. C. B. Whittet, W. A. Schutte, A. C. A. Boogert, J. E. Chiar, P. Ehrenfreund, P. A. Gerakines, J. V. Keane, A. G. G. M.

- Tielens, E. F. van Dishoeck, and O. Kerkhof, "An Inventory of Interstellar Ices toward the Embedded Protostar W33A," *The Astrophysical Journal*, vol. 536, pp. 347–356, June 2000.
- [18] E. Habart, F. Boulanger, L. Verstraete, G. P. des Forêts, E. Falgarone, and A. Abergel, "H<sub>2</sub> infrared line emission across the bright side of the  $\rho$  ophiuchi main cloud," *Astronomy & Astrophysics*, vol. 397, no. 2, pp. 623–634, 2003.
- [19] M. Jura, "Interstellar clouds containing optically thin H<sub>2</sub>," *The Astrophysical Journal*, vol. 197, pp. 575–580, May 1975.
- [20] V. Pirronello, C. Liu, L. Shen, and G. Vidali, "Laboratory Synthesis of Molecular Hydrogen on Surfaces of Astrophysical Interest," *The Astrophysical Journal Letters*, vol. 475, pp. L69–L72, Jan. 1997.
- [21] V. Pirronello, O. Biham, C. Liu, L. Shen, and G. Vidali, "Efficiency of Molecular Hydrogen Formation on Silicates," *The Astrophysical Journal Letters*, vol. 483, pp. L131–L134, July 1997.
- [22] H. B. Perets, A. Lederhendler, O. Biham, G. Vidali, L. Li, S. Swords, E. Congiu, J. Roser, G. Manicó, J. R. Brucato, and V. Pirronello, "Molecular Hydrogen Formation on Amorphous Silicates under Interstellar Conditions," *The Astrophysical Journal Letters*, vol. 661, pp. L163–L166, June 2007.
- [23] G. Vidali, L. Li, J. E. Roser, and R. Badman, "Catalytic activity of interstellar grains: Formation of molecular hydrogen on amorphous silicates," *Advances in Space Research*, vol. 43, pp. 1291–1298, Apr. 2009.
- [24] E. R. Latimer, F. Islam, and S. D. Price, "Studies of HD formed in excited vibrational states from atomic recombination on cold graphite surfaces," *Chemical Physics Letters*, vol. 455, pp. 174–177, Apr. 2008.
- [25] J. S. A. Perry and S. D. Price, "Detection of rovibrationally excited H<sub>2</sub> formed through the heterogeneous recombination of H atoms on a cold HOPG surface," *Astronomy and Astrophysics, Supplement*, vol. 285, pp. 769–776, 2003.

- [26] V. Pirronello, C. Liu, J. E. Roser, and G. Vidali, "Measurements of molecular hydrogen formation on carbonaceous grains," *Astronomy and Astrophysics*, vol. 344, pp. 681–686, Apr. 1999.
- [27] L. Hornekær, A. Baurichter, V. V. Petrunin, D. Field, and A. C. Luntz, "Importance of Surface Morphology in Interstellar H<sub>2</sub> Formation," *Science*, vol. 302, pp. 1943–1946, Dec. 2003.
- [28] L. Hornekær, A. Baurichter, V. V. Petrunin, A. C. Luntz, B. D. Kay, and A. Al-Halabi, "Influence of surface morphology on d 2 desorption kinetics from amorphous solid water," *The Journal of chemical physics*, vol. 122, no. 12, p. 124701, 2005.
- [29] G. Manico, G. Raguni, V. Pirronello, J. Roser, and G. Vidali, "Laboratory measurements of molecular hydrogen formation on amorphous water ice," *The Astrophysical Journal Letters*, vol. 548, no. 2, p. L253, 2001.
- [30] H. M. Cuppen and E. Herbst, "Monte Carlo simulations of H<sub>2</sub> formation on grains of varying surface roughness," *Monthly Notices to the Royal Astronomical Society*, vol. 361, pp. 565–576, Aug. 2005.
- [31] L. Hornekær, E. Rauls, W. Xu, Ž. Šljivančanin, R. Otero, I. Stensgaard, E. Lægsgaard, B. Hammer, and F. Besenbacher, "Clustering of Chemisorbed H(D) Atoms on the Graphite (0001) Surface due to Preferential Sticking," *Physical Review Letters*, vol. 97, p. 186102, Nov. 2006.
- [32] T. Zecho, A. Guttler, X. Sha, B. Jackson, and J. Kupperts, "Adsorption of hydrogen and deuterium atoms on the (0001) graphite surface," *Journal of Chemical Physics*, vol. 117, pp. 8486–8492, Nov. 2002.
- [33] X. Sha and B. Jackson, "First-principles study of the structural and energetic properties of h atoms on a graphite (0001) surface," *Surface Science*, vol. 496, no. 3, pp. 318–330, 2002.
- [34] E. Habart, F. Boulanger, L. Verstraete, C. Walmsley, and G. P. Des Forêts, "Some empirical estimates of the h<sub>2</sub> formation rate in photon-dominated regions," *Astronomy & Astrophysics*, vol. 414, no. 2, pp. 531–544, 2004.

- [35] A. G. Tielens, “Interstellar polycyclic aromatic hydrocarbon molecules\*,” *Annu. Rev. Astron. Astrophys.*, vol. 46, pp. 289–337, 2008.
- [36] R. F. Peter Atkins, *Molecular Quantum Mechanics*. Oxford University Press, 5 ed., 2011.
- [37] A. Leger and J. Puget, “Identification of the ‘unidentified’ ir emission features of interstellar dust?,” *Astronomy and Astrophysics*, vol. 137, pp. L5–L8, 1984.
- [38] L. Allamandola, A. Tielens, and J. Barker, “Interstellar polycyclic aromatic hydrocarbons—the infrared emission bands, the excitation/emission mechanism, and the astrophysical implications,” *The Astrophysical Journal Supplement Series*, vol. 71, pp. 733–775, 1989.
- [39] L. Allamandola, J. Bregman, S. Sandford, A. Tielens, F. Witteborn, D. Wooden, and D. Rank, “The discovery of a new infrared emission feature at 1905 wavenumbers (5.25 microns) in the spectrum of bd+30 deg 3639 and its relation to the polycyclic aromatic hydrocarbon model,” *The Astrophysical Journal*, vol. 345, pp. L59–L62, 1989.
- [40] C. Joblin and A. G. G. M. Tielens, “Pahs and the universe: A symposium to celebrate the 25th anniversary of the pah hypothesis,” in *EAS publications series*, vol. 46, 2011.
- [41] “Tb2 chemistry at tasis.”  
<http://wps.prenhall.com/wps/media/objects/3081/3155729/blb0905.html>.  
date accessed: July 21st, 2017.
- [42] M. P. Bernstein, S. A. Sandford, and L. J. Allamandola, “Hydrogenated polycyclic aromatic hydrocarbons and the 2940 and 2850 wavenumber (3.40 and 3.51 micron) infrared emission features,” *The Astrophysical Journal Letters*, vol. 472, no. 2, p. L127, 1996.
- [43] S. A. Sandford, M. P. Bernstein, and C. K. Materese, “The infrared spectra of polycyclic aromatic hydrocarbons with excess peripheral h atoms (h n-pahs) and their relation to the 3.4 and 6.9  $\mu\text{m}$  pah emission features,” *The Astrophysical Journal Supplement Series*, vol. 205, no. 1, p. 8, 2013.

- [44] K. Volk, B. J. Hrivnak, M. Matsuura, J. Bernard-Salas, R. Szczerba, G. Sloan, K. E. Kraemer, J. T. van Loon, F. Kemper, P. M. Woods, *et al.*, “Discovery and analysis of 21  $\mu\text{m}$  feature sources in the magellanic clouds,” *The Astrophysical Journal*, vol. 735, no. 2, p. 127, 2011.
- [45] C. Sagan, B. Khare, W. Thompson, G. McDonald, M. R. Wing, J. L. Bada, T. Vo-Dinh, and E. Arakawa, “Polycyclic aromatic hydrocarbons in the atmospheres of titan and jupiter,” *The Astrophysical Journal*, vol. 414, pp. 399–405, 1993.
- [46] E. Sciamma-O’Brien, C. L. Ricketts, and F. Salama, “The titan haze simulation experiment on cosmic: Probing titan’s atmospheric chemistry at low temperature,” *Icarus*, vol. 243, pp. 325–336, 2014.
- [47] E. Peeters, S. Hony, C. Van Kerckhoven, A. Tielens, L. Allamandola, D. Hudgins, and C. Bauschlicher, “The rich 6 to 9  $\mu\text{m}$  spectrum of interstellar pahas,” *Astronomy and Astrophysics*, vol. 390, no. 3, pp. 1089–1113, 2002.
- [48] M. Rapacioli, C. Joblin, and P. Boissel, “Spectroscopy of polycyclic aromatic hydrocarbons and very small grains in photodissociation regions,” *Astronomy & Astrophysics*, vol. 429, no. 1, pp. 193–204, 2005.
- [49] O. Berné, C. Joblin, Y. Deville, J. Smith, M. Rapacioli, J. Bernard, J. Thomas, W. Reach, and A. Abergel, “Analysis of the emission of very small dust particles from spitzer spectro-imagery data using blind signal separation methods,” *Astronomy & Astrophysics*, vol. 469, no. 2, pp. 575–586, 2007.
- [50] C. W. Bauschlicher Jr, E. Peeters, and L. J. Allamandola, “The infrared spectra of very large, compact, highly symmetric, polycyclic aromatic hydrocarbons (pahas),” *The Astrophysical Journal*, vol. 678, no. 1, p. 316, 2008.
- [51] C. W. Bauschlicher Jr, E. Peeters, and L. J. Allamandola, “the infrared spectra of very large irregular polycyclic aromatic hydrocarbons (pahas): Observational probes of astronomical pah geometry, size, and charge,” *The Astrophysical Journal*, vol. 697, no. 1, p. 311, 2009.
- [52] M. Rosenberg, O. Berné, C. Boersma, L. Allamandola, and A. M. Tielens, “Coupled blind signal separation and spectroscopic database

- fitting of the mid infrared pah features,” *Astronomy & Astrophysics*, vol. 532, p. A128, 2011.
- [53] A. Ricca, C. W. Bauschlicher Jr, C. Boersma, A. G. Tielens, and L. J. Allamandola, “The infrared spectroscopy of compact polycyclic aromatic hydrocarbons containing up to 384 carbons,” *The Astrophysical Journal*, vol. 754, no. 1, p. 75, 2012.
- [54] C. Boersma, J. Bregman, and L. Allamandola, “Properties of polycyclic aromatic hydrocarbons in the northwest photon dominated region of ngc 7023. i. pah size, charge, composition, and structure distribution,” *The Astrophysical Journal*, vol. 769, no. 2, p. 117, 2013.
- [55] C. Boersma, J. Bregman, and L. Allamandola, “Properties of polycyclic aromatic hydrocarbons in the northwest photon dominated region of ngc 7023. ii. traditional pah analysis using k-means as a visualization tool,” *The Astrophysical Journal*, vol. 795, no. 2, p. 110, 2014.
- [56] C. Boersma, J. Bregman, and L. Allamandola, “Properties of polycyclic aromatic hydrocarbons in the northwest photon dominated region of ngc 7023. iii. quantifying the traditional proxy for pah charge and assessing its role,” *The Astrophysical Journal*, vol. 806, no. 1, p. 121, 2015.
- [57] H. Andrews, C. Boersma, M. Werner, J. Livingston, L. Allamandola, and A. Tielens, “Pah emission at the bright locations of pdrs: the grandpah hypothesis,” *The Astrophysical Journal*, vol. 807, no. 1, p. 99, 2015.
- [58] B. Van Diedenhoven, E. Peeters, C. Van Kerckhoven, S. Hony, D. Hudgins, L. Allamandola, and A. Tielens, “The profiles of the 3-12 micron polycyclic aromatic hydrocarbon features based on observations with iso, an esa project with instruments funded by esa member states (especially the pi countries: France, germany, the netherlands, and the united kingdom) and with the participation of isas and nasa.,” *The Astrophysical Journal*, vol. 611, no. 2, p. 928, 2004.
- [59] M. Matsuura, J. Bernard-Salas, T. L. Evans, K. M. Volk, B. J. Hrivnak, G. C. Sloan, Y.-H. Chu, R. Gruendl, K. E. Kraemer, E. Peeters, *et al.*, “Spitzer space telescope spectra of post-agb stars in the large

- magellanic cloud–polycyclic aromatic hydrocarbons at low metallicities,” *Monthly Notices of the Royal Astronomical Society*, vol. 439, no. 2, pp. 1472–1493, 2014.
- [60] J. Cami, “Analyzing astronomical observations with the nasa ames pah database,” *EAS Publications Series*, vol. 46, pp. 117–122, 2011.
- [61] G. Sloan, L. Keller, W. Forrest, E. Leibensperger, B. Sargent, A. Li, J. Najita, D. Watson, B. Brandl, C. Chen, *et al.*, “Mid-infrared spectra of polycyclic aromatic hydrocarbon emission in herbig ae/be stars,” *The Astrophysical Journal*, vol. 632, no. 2, p. 956, 2005.
- [62] C. Boersma, J. Bouwman, F. Lahuis, C. Van Kerckhoven, A. Tielens, L. Waters, and T. Henning, “The characteristics of the ir emission features in the spectra of herbig ae stars: evidence for chemical evolution,” *Astronomy & Astrophysics*, vol. 484, no. 1, pp. 241–249, 2008.
- [63] L. D. Keller, G. Sloan, W. Forrest, S. Ayala, P. D’Alessio, S. Shah, N. Calvet, J. Najita, A. Li, L. Hartmann, *et al.*, “Pah emission from herbig ae/be stars,” *The Astrophysical Journal*, vol. 684, no. 1, p. 411, 2008.
- [64] T. Pino, E. Dartois, A.-T. Cao, Y. Carpentier, T. Chamail e, R. Vasquez, A. Jones, L. d’Hendecourt, and P. Br echnignac, “The 6.2  $\mu$  m band position in laboratory and astrophysical spectra: a tracer of the aliphatic to aromatic evolution of interstellar carbonaceous dust,” *Astronomy and Astrophysics*, vol. 490, no. 2, pp. 665–672, 2008.
- [65] B. Acke, J. Bouwman, A. Juh asz, T. Henning, M. Van den Ancker, G. Meeus, A. Tielens, and L. Waters, “Spitzer’s view on aromatic and aliphatic hydrocarbon emission in herbig ae stars,” *The Astrophysical Journal*, vol. 718, no. 1, p. 558, 2010.
- [66] D. J. S. P. A. Jensen, M. J. Shannon and E. Peeters, “Aliphatic features in mid-infrared polycyclic aromatic hydrocarbon spectra,” *Astronomy and Astrophysics*, 2017.
- [67] J. R. Barker, L. Allamandola, and A. Tielens, “Anharmonicity and the interstellar polycyclic aromatic hydrocarbon infrared emission spectrum,” *The Astrophysical Journal*, vol. 315, pp. L61–L65, 1987.

- [68] T. Geballe, A. Tielens, L. Allamandola, A. Moorhouse, and P. Brand, "Spatial variations of the 3 micron emission features within uv-excited nebulae-photochemical evolution of interstellar polycyclic aromatic hydrocarbons," *The Astrophysical Journal*, vol. 341, pp. 278–287, 1989.
- [69] C. Joblin, A. Tielens, L. Allamandola, and T. Geballe, "Spatial variation of the 3.29 and 3.40 micron emission bands within reflection nebulae and the photochemical evolution of methylated polycyclic aromatic hydrocarbons," *The Astrophysical Journal*, vol. 458, p. 610, 1996.
- [70] N. Hiyoshi, M. Osada, C. V. Rode, O. Sato, and M. Shirai, "Hydrogenation of benzothiophene-free naphthalene over charcoal-supported metal catalysts in supercritical carbon dioxide solvent," *Applied Catalysis A: General*, vol. 331, pp. 1–7, 2007.
- [71] M. J. Jacinto, O. H. Santos, R. Landers, P. K. Kiyohara, and L. M. Rossi, "On the catalytic hydrogenation of polycyclic aromatic hydrocarbons into less toxic compounds by a facile recoverable catalyst," *Applied Catalysis B: Environmental*, vol. 90, no. 3, pp. 688–692, 2009.
- [72] W. Liao, H.-W. Liu, H.-J. Chen, W.-Y. Chang, K.-H. Chiu, and C. M. Wai, "Catalytic hydrogenation rate of polycyclic aromatic hydrocarbons in supercritical carbon dioxide containing polymer-stabilized palladium nanoparticles," *Chemosphere*, vol. 82, no. 4, pp. 573–580, 2011.
- [73] B. Jørgensen, *Hydrogen interaction with carbonaceous materials*. PhD thesis, Aarhus University, 2011.
- [74] E. Rauls and L. Hornekær, "Catalyzed Routes to Molecular Hydrogen Formation and Hydrogen Addition Reactions on Neutral Polycyclic Aromatic Hydrocarbons under Interstellar Conditions," *The Astrophysical Journal*, vol. 679, pp. 531–536, May 2008.
- [75] J. A. Rasmussen, G. Henkelman, and B. Hammer, "Pyrene: Hydrogenation, hydrogen evolution, and  $\pi$ -band model," *Journal of Chemical Physics*, vol. 134, pp. 164703–164703, Apr. 2011.
- [76] R. M. Ferullo, N. J. Castellani, and P. G. Beelli, "Interaction of atomic hydrogen with anthracene and polyacene from density functional theory," *Chemical Physics Letters*, vol. 648, pp. 25–30, Mar. 2016.

- [77] J. A. Rasmussen, "Polycyclic aromatic hydrocarbons: trends for bonding hydrogen," *The Journal of Physical Chemistry A*, vol. 117, no. 20, pp. 4279–4285, 2013.
- [78] M. Bonfanti, S. Casolo, G. F. Tantardini, A. Ponti, and R. Martinazzo, "A few simple rules governing hydrogenation of graphene dots," *Journal of Chemical Physics*, vol. 135, pp. 164701–164701, Oct. 2011.
- [79] T. P. M. Goumans, "Hydrogen chemisorption on polycyclic aromatic hydrocarbons via tunnelling," *Monthly Notices to the Royal Astronomical Society*, vol. 415, pp. 3129–3134, Aug. 2011.
- [80] J. D. Thrower, B. Jørgensen, E. E. Friis, S. Baouche, V. Mennella, A. C. Luntz, M. Andersen, B. Hammer, and L. Hornekær, "Experimental Evidence for the Formation of Highly Superhydrogenated Polycyclic Aromatic Hydrocarbons through H Atom Addition and Their Catalytic Role in H<sub>2</sub> Formation," *The Astrophysical Journal*, vol. 752, p. 3, June 2012.
- [81] J. D. Thrower, E. E. Friis, A. L. Skov, B. Jørgensen, and L. Hornekær, "Hydrogenation of pah molecules through interaction with hydrogenated carbonaceous grains," *Physical Chemistry Chemical Physics*, vol. 16, no. 8, pp. 3381–3387, 2014.
- [82] A. Skov, J. Thrower, and L. Hornekær, "Polycyclic aromatic hydrocarbons—catalysts for molecular hydrogen formation," *Faraday discussions*, vol. 168, pp. 223–234, 2014.
- [83] A. W. Skov, M. Andersen, J. D. Thrower, B. Jørgensen, B. Hammer, and L. Hornekær, "The influence of coronene super-hydrogenation on the coronene-graphite interaction," *The Journal of chemical physics*, vol. 145, no. 17, p. 174708, 2016.
- [84] J. D. Thrower, E. E. Friis, A. L. Skov, L. Nilsson, M. Andersen, L. Ferrihi, B. Jørgensen, S. Baouche, R. Balog, B. Hammer, *et al.*, "Interaction between coronene and graphite from temperature-programmed desorption and dft-vdw calculations: Importance of entropic effects and insights into graphite interlayer binding," *The Journal of Physical Chemistry C*, vol. 117, no. 26, pp. 13520–13529, 2013.

- [85] U. Zimmermann and N. Karl, "Epitaxial growth of coronene and hexaperi-benzocoronene on MoS<sub>2</sub>(0001) and graphite (0001): a LEED study of molecular size effects," *Surface Science*, vol. 268, pp. 296–306, 1992.
- [86] M. Lackinger, S. Griessl, W. M. Heckl, and M. Hietschold, "Stm and sts of coronene on hopg (0001) in uhv-adsorption of the smallest possible graphite flakes on graphite," *Analytical and bioanalytical chemistry*, vol. 374, no. 4, pp. 685–687, 2002.
- [87] K. Walzer, M. Sternberg, and M. Hietschold, "Formation and characterization of coronene monolayers on HOPG(0001) and MoS<sub>2</sub>(0001): a combined STM/STS and tight-binding study," *Surface Science*, vol. 415, pp. 376–384, Oct. 1998.
- [88] V. Mennella, L. Hornekær, J. Thrower, and M. Accolla, "The Catalytic Role of Coronene for Molecular Hydrogen Formation," *The Astrophysical Journal Letters*, vol. 745, p. L2, Jan. 2012.
- [89] C. W. Bauschlicher Jr, "The reaction of polycyclic aromatic hydrocarbon cations with hydrogen atoms: The astrophysical implications," *The Astrophysical Journal Letters*, vol. 509, no. 2, p. L125, 1998.
- [90] M. Hirama, T. Ishida, and J.-I. Aihara, "Possible molecular hydrogen formation mediated by the radical cations of anthracene and pyrene," *Journal of computational chemistry*, vol. 24, no. 12, pp. 1378–1382, 2003.
- [91] A. Ricca, E. L. O. Bakes, and C. W. Bauschlicher, Jr., "The Energetics for Hydrogen Addition to Naphthalene Cations," *The Astrophysical Journal*, vol. 659, pp. 858–861, Apr. 2007.
- [92] V. Le Page, Y. Keheyan, V. M. Bierbaum, and T. P. Snow, "Chemical constraints on organic cations in the interstellar medium," *Journal of the American Chemical Society*, vol. 119, no. 35, pp. 8373–8374, 1997.
- [93] T. P. Snow, V. Le Page, Y. Keheyan, and V. M. Bierbaum, "The interstellar chemistry of pah cations," *Nature*, vol. 391, no. 6664, pp. 259–260, 1998.

- [94] B. Klærke, Y. Toker, D. B. Rahbek, L. Hornekær, and L. H. Andersen, "Formation and stability of hydrogenated PAHs in the gas phase," *Astronomy and Astrophysics*, vol. 549, p. A84, Jan. 2013.
- [95] S. Cazaux, L. Boschman, N. Rougeau, G. Reitsma, R. Hoekstra, D. Teillet-Billy, S. Morisset, M. Spaans, and T. Schlathölter, "The sequence to hydrogenate coronene cations: A journey guided by magic numbers," *Scientific Reports*, vol. 6, p. 19835, Jan. 2016.
- [96] L. Boschman, G. Reitsma, S. Cazaux, T. Schlathölter, R. Hoekstra, M. Spaans, and O. Gonzalez-Magana, "Hydrogenation of pah cations: A first step toward h<sub>2</sub> formation," *The Astrophysical Journal Letters*, vol. 761, no. 2, p. L33, 2012.
- [97] M. Vala, J. Szczepanski, J. Oomens, and J. D. Steill, "H<sub>2</sub> ejection from polycyclic aromatic hydrocarbons: infrared multiphoton dissociation study of protonated 1, 2-dihydronaphthalene," *Journal of the American Chemical Society*, vol. 131, no. 16, pp. 5784–5791, 2009.
- [98] J. Szczepanski, J. Oomens, J. D. Steill, and M. T. Vala, "H<sub>2</sub> ejection from polycyclic aromatic hydrocarbons: infrared multiphoton dissociation study of protonated acenaphthene and 9, 10-dihydrophenanthrene," *The Astrophysical Journal*, vol. 727, no. 1, p. 12, 2010.
- [99] J. Zhen, P. Castellanos, D. M. Paardekooper, N. Ligterink, H. Linartz, L. Nahon, C. Joblin, and A. G. Tielens, "Laboratory photochemistry of pahs: Ionization versus fragmentation," *The Astrophysical Journal Letters*, vol. 804, no. 1, p. L7, 2015.
- [100] J. Zhen, S. R. Castillo, C. Joblin, G. Mulas, H. Sabbah, A. Giuliani, L. Nahon, S. Martin, J.-P. Champeaux, and P. M. Mayer, "Vuv photo-processing of pah cations: Quantitative study on the ionization versus fragmentation processes," *The Astrophysical Journal*, vol. 822, no. 2, p. 113, 2016.
- [101] M. Gatchell, M. H. Stockett, N. de Ruelle, T. Chen, L. Giacomozzi, R. F. Nascimento, M. Wolf, E. K. Anderson, R. Delaunay, V. Vizcaino, *et al.*, "Failure of hydrogenation in protecting polycyclic aromatic hydrocarbons from fragmentation," *Physical Review A*, vol. 92, no. 5, p. 050702, 2015.

- [102] T. Chen, M. Gatchell, M. H. Stockett, R. Delaunay, A. Domaracka, E. R. Micelotta, A. G. Tielens, P. Rousseau, L. Adoui, B. A. Huber, *et al.*, “Formation of h<sub>2</sub> from internally heated polycyclic aromatic hydrocarbons: Excitation energy dependence,” *The Journal of chemical physics*, vol. 142, no. 14, p. 144305, 2015.
- [103] M. Wolf, L. Giacomozzi, M. Gatchell, N. de Ruelle, H. M. Stockett, T. H. Schmidt, H. Cederquist, and H. Zettergren, “Hydrogenated pyrene: Statistical single-carbon loss below the knockout threshold,” *European Physical Journal D: Atomic, Molecular and Optical Physics*, vol. 70, no. 4, 2016.
- [104] C.-E. Boström, P. Gerde, A. Hanberg, B. Jernström, C. Johansson, T. Kyrklund, A. Rannug, M. Törnqvist, K. Victorin, and R. Westerholm, “Cancer risk assessment, indicators, and guidelines for polycyclic aromatic hydrocarbons in the ambient air.,” *Environmental health perspectives*, vol. 110, no. Suppl 3, p. 451, 2002.
- [105] H. W. Kroto, J. R. Heath, S. C. O’Brien, R. F. Curl, R. E. Smalley, *et al.*, “C<sub>60</sub>: buckminsterfullerene,” *Nature*, vol. 318, no. 6042, pp. 162–163, 1985.
- [106] B. Foing and P. Ehrenfreund, “Detection of two interstellar absorption bands coincident with spectral features of c<sub>60</sub>+,” *Nature*, vol. 369, no. 6478, pp. 296–298, 1994.
- [107] K. Sellgren, M. W. Werner, J. G. Ingalls, J. Smith, T. Carleton, and C. Joblin, “C<sub>60</sub> in reflection nebulae,” *The Astrophysical Journal Letters*, vol. 722, no. 1, p. L54, 2010.
- [108] A. Goeres and E. Sedlmayr, “The envelopes of r coronae borealis stars. i-a physical model of the decline events due to dust formation,” *Astronomy and Astrophysics*, vol. 265, pp. 216–236, 1992.
- [109] I. Cherchneff, Y. Le Teuff, P. Williams, and A. Tielens, “Dust formation in carbon-rich wolf-rayet stars. i. chemistry of small carbon clusters and silicon species,” *Astronomy and Astrophysics*, vol. 357, pp. 572–580, 2000.
- [110] G. Pascoli and A. Polleux, “Condensation and growth of hydrogenated carbon clusters in carbon-rich stars,” *Astronomy and Astrophysics*, vol. 359, pp. 799–810, 2000.

- [111] O. Berné and A. G. Tielens, “Formation of buckminsterfullerene (c60) in interstellar space,” *Proceedings of the National Academy of Sciences*, vol. 109, no. 2, pp. 401–406, 2012.
- [112] O. Berné, J. Montillaud, and C. Joblin, “Top-down formation of fullerenes in the interstellar medium,” *Astronomy & Astrophysics*, vol. 577, p. A133, 2015.
- [113] O. Berne, “From paks to fullerenes: Atronomical models.” Conference presentation, 11 2016.
- [114] E. K. Campbell, M. Holz, D. Gerlich, and J. P. Maier, “Laboratory confirmation of c60+ as the carrier of two diffuse interstellar bands,” *Nature*, vol. 523, no. 7560, pp. 322–323, 2015.
- [115] G. Galazutdinov, V. Shimansky, A. Bondar, G. Valyavin, and J. Krelowski, “C60+—looking for the bucky-ball in interstellar space,” *Monthly Notices of the Royal Astronomical Society*, vol. 465, no. 4, pp. 3956–3964, 2016.
- [116] K. Tschersich and V. Von Bonin, “Formation of an atomic hydrogen beam by a hot capillary,” *Journal of applied physics*, vol. 84, no. 8, pp. 4065–4070, 1998.
- [117] K. Tschersich, “Intensity of a source of atomic hydrogen based on a hot capillary,” *Journal of Applied Physics*, vol. 87, no. 5, pp. 2565–2573, 2000.
- [118] K. Tschersich, J. Fleischhauer, and H. Schuler, “Design and characterization of a thermal hydrogen atom source,” *Journal of applied physics*, vol. 104, no. 3, p. 034908, 2008.
- [119] E. Lægsgaard, F. Besenbacher, K. Mortensen, and I. Stensgaard, “A fully automated, ‘thimble-size’ scanning tunnelling microscope,” *Journal of microscopy*, vol. 152, no. 3, pp. 663–669, 1988.
- [120] P. Hofmann, *Surface Physics: An Introduction*. self-published, 2013.
- [121] J. Venables, *Introduction to surface and thin film processes*. Cambridge University Press, 2000.

- [122] A. W. Skov, *Probing the superhydrogenation of coronene on graphite*. PhD thesis.
- [123] R. Zacharia, *Desorption of gases from graphitic and porous carbon surfaces*. PhD thesis, Freie Universität Berlin, 2004.
- [124] G. Binnig, H. Rohrer, C. Gerber, and E. Weibel, "Tunneling through a controllable vacuum gap," *Applied Physics Letters*, vol. 40, no. 2, pp. 178–180, 1982.
- [125] G. Binnig and H. Rohrer, "Scanning tunneling microscopy," *Surface science*, vol. 126, no. 1-3, pp. 236–244, 1983.
- [126] G. Binnig, H. Rohrer, C. Gerber, and E. Weibel, "7x7 reconstruction on si (111) resolved in real space," *Phys. Rev. Lett*, vol. 50, no. 2, pp. 120–123, 1983.
- [127] "Auger electron spectroscopy (aes)."  
<https://wiki.utep.edu/pages/viewpage.action?pageId=39194437>.  
Data accessed: 21st July, 2017.
- [128] P. Hohenberg and W. Kohn, "Inhomogeneous electron gas," *Physical review*, vol. 136, no. 3B, p. B864, 1964.
- [129] W. Kohn and L. J. Sham, "Self-consistent equations including exchange and correlation effects," *Physical review*, vol. 140, no. 4A, p. A1133, 1965.
- [130] J. P. Perdew and Y. Wang, "Accurate and simple analytic representation of the electron-gas correlation energy," *Physical Review B*, vol. 45, no. 23, p. 13244, 1992.
- [131] A. D. Becke, "A new mixing of hartree-fock and local density-functional theories," *The Journal of chemical physics*, vol. 98, no. 2, pp. 1372–1377, 1993.
- [132] J. Thrower, "H source flux." Private communication, 2017.
- [133] K. Oura, J. Yamane, K. Umezawa, M. Naitoh, F. Shoji, and T. Hanawa, "Hydrogen adsorption on si (100)-2× 1 surfaces studied by elastic recoil detection analysis," *Physical Review B*, vol. 41, no. 2, p. 1200, 1990.

- [134] F. Shoji, K. Kashihara, K. Sumitomo, and K. Oura, "Low-energy recoil-ion spectroscopy studies of hydrogen adsorption on si (100)- $2 \times 1$  surfaces," *Surface Science*, vol. 242, no. 1-3, pp. 422–427, 1991.
- [135] F. Shoji, K. Kusumura, and K. Oura, "A si (100)- $2 \times 1$ : H monohydride surface studied by low-energy recoil-ion spectroscopy," *Surface science*, vol. 280, no. 1-2, pp. L247–L252, 1993.
- [136] Y. Chabal and K. Raghavachari, "New ordered structure for the h-saturated si (100) surface: the ( $3 \times 1$ ) phase," *Physical review letters*, vol. 54, no. 10, p. 1055, 1985.
- [137] S. White and D. Woodruff, "The surface structure of si (100) surfaces using averaged leed: I. the ( $1 \times 1$ ) h structure," *Surface Science*, vol. 63, pp. 254–262, 1977.
- [138] M. Suemitsu, H. Nakazawa, and N. Miyamoto, "Temperature-programmed-desorption study of the process of atomic deuterium adsorption onto si (100)  $2 \times 1$ ," *Applied surface science*, vol. 82, pp. 449–453, 1994.
- [139] F. Tautz and J. Schaefer, "Ultimate resolution electron energy loss spectroscopy at h/si (100) surfaces," *Journal of applied physics*, vol. 84, no. 12, pp. 6636–6643, 1998.
- [140] J. J. Boland, "Structure of the h-saturated si (100) surface," *Physical review letters*, vol. 65, no. 26, p. 3325, 1990.
- [141] J. J. Boland, "Role of bond-strain in the chemistry of hydrogen on the si (100) surface," *Surface science*, vol. 261, no. 1-3, pp. 17–28, 1992.
- [142] Y. Wang, M. Shi, and J. Rabalais, "Structure of the si {100} surface in the clean ( $2 \times 1$ ), ( $2 \times 1$ )-h monohydride, ( $1 \times 1$ )-h dihydride, and c ( $4 \times 4$ )-h phases," *Physical Review B*, vol. 48, no. 3, p. 1678, 1993.
- [143] X. Qin and P. Norton, "Scanning tunneling microscopy of the phase transition between h/si (100)-( $2 \times 1$ ) and h/si (100)-( $3 \times 1$ )," *Physical Review B*, vol. 53, no. 16, p. 11100, 1996.
- [144] K. Oura, V. Lifshits, A. Saranin, A. Zotov, and M. Katayama, "Hydrogen interaction with clean and modified silicon surfaces," *Surface Science Reports*, vol. 35, no. 1, pp. 1–69, 1999.

- [145] A. Dinger, C. Lutterloh, and J. Küppers, “Kinetics of d abstraction with h atoms from the monodeuteride phase on si (100) surfaces,” *Chemical physics letters*, vol. 311, no. 3, pp. 202–208, 1999.
- [146] P. Redhead, “Thermal desorption of gases,” *Vacuum*, vol. 12, no. 4, pp. 203–211, 1962.
- [147] J. Gardener, G. Briggs, and M. Castell, “Scanning tunneling microscopy studies of c 60 monolayers on au (111),” *Physical Review B*, vol. 80, no. 23, p. 235434, 2009.
- [148] J. Bernard-Salas, E. Peeters, G. Sloan, S. Gutenkunst, M. Matsuura, A. Tielens, A. Zijlstra, and J. Houck, “Unusual dust emission from planetary nebulae in the magellanic clouds,” *The Astrophysical Journal*, vol. 699, no. 2, p. 1541, 2009.
- [149] L. Cerrigone, J. L. Hora, G. Umana, and C. Trigilio, “Spitzer detection of polycyclic aromatic hydrocarbons and silicate features in post-agn stars and young planetary nebulae,” *The Astrophysical Journal*, vol. 703, no. 1, p. 585, 2009.
- [150] L. Cerrigone, J. L. Hora, G. Umana, C. Trigilio, A. Hart, and G. Fazio, “Identification of three new protoplanetary nebulae exhibiting the unidentified feature at 21  $\mu\text{m}$ ,” *The Astrophysical Journal*, vol. 738, no. 2, p. 121, 2011.
- [151] T. Herter, J. Adams, J. De Buizer, G. Gull, J. Schoenwald, C. Henderson, L. Keller, T. Nikola, G. Stacey, and W. Vacca, “First science observations with sofia/forcast: the forcast mid-infrared camera,” *The Astrophysical Journal Letters*, vol. 749, no. 2, p. L18, 2012.
- [152] E. Young, E. Becklin, P. Marcum, T. Roellig, J. De Buizer, T. Herter, R. Güsten, E. Dunham, P. Temi, B.-G. Andersson, *et al.*, “Early science with sofia, the stratospheric observatory for infrared astronomy,” *The Astrophysical Journal Letters*, vol. 749, no. 2, p. L17, 2012.
- [153] P. Temi, P. M. Marcum, E. Young, J. D. Adams, S. Adams, B.-G. Andersson, E. E. Becklin, A. Boogert, R. Brewster, E. Burgh, *et al.*, “The sofia observatory at the start of routine science operations: Mission capabilities and performance,” *The Astrophysical Journal Supplement Series*, vol. 212, no. 2, p. 24, 2014.

- [154] T. De Graauw, L. Haser, D. Beintema, P. Roelfsema, H. Van Agthoven, L. Barl, O. Bauer, H. Bekenkamp, A.-J. Boonstra, D. Boxhoorn, *et al.*, “Observing with the iso short-wavelength spectrometer,” *Astronomy and Astrophysics*, vol. 315, pp. L49–L54, 1996.
- [155] M. Kessler, J. Steinz, M. Anderegg, J. Clavel, G. Drechsel, P. Estaria, J. Faelker, J. Riedinger, A. Robson, B. Taylor, *et al.*, “The infrared space observatory (iso) mission.,” *Astronomy and Astrophysics*, vol. 315, pp. L27–L31, 1996.
- [156] J. R. Houck, T. L. Roellig, J. Van Cleve, W. J. Forrest, T. L. Herter, C. R. Lawrence, K. Matthews, H. J. Reitsema, B. Soifer, D. M. Watson, *et al.*, “The infrared spectrograph on the spitzer space telescope,” in *SPIE Astronomical Telescopes+ Instrumentation*, pp. 62–76, International Society for Optics and Photonics, 2004.
- [157] M. Werner, T. Roellig, F. Low, G. H. Rieke, M. Rieke, W. Hoffmann, E. Young, J. Houck, B. Brandl, G. Fazio, *et al.*, “The spitzer space telescope mission,” *The Astrophysical Journal Supplement Series*, vol. 154, no. 1, p. 1, 2004.
- [158] M. Wenger, F. Ochsenbein, D. Egret, P. Dubois, F. Bonnarel, S. Borde, F. Genova, G. Jasniewicz, S. Laloë, S. Lesteven, *et al.*, “The simbad astronomical database—the cds reference database for astronomical objects,” *Astronomy and Astrophysics Supplement Series*, vol. 143, no. 1, pp. 9–22, 2000.
- [159] P. M. Woods, J. Oliveira, F. Kemper, J. T. van Loon, B. Sargent, M. Matsuura, R. Szczerba, K. Volk, A. Zijlstra, G. Sloan, *et al.*, “The sage-spec spitzer legacy programme: the life-cycle of dust and gas in the large magellanic cloud—point source classification i,” *Monthly Notices of the Royal Astronomical Society*, vol. 411, no. 3, pp. 1597–1627, 2011.
- [160] S. Hony, C. Van Kerckhoven, E. Peeters, A. Tielens, D. Hudgins, and L. Allamandola, “The ch out – of – plane bending modes of pah molecules in astrophysical environments,” *Astronomy & Astrophysics*, vol. 370, no. 3, pp. 1030–1043, 2001.

- [161] C. Boersma, C. Bauschlicher, L. Allamandola, A. Ricca, E. Peeters, and A. Tielens, “The 15–20  $\mu\text{m}$  pah emission features: probes of individual pachs?,” *Astronomy & Astrophysics*, vol. 511, p. A32, 2010.
- [162] D. Stock, E. Peeters, A. Tielens, J. Otaguro, and A. Bik, “Extinction and polycyclic aromatic hydrocarbon intensity variations across the h ii region iras 12063–6259,” *The Astrophysical Journal*, vol. 771, no. 1, p. 72, 2013.
- [163] D. Stock, E. Peeters, W.-Y. Choi, and M. Shannon, “The mid-infrared appearance of the galactic mini-starburst w49a,” *The Astrophysical Journal*, vol. 791, no. 2, p. 99, 2014.
- [164] M. Shannon, D. Stock, and E. Peeters, “Probing the ionization states of polycyclic aromatic hydrocarbons via the 15? 20? m emission bands,” *The Astrophysical Journal*, vol. 811, no. 2, p. 153, 2015.
- [165] E. Peeters, C. W. Bauschlicher, Jr., L. J. Allamandola, A. G. G. M. Tielens, A. Ricca, and M. G. Wolfire, “The PAH Emission Characteristics of the Reflection Nebula NGC 2023,” *The Astrophysical Journal*, vol. 836, p. 198, Feb. 2017.
- [166] D. J. Stock, W. D.-Y. Choi, L. G. V. Moya, J. N. Otaguro, S. Sorkhou, L. J. Allamandola, A. G. G. M. Tielens, and E. Peeters, “Polycyclic Aromatic Hydrocarbon Emission in Spitzer/IRS Maps. I. Catalog and Simple Diagnostics,” *The Astrophysical Journal*, vol. 819, p. 65, Mar. 2016.
- [167] F. Galliano, S. C. Madden, A. G. Tielens, E. Peeters, and A. P. Jones, “Variations of the mid-ir aromatic features inside and among galaxies,” *The Astrophysical Journal*, vol. 679, no. 1, p. 310, 2008.
- [168] C. Van Kerckhoven, *Polycyclic Aromatic Hydrocarbons and Diamonds around Young Stellar Objects*. PhD thesis, 2002.
- [169] D. M. Hudgins and L. Allamandola, “Interstellar pah emission in the 11-14 micron region: New insights from laboratory data and a tracer of ionized pachs,” *The Astrophysical Journal Letters*, vol. 516, no. 1, p. L41, 1999.